NORTHWESTERN UNIVERSITY

The Dawn of Multi-Messenger Astronomy: Neutron Star Mergers and Gravitational Waves

A DISSERTATION

SUBMITTED TO THE GRADUATE SCHOOL

IN PARTIAL FULFILLMENT OF THE REQUIREMENTS

for the degree

DOCTOR OF PHILOSOPHY

Field of Astronomy

By

Eve A. Chase

EVANSTON, ILLINOIS

September 2021

ABSTRACT

The Dawn of Multi-Messenger Astronomy: Neutron Star Mergers and Gravitational Waves

Eve A. Chase

Neutron star mergers instigate a wealth of observable astrophysical signals, offering key insights into interdisciplinary questions in stellar astronomy, nuclear physics, cosmology, and atomic physics. The coalescence of neutron stars and/or black holes produces gravitational wave emission, only recently accessible to ground-based laser-interferometric detectors. Additionally, these mergers can incite emission across the electromagnetic spectrum, including short-duration gamma-ray bursts and kilonova emission, where kilonovae are ultraviolet, optical, and infrared transients powered by the radioactive decay of heavy elements following a neutron star merger.

In this thesis, I investigate three topics related to the joint detection of gravitational wave and electromagnetic signals from neutron star mergers. Throughout this work, I describe the production of sky localization maps from gravitational-wave detector data, with a focus on sky localization maps for binary neutron star (BNS) and neutron star – black hole (NSBH) binary systems. I present the first systematic study of sky localization

for NSBH systems, finding a median sky localization of 60 deg^2 with three advanced ground-based interferometers which is reduced to 19 deg^2 and 11 deg^2 with four and five interferometers, respectively. Additionally, I present a case study in which the estimation of sky localization maps is hindered by the presence of an instrumental noise transient. In this case study, I describe methods of transient removal and verify that this excision process does not bias astrophysical parameter estimates. Lastly, I quantify the ability of 13 wide field-of-view instruments to detect kilonovae following a gravitational wave detection, leveraging a large grid of over 900 radiative transfer simulations. In the process, I provide a framework to infer kilonova ejecta properties following non-detections and explore variation in detectability with these ejecta parameters.

Acknowledgements

I am immensely grateful for the extensive network of friends, family, and colleagues that have supported me throughout graduate school. First and foremost, I acknowledge the support of my advisor Vicky Kalogera throughout the production of this thesis. Vicky, these past five years haven't been easy for either of us. We've both had more than our fair share of highs and lows, but I hope we can both take pride in the completion of this thesis. I know I will look back on my PhD experience fondly as an immense period of personal growth. Additionally, I also acknowledge the support of my committee members Wen-fai Fong and Christopher Fryer, in addition to mentorship from Christopher Berry and Christopher Pankow.

My graduate research has benefited from numerous avenues of financial support, including the Illinois Space Grant Consortium graduate fellowship and the IDEAS Fellowship, a research traineeship program funded by the National Science Foundation under grant DGE-1450006. I also had the immense pleasure of participating in the first cohort of the LSSTC Data Science Fellowship program. The skills I gained through this program were instrumental in the completion of this dissertation.

I can't possibly list every person who has supported me throughout my graduate career, although I'll aim to list a few here. I am grateful to the many wonderful classmates and colleagues I have met through my time at Northwestern, my peers in the LSSTC Data Science Fellowship Program, and my fantastic collaborators in the LVC– thank

you all! In particular, I want to thank Haley Bauser and Matthew Heffernan for their constant support throughout my entire PhD journey. Thank you for standing by my side for all these years. Thank you to my fantastic officemates in CIERA: Chase Kimball, Cody Dirks, and Michael Zevin. Thank you to the Northwestern University Graduate Workers dissertation writing group for pushing me to complete this work– you guys rock! Lastly, I want to acknowledge the phenomenal support of staff members in CIERA and the Department of Physics & Astronomy, including Bud Robinson, Pam Villalovoz, Yas Shemirani, Kari Frank, John Everett, Lisa Raymond, Alexandria Romasanta, Michelle Paulsen, Peter Anglada, and Gretchen Oehlschlager.

I am extremely grateful for Carlos and Tamara Moreno for housing me during the completion of my dissertation. I know everyone thinks I was in Cinicinnati to help you around the house, but the three of us know you were really helping me. And lastly, I thank Aaron Buzek for contributions as figure color consultant.

List of abbreviations

BBH – binary black hole
BH – black hole
BNS – binary neutron star
CE – common envelope
DNS – double neutron star
EM – electromagnetic
EOS – equation of state
FFT – fast Fourier transform
FoV – field of view
GRB – gamma-ray burst
GW – gravitational wave
HMXB – higher-mass X-ray binary
ISM – interstellar medium
LIGO – Laser Interferometer Gravitational-Wave Observatory
LVC – LIGO - Virgo Collaboration
MCMC – Markov chain Monte Carlo
MM – multi-messenger
MMA – multi-messenger astronomy
NS – neutron star
NSBH – neutron star–black hole
NSM – neutron star merger
PN – post-Newtonian
PSD – power spectral density
RLO – Roche-lobe overflow
sGRB – short gamma-ray burst
SN – supernova
SNR – signal-to-noise ratio
TFA – time-frequency area
UVOIR – ultraviolet/optical/infrared
XRB – X-ray binary
ZAMS – zero-age main sequence

Dedication

To my parents, Tana and Greg.

Table of Contents

List of Tables

List of Figures

CHAPTER 1

Introduction

The era of multi-messenger astronomy (MMA) with gravitational waves is upon us. Multi-messenger (MM) observations involve joint detections with two or more astronomical "messengers": either electromagnetic (EM) observations, gravitational waves (GWs), neutrinos, or cosmic rays. The first extrasolar MM observation was made in 1987, with the combined observation of neutrinos and EM emission from a supernova (SN 1987A) in the Large Magellanic Cloud (Hirata et al., 1987; Bionta et al., 1987; Alekseev et al., 1987; Hirata et al., 1988). Thirty years later, in 2017, a world-wide network of astronomers made the first MM detection with GWs, through the joint detection of GWs and EM emission from a binary neutron star (BNS) merger (GW170817/GRB 170817A/AT 2017gfo; Abbott et al., 2017a,b,c), ushering in a new era of astronomy. The advent of MMA with neutron star mergers (NSMs) holds immense promise for key questions in stellar astronomy, cosmology, nuclear physics, and other interdisciplinary subjects. While only one observation has been made to-date, the 2020s offer ample opportunities to grow our sample of MM observations of NSMs with GWs.

Neutron stars are hot, dense, old stellar objects at the final stages of their lives. Correctly theorized by Baade & Zwicky (1934), neutron stars are remnants of supernova explosions. These stars are supported by neutron degeneracy pressure and exhibit some of the largest densities in the Universe ($\sim 10^{15}$ g cm^{-3}; i.e. Lattimer, 2015). Neutron stars were first observed in the 1960s through X-ray emission from the binary star system

Scorpius X-1 (Giacconi et al., 1962), which was later interpreted as accretion onto a neutron star (Shklovsky, 1967). In the same decade, Jocelyn Bell Burnell discovered radio pulsars (Hewish et al., 1968; Gold, 1968, 1969), neutron stars with beamed emission.

An typical neutron star's mass is equivalent to the Chandrasekhar limit (1.4 $M_{\odot}$), although various formation scenarios and progenitor properties lead to variations in mass. The maximum neutron star mass is an open question in astrophysics, founded upon the Tolman – Oppenheimer – Volkoff (TOV) equation (Oppenheimer & Volkoff, 1939). Recent estimates predict that the TOV mass is $M_{\rm TOV} \lesssim 2.16^{+0.17}_{-0.15}\ M_{\odot}$ (Rezzolla et al., 2018), where the TOV mass corresponds to the maximum mass of a non-rotating neutron star. Higher masses are possible for rotating neutron stars, with inferred maximum neutron star masses of $M_{\rm max} = \left(1.20^{+0.02}_{-0.02}\right) M_{\rm TOV}$ (Breu & Rezzolla, 2016). Currently, there are three observational candidates for the most massive neutron star: PSR J1614–2230 with a mass of $1.908 \pm 0.016\ M_{\odot}$ (Demorest et al., 2010; Fonseca et al., 2016; Arzoumanian et al., 2018), PSR J0348+0432 with a mass of $2.01 \pm 0.04\ M_{\odot}$ (Antoniadis et al., 2013), and PSR J0740+6620 with a mass of $2.08 \pm 0.07\ M_{\odot}$, where all uncertainties are given at the 1σ confidence level.

Neutron stars are frequently located in binary star systems, with a wide range of possible companions. This thesis focuses on binary systems composed of either two neutron stars, known as both binary neutron star and double neutron star systems (we employ the BNS nomenclature in this thesis), or a neutron star – black hole (NSBH) binary. In this thesis, we classify both systems as NSMs when their components eventually coalesce. In the 1970s, Hulse and Taylor made the first detection of a BNS system (Hulse & Taylor, 1975). Although the neutron stars in this binary are not expected to merge for another

300 million years (Weisberg et al., 1981), measurements of the binary's shrinking orbit provided strong evidence for the production of GWs (Taylor & Weisberg, 1982).

The formation of neutron star binaries which merge within a Hubble time relies on a delicate balance of multiple evolutionary scenarios. The typical formation sequence of neutron star binaries is summarized in Figure 1.1 and reviewed in Kalogera et al. (2007) and Tauris et al. (2017). In short, the formation of a neutron star binary involves two supernova explosions and multiple episodes of mass transfer. Each supernova explosion produces a compact object: either a neutron star or a black hole. Mass transfer episodes may tighten a binary's orbit, decreasing the time needed for the compact objects to coalesce. In some cases, mass transfer may lead to the collapse of a neutron star to a black hole, potentially producing a NSBH binary. Similar formation scenarios may also produce binary black hole (BBH) systems.

In the final stages of the binary's evolution, the orbital semi-major axis shrinks as GWs are emitted. Einstein's general theory of relativity predicts that all accelerating massive objects with non-spherical geometries emit GWs, oscillations in the space-time metric (Einstein, 1916, 1918). GWs were detected for the first time in 2015 (Abbott et al., 2016a), through the observation of a BBH merger with ground-based laser-interferometric detectors. Existing GW detectors include the two advanced LIGO detectors (Aasi et al., 2015), the advanced Virgo detector (Acernese et al., 2015), and KAGRA (Akutsu et al., 2019), with proposed plans for the construction of additional interferometers in the coming decades. In this thesis, I focus on the observation of compact binary mergers with ground-based GW detectors; however, I note that other astrophysical sources are observable with these instruments, including core-collapse SNe and continuous GW signals. Other

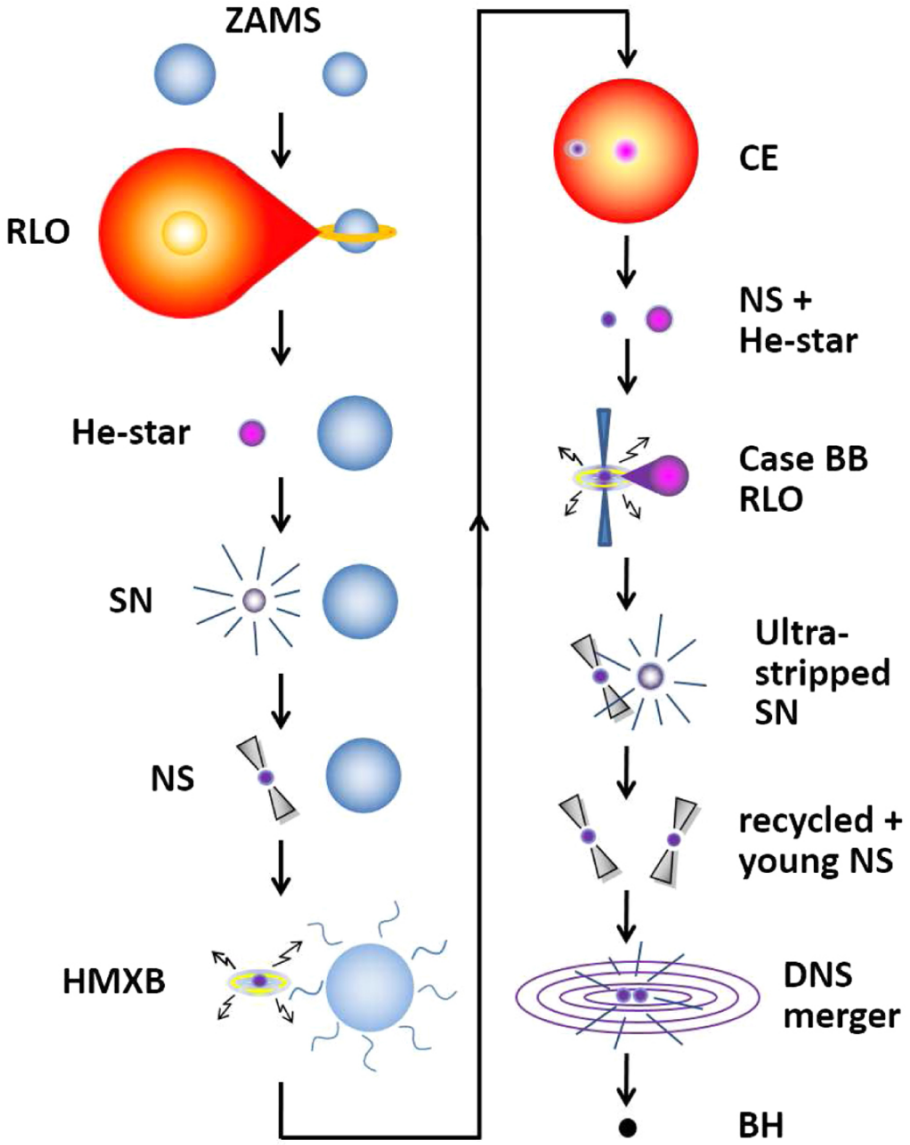

Figure 1.1. Figure 1 of Tauris et al. (2017) summarizes the typical formation mechanism of a BNS system. In the example shown, the BNS eventually forms a black hole; although we note that formation of a neutron star is also possible (see Metzger 2019 for a review). All abbreviations in the figure are defined on page 7. NSBHs are theorized to be assembled through similar formation mechanisms (i.e. Broekgaarden et al., 2021).

methods of GW detection, including with the space-based LISA detector (Amaro-Seoane et al., 2017) and pulsar timing arrays (Manchester & IPTA, 2013), are expected to reveal additional GW sources.

At the time of this thesis's compilation, there are 50 known GW events, all emanating from compact binary mergers (Abbott et al., 2021). Through the use of Bayesian parameter estimation (i.e. Veitch et al., 2015), properties of each binary are inferred including masses, spins, inclination, and sky localization (see Chapters 2 and 3). Of the 50 events, at least three are consistent with a merger containing at least one NS (Abbott et al., 2021). GW170817 remains the only confirmed MM observation of a NSM.

NSMs can produce emission spanning the EM spectrum, as summarized in Figure 1.2 and reviewed in Metzger & Berger (2012), Fernández & Metzger (2016), and Metzger (2019). EM sources associated with a NSM include a sGRB and kilonova, along with their respective afterglows. For decades, NSMs were the theorized progenitors of GRBs (Blinnikov et al., 1984; Paczynski, 1986; Eichler et al., 1989; Narayan et al., 1992). Later theories eventually linked NSMs to the short-duration subclass of GRBs (sGRBs; Popham et al., 1999; Fryer et al., 1999), defined as GRBs persisting for less than two seconds (Norris et al., 1984; Kouveliotou et al., 1993). While significant observational evidence supported the association between sGRBs and NSMs (see Berger 2014 for a review), this connection was finally solidified with the MM detection of GW170817 (Abbott et al., 2017a,c).

A subset of NSMs also result in kilonova emission, spanning UVOIR wavelengths. Since the 1970s, NSMs have been proposed as cosmic sources of heavy elements produced through rapid-neutron capture (r-process) nucleosynthesis (Lattimer & Schramm, 1974; Lattimer et al., 1977; Symbalisty & Schramm, 1982; Eichler et al., 1989; Freiburghaus

et al., 1999). The r-process was first introduced by Burbidge et al. (1957) and Cameron (1957), and refers to the rapid capture of free neutrons in dense environments before the nuclei have time to radioactively decay through β-decay. The r-process is the proposed origin of roughly half of all atomic nuclei heavier than iron, including many lanthanide and actinide isotopes. NSMs were repeatedly proposed as astrophysical sources of the r-process until their confirmation with the observation of GW170817 (Abbott et al., 2017b). Although a substantial source of r-process enrichment, NSMs may not be able to account for the full set of r-process abundance throughout the galaxy (Côté et al., 2019; Holmbeck et al., 2021). Additional MM observations of NSMs are necessary to further constrain the role of NSMs in heavy element production (see Côté et al. 2018 for review).

Kilonova emission is hallmarked by an early "blue" component which eventually gives way to a longer-lived "red" component, persisting for upwards of a week. The red component corresponds to higher-wavelength emission in optical and near-infrared wavelengths, indicative of lanthanide-rich or low-Y_e ejecta, where Y_e is the electron fraction of ejecta

$$Y_e = \frac{n_p}{n_n + n_p}, \tag{1.1}$$

where n_p and n_n are the density of protons and neutrons, respectively. For neutral ions, the proton density is equivalent to the electron density, n_e, such that high-Y_e values correspond to electron-rich or, equivalently, neutron-poor ejecta. Low-Y_e ejecta corresponds to neutron-rich ejecta, an expected result of r-process nucleosynthesis.

Red emission typically originates from dynamical ejecta, tidally stripped from the inspiraling neutron star(s). On the contrary, blue emission refers to lower-wavelength emission in ultraviolet and optical wavelengths, consistent with lanthanide-poor or high-Y_e

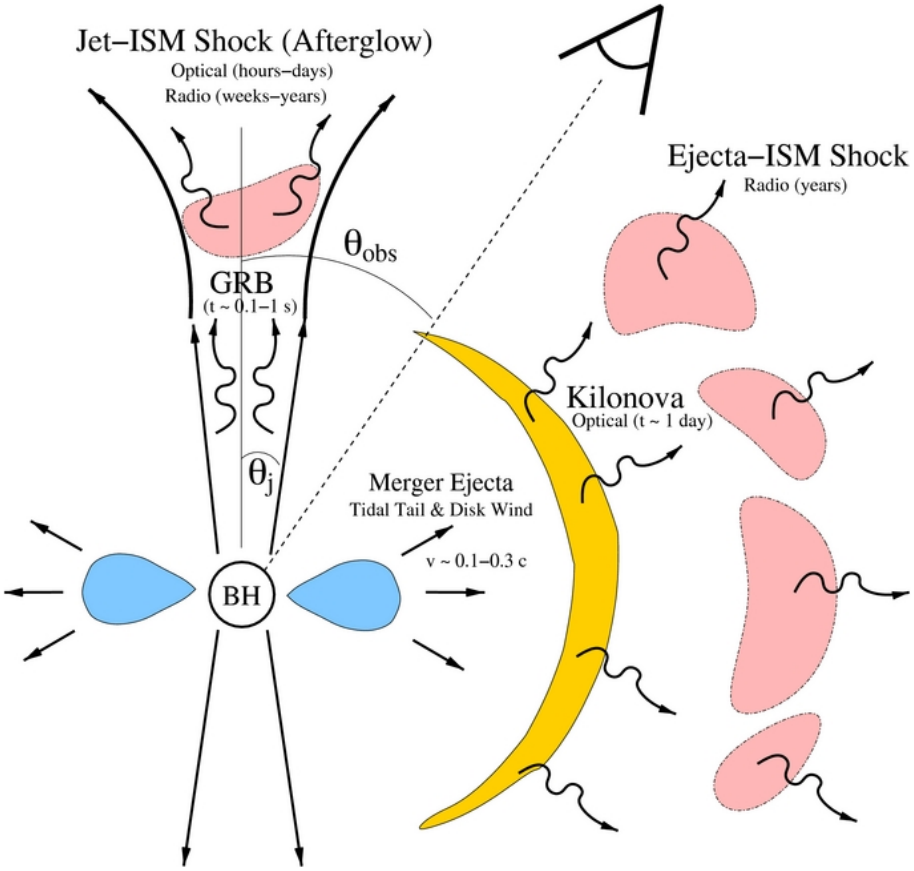

Figure 1.2. Figure 1 of Metzger & Berger (2012) summarizes the multiple mechanisms of EM emission from a NSM. sGRB emission is concentrated around the poles, while kilonova emission is generally isotropically distributed around the remnant compact object. Both the sGRB and kilonova later incite afterglow emission.

ejecta. There are multiple sources of lanthanide-poor ejecta in NSMs (see Metzger 2019), including wind-driven ejecta from an accretion disk surrounding the remnant compact object. The identity of the remnant compact object may alter the Y_e of ejecta concentrated in an accretion disk through neutrino irradiation (i.e. Kasen et al., 2015; Fernández & Metzger, 2016; Lippuner et al., 2017). All BNSs yield kilonovae while only NSBH systems with near-equal mass ratios (i.e. low-mass BHs) produce kilonova emission (see Metzger

2019 and references therein), with observable kilonova emission more likely for high-spin BHs (i.e. Rantsiou et al., 2008).

Some NSMs also produce afterglow emission, corresponding to synchrotron-drive radio and X-ray emission potentially observable for years after merger. Afterglow emission accompanies a subset of sGRB observations (i.e. Sari et al., 1998; Berger, 2014; Fong et al., 2015), with emission concentrated along polar viewing angles. Additionally, afterglow emission is predicted to accompany a kilonova, as the NSM ejecta expands into the surrounding interstellar medium, yielding emission known as either a kilonova afterglow or "radio flare" (i.e. Nakar & Piran, 2011; Hajela et al., 2019, 2021; Troja et al., 2021). At the time of this thesis's compilation, no kilonova afterglow has been confidently detected.

Several follow-up observations of sGRBs reveal plausible kilonova candidates (i.e. Perley et al., 2009; Tanvir et al., 2013; Berger et al., 2013; Yang et al., 2015; Jin et al., 2016; Troja et al., 2018; Gompertz et al., 2018; Ascenzi et al., 2019; Lamb et al., 2019; Troja et al., 2019a; Jin et al., 2020; Rossi et al., 2020; Fong et al., 2021; Rastinejad et al., 2021; O'Connor et al., 2021). Although, the connection between NSMs, sGRBs, and kilonovae was not solidified until the joint observation of GW170817 and AT 2017gfo.

In this thesis, I provide an overview of numerous challenges in MMA with GWs, with a specific focus on the identification of UVOIR kilonova emission. As kilonovae fade on rapid timescales, quick and efficient observations are imperative for the detection of a kilonova in association with a GW candidate event. The LIGO/Virgo/KAGRA collaboration publicly announces candidate events, sharing a low-latency estimate on distance and sky location, ideally within minutes of GW detection.[1] In some cases, such as the observation

[1]LIGO/Virgo Public Alerts User Guide: `https://emfollow.docs.ligo.org/userguide/index.html`.

of GW170817 (Abbott et al., 2017a,c), a sGRB may be identified nearly-simultaneously with a GW candidate event, through large-scale time-domain surveys such as the *Fermi Gamma-Ray Burst Monitor*. Additional timing information from GRB observations may further refine the sky localization area for a NSM (Abbott et al., 2017c; Goldstein et al., 2020). In order to promptly detect a kilonova associated with an event, astronomers rapidly search the low-latency sky localization region for plausible transient events. If the sky localization is tightly constrained, small field-of-view (FoV) instruments may make galaxy-targeted observations throughout the localization region. However, wide-field observations are necessary if sky localization estimates span wide areas of the sky.

I present an overview of GW sky localization following NSMs in Chapter 2. In this chapter, I explore how sky localization estimates will improve as additional ground-based GW interferometers are constructed. In Chapter 3, I present a case study of instrumental noise transients in GW interferometers hindering the production of a sky localization map in low latency. Through this discussion, I describe various excision methods to remove instrumental noise signals from interferometer data and verify that these excision methods do not bias parameter estimates. Chapter 4 describes a selection of current and upcoming wide-field UVOIR instruments and quantifies their ability to detect kilonova. This section also describes radiative transfer simulations of kilonova emission, provided in Wollaeger et al. (2021). Lastly, in Chapter 5, I offer concluding remarks.

CHAPTER 2

Improvements in Gravitational-Wave Sky Localization with Expanded Networks of Interferometers

In this chapter, I present a systematic study of sky localization of BNS and NSBH events using gravitational-wave parameter estimation techniques. I specifically focus on the inclusion of the KAGRA and LIGO-India interferometers. This work was initially published in Pankow et al. (2018a) and has been updated to reflect recent changes in detection rate estimates and instrument timelines. At the time of publication, this was the first study of its kind for NSBH events.

2.1. Introduction

The joint detection of gravitational waves from a BNS merger (Abbott et al., 2017b) and subsequent electromagnetic observations of an associated sGRB (Abbott et al., 2017c) and kilonova (Abbott et al., 2017d) have added gravitational-wave observations to multi-messenger astronomy (Abbott et al., 2017a). The detection of events with electromagnetic, neutrino, and gravitational-wave observations can provide cross-cutting measurements of phenomena that would be otherwise inaccessible individually, for instance, an independent measurement of the Hubble constant via electromagnetic and gravitational-wave distance estimates (Abbott et al., 2017e). Additional multi-messenger events are awaited, as the advanced LIGO and Virgo detectors reach design sensitivity (Aasi et al.,

2015; Acernese et al., 2015). In the era of multi-messenger astronomy, improved sky localization of gravitational-wave events will promote the routine and rapid identification of electromagnetic counterparts. The study presented here focuses on compact binaries with at least one neutron star component, with a specific emphasis on NSBH binaries. Both categories provide a wide variety of electromagnetic signatures (Metzger & Berger, 2012), such as sGRBs, afterglows, and kilonovae. However, certain configurations of NSBH binaries are unfavorable to such emission as the neutron star is engulfed by the black hole before disruption (Pannarale & Ohme, 2014).

Localization on the sky with networks of gravitational-wave interferometers relies on relative signal arrival times and the realized signal amplitude in each detector. For example, a network of two instruments with perfect timing reconstruction would produce rings on the sky corresponding to locations with similar arrival times. Using consistency between the amplitude responses in widely-separated instruments can refine this result to a few disconnected arcs along the ring (Singer et al., 2014). Furthermore, the inclusion of physical parameters of the source (intrinsic parameters such as spin) can help break degeneracies and further constrain sky localization (van der Sluys et al., 2008; Raymond et al., 2009): component spins misaligned with the orbital angular momentum can introduce "knotting" in the arc. However, with only two detectors, electromagnetic facilities would likely need to search hundreds to thousands of square degrees on the sky to adequately survey the full posterior probability distribution of sky localization.

The Virgo detector in Cascina, Italy joined the two US-based LIGO detectors for the last month of LIGO's second Observing Run (O2; Abbott et al., 2019a), altering the

network's ability to localize sources on the sky. The addition of a third detector can substantially improve localization by introducing another set of baselines, and consequently, several intersecting rings on the sky of constant arrival time. The intersections of the rings identify source locations consistent with measured arrival time differences. Additionally, despite Virgo's lower sensitivity during O2 compared to the two LIGO detectors, the inclusion of data from Virgo provides another set of baselines as well as another point of comparison for the expected signal amplitude on arrival at separated instruments. This is exemplified by the LIGO-Virgo detections GW170814 and GW170817. GW170814 (Abbott et al., 2017f), the first three-detector observation of gravitational waves from a compact binary merger, was localized to 1160 $\deg^2$ at the 90% credible level with only the two LIGO detectors. The inclusion of Virgo reduced this area to only 100 $\deg^2$. For the BNS merger GW170817, the addition of data from Virgo reduced the LIGO-only 100 $\deg^2$ sky localization to roughly 30 $\deg^2$ (Abbott et al., 2017b), enabling the swift identification of the electromagnetic transients and host galaxy (Abbott et al., 2017a). Over the next decade, it is anticipated that sky localization of compact binary systems detected through gravitational waves will be confined to areas of a few tens to hundreds of square degrees (Abbott et al., 2020a), as all detectors reach design sensitivity.

Two additional ground-based interferometers are scheduled to come online in the early 2020s. KAGRA, a Japanese-built, cryogenically-cooled, 3-km interferometer in the Kamioka mine (Akutsu et al., 2019) is will join LIGO and Virgo in the fourth Observing Run (O4; Abbott et al., 2020a). In addition, construction is expected to begin on the LIGO-India detector in the coming years with possible operations beginning in the late 2020s (IndIGO Collaboration, 2011). If all five instruments are active and equally

sensitive, it is expected that sky localization regions for BNS systems will reduce to $\sim 1 - 10$ deg^2 (Wen & Chen, 2010).

In this study, we examine sky localization mainly for a set of NSBH mergers detectable by the LIGO-Virgo network (HLV). We then study the same events in the LIGO-KAGRA-Virgo (HKLV) and LIGO-India-KAGRA-Virgo (HIKLV) detector configurations, following the expected progression of additions to the detector network. In general, the progression from three-, to four-, to five-instrument networks reduces the median integral sky area at the 90% credible interval by about a factor of two between each detector configuration for a canonical population of NSBH sources. While multiple studies have examined sky localization with BNS systems (Nissanke et al., 2011; Veitch et al., 2012; Singer et al., 2014; Rodriguez et al., 2014; Berry et al., 2015; Farr et al., 2016), this is the first study to examine the localization of a population of NSBH events with plausible component masses and spins in the advanced gravitational-wave detector era. We also perform a similar study for a smaller selection of BNS sources, as a comparison metric with past studies.

2.2. Gravitational-Wave Sky Localization

The amplitude, time of arrival, and phase of the gravitational-wave strain at a given instrument is dependent on the source location. The measured strain has an intrinsic source-dependent amplitude, and two factors (the so-called "antenna patterns") determining the geometric sensitivity to either polarization of the gravitational wave. A single interferometer, and hence only a single measurement of the combination of two amplitudes, is unable to independently measure responses to both gravitational-wave polarizations,

nor a time-of-arrival difference, and is therefore unsuitable for source sky localization However, localization is possible with two or more interferometers, as each additional detector provides an independent measure of the difference in time of arrival along the sites' baseline. Each difference corresponds to a ring of locations in the sky, with the center of the ring formed by the baseline projected into the celestial sphere. The intersections of those rings for each detector pair indicate most probable source locations on the sky. As the number of detectors increases, specific intersections are favored, further reducing sky localization regions. This is equivalent to the technique of triangulation (Fairhurst, 2011a) Rings of constant arrival time have widths proportional to source timing uncertainty. In addition to the time of arrival precision (and hence timing uncertainty), the precision with which phase of arrival is determined is also crucial to the localization size (Singer & Price, 2016).

The orientation of the gravitational-wave detector relative to the incident source direction further affects localization. Different detectors are not equally sensitive to the same source location, as gravitational-wave interferometers are not omni-directional and do not have aligned zenith axes. As additional detectors are constructed, the constraints on which relative amplitudes (corresponding to antenna-pattern values) are supported by the data become tighter, since several disparate amplitudes must be matched self-consistently by the signal projected at each site. Consistency in the expected detected amplitude of an incoming wave between different sites can also further reduce localization regions. In general, having differing amplitude response from geographically-separated sites provides better localization, as was notable for GW170817 (Abbott et al., 2017b). For a given network configuration, it is possible to extract the expected error region from

the Fisher information matrix as a timing-weighted sum over the angles formed by the normal of the planes of each non-degenerate instrument triple and the wave propagation direction (Wen & Chen, 2010). Geographically, the placement of new instruments will have varying effects on localization, depending on location and orientation relative to the remainder of the network. Previous studies have examined the optimal placement of new instruments (Searle et al., 2006; Hu et al., 2015).

Localization also depends on source parameters, with BNS systems generally achieving better localization than NSBH systems. This is due to the frequency content of the signal, measured by its effective bandwidth. Effective bandwidth is the second noise-weighted moment in frequency of a source waveform (see Equation 2 of Fairhurst 2011b). Thus, sky localization for sources with equal SNR will change with differing effective bandwidth. NSBH systems typically have smaller effective bandwidths than BNS systems, due to more compact frequency content. Based on effective bandwidth alone, a canonical NSBH system ($1.4\ M_\odot + 10\ M_\odot$) is expected to have 1.3^2 times larger localization error regions than their canonical BNS counterparts ($1.4\ M_\odot + 1.4\ M_\odot$), at equal SNR. However, effective bandwidth and SNR in isolation are not sufficient to fully describe the sky localization capabilities of a given network.

Other source parameters, such as spin, can further affect localization through the effective bandwidth. Large spin magnitudes, when their direction is orthogonal to the plane of the binary, shift the frequency content of the waveform relative to the non-spinning case (Bardeen et al., 1972; Reisswig et al., 2009). Thus the effective bandwidth is changed because this power now resides in a frequency region with different spectral sensitivity, changing the expected size of localization regions. The components of the

spin projected into the orbital plane also affect localization (van der Sluys et al., 2008; Raymond et al., 2009), but nominally through breaking degeneracies in the parameter space, rather than through the effective bandwidth.

2.3. Posterior Sampling and Event Population

A fixed set of simulated gravitational-wave events is analyzed in three different detector configurations: HLV, HKLV, and HIKLV. All event properties are left unchanged between each network configurations. We employ `LALinference_mcmc` (Veitch et al., 2015), one of the standard MCMC samplers developed within the LVC to produce Bayesian posteriors of binary waveform properties. To ensure that the effect of correlation with other source properties is accounted for, we sample all source properties and orientation parameters. However, only the sky area is examined in detail. We refer the reader to Gaebel & Veitch (2017) for how accurately other properties such as masses and spins would be measured with additional detectors. As with previous studies, our simulations are performed noise-free to separate the localization uncertainties from effects arising from realizations of the noise (Rodriguez et al., 2014; Berry et al., 2015). All instruments are assumed to have identical advanced LIGO design sensitivity curves (Aasi et al., 2015) with the exception of Virgo which assumes its own advanced Virgo curve (Acernese et al., 2015; Patricelli et al., 2016).

2.3.1. Neutron Star – Black Hole Binaries

We make use of a population of NSBHs, with waveforms modeled using the `IMRPhenomPv2` (Hannam et al., 2014) family. Previous localization studies addressing NSBHs assume

fixed masses and neglect spin. Known XRBs, one of the most likely evolutionary paths of NSBH, have a handful of mass and spin measurements (Farr et al., 2011; Fragos & McClintock, 2015; Corral-Santana et al., 2016). While a detailed population analysis is beyond the scope of this work, the values measured span the range explored here. Therefore, in the absence of well measured population statistics, we note that uniform distributions are plausible and have the additional advantage of mapping reasonably well on to the priors adopted by gravitational-wave parameter estimation (Veitch et al., 2015). Masses are drawn from a uniform distribution between 5 – 30 $M_{\odot}$ for BH and 1 – 3 $M_{\odot}$ for NS. The black hole spin is distributed isotropically with dimensionless magnitudes ($a = |S/m^2|$) uniform up to 0.99. The population is selected to represent a plausible set of detections with the three-instrument HLV network, described in Pankow et al. (2017). The set of posteriors from Pankow et al. (2017) are used for the HLV network studies, without modification.[1]

2.3.2. Binary Neutron Stars

When comparing the effect of source properties, BNS populations should have less variation in sky localization: their mass ranges are narrower — thus leading to less variation in effective bandwidth — and their spins are not expected to be high enough to induce measurable precessional effects (i.e. Abbott et al., 2016b). It is unlikely that other properties, such as tidal deformability are significant enough to affect sky localization. As BNS localization is addressed in several previous studies, we restrict our study to only three representative BNS systems, each with different spin magnitudes but consistent

[1]In Pankow et al. (2017), five configurations of fixed parameter sets were examined. In this work, we use the posteriors with no fixed source parameters.

masses (1.4 $M_\odot$ + 1.4 $M_\odot$). We examine three different spins: zero-spin, component spin magnitudes equal to the largest spin measured in a binary of NS with dimensionless spin magnitude $a = 0.05$ (Kramer & Wex, 2009), and spin magnitudes near the fastest observed neutron star spin at $a = 0.4$ (Freire et al., 2008).[2] In all cases, the spin direction is oriented in the plane of the binary to capture the range of variation induced in the waveform by the precessing spins. Each system is then scaled to distances corresponding to SNR of 12, 14, 16, and 20 to simulate various potential detection ranges over each network configuration.

2.4. Results

The following sections present the resultant credible regions for the transition between HLV to HKLV and HKLV to HIKLV. It is important to recall that this is equivalent to viewing the same population of events, but with additional instruments added to the network. In general, this means that the SNR of each event receives contributions from additional instruments. The overall improvement in sky localization is thus split between both the increase in SNR (which improves the timing uncertainty measurement in the network) as well as the additional constraints added by amplitude and phase consistency over the network.

When visualizing distributions which would nominally be shifted across the sky by the Earth's rotation, we instead use Earth-fixed coordinates. This is achieved by aligning the zero of the right ascension with the prime meridian to represent sky alignment with the Earth at the event time. This representation highlights any correlations between sky

[2]Both NS spin superlatives were valid at the time of publication.

localization size and network orientation which is necessarily fixed to the frame of the Earth.

2.4.1. Neutron Star – Black Hole Binaries

The panels in Figure 2.1 show the transition in sky localization capability for the same set of NSBH events realized in each detector configuration. Specifically, the top panel in Figure 2.1 shows the same events in the transition from LIGO-Virgo to LIGO-KAGRA-Virgo. The improvement in sky localization is universal.

The bottom panel of Figure 2.1 shows a similar transition as the LIGO-India detector is activated. Here, the decrease is less noticeable as arc-like regions have already been reduced to more symmetrical ellipses. The best improvement is now apparent over the Indian Ocean, northeast of Australia, as well as a continued decrease in error region size over the equator in the Pacific. This effect is due to the geographic location of LIGO-India, as these events would be nearly directly overhead and thus well oriented for detection.

We compare our NSBH localizations to the expected sky localizations according to Equation 41 in Wen & Chen (2010) in Figure 2.2, finding generally consistent results. The histograms indicate the median and 90% credible intervals for each network configuration of these events, which are also recorded in Table 2.1. The notable scatter between expectation and reality may arise from systematic underestimation, particularly at low SNR where assumptions inherent to the analytic approximations break down (Vallisneri, 2008). Overall, the median and 90% intervals decrease by a factor of about three between the three- and four-detector transitions and a factor of two as a fifth detector is added. We also explore the relationship between network SNR and sky localization for HKLV and

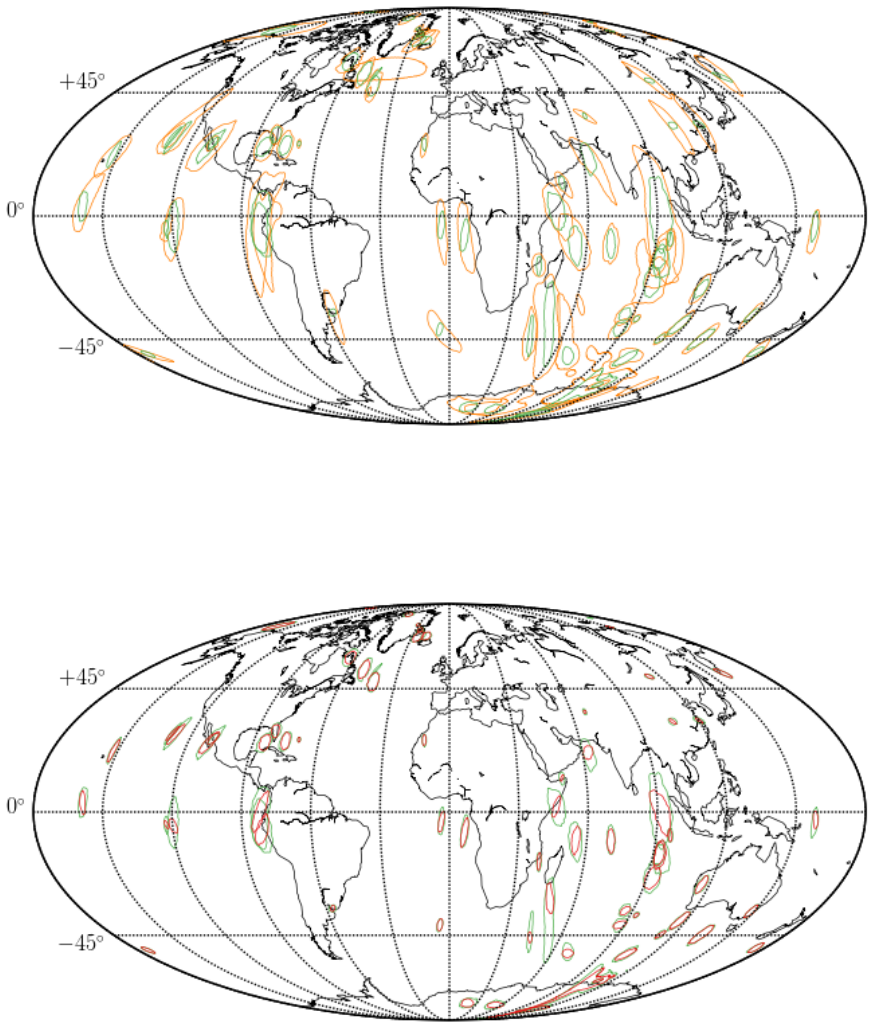

Figure 2.1. *Top:* 90% credible regions for NSBH sky localization with the HLV (orange) and HKLV (green) networks plotted on the sky in an Earth-fixed geographic coordinate frame. *Bottom:* Same, but for the HKLV (green) to HIKLV (red) transition.

HIKLV configurations in Figure 2.2, recovering the expected relationship as suggested in Berry et al. (2015).

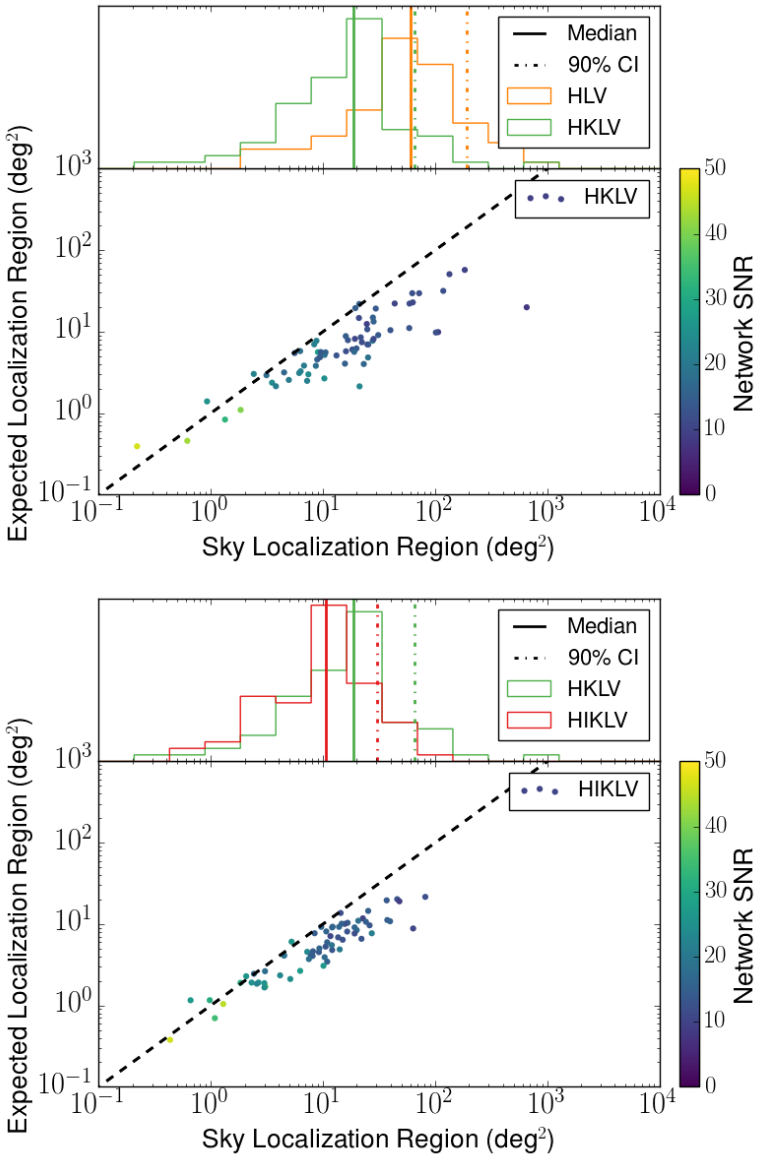

Figure 2.2. *Top:* scatterplot and histogram of 90% credible regions for NSBH sky localization. The histogram shows the distribution of sky localizations for both HLV (orange) and HKLV (green) detector networks. The scatterplot displays localization of all NSBH events in the HKLV network, along with the expected sky localization according to Equation 41 in Wen & Chen (2010). Events are colored by their network SNR. For comparison purposes, a dashed line is displayed for equal expected sky localization error region and computed sky localization error region. *Bottom:* Same, but for the HKLV (green) to HIKLV (red) transition. The scatterplot now contains events in the HIKLV network.

	HLV	HKLV	HIKLV
50%	60	19	11
90%	193	66	30

Table 2.1. Summary of 50% (median) and 90% fractions of the 90% credible regions for the NSBH event study. Values are represented in units of square degrees.

	HLV			HKLV			HIKLV		
SNR	0	0.05	0.4	0	0.05	0.4	0	0.05	0.4
12	74	80	80	30	34	34	12	13	12
14	43	56	58	21	21	22	9.3	8.1	9.0
16	37	35	45	15	13	15	6.1	5.8	5.9
20	22	24	24	8.0	7.8	8.3	3.1	3.8	3.9

Table 2.2. The 90% localization region values for BNS runs in square degrees. Each set of three columns corresponds to a network configuration (top), and a component spin magnitude (below network). Each row corresponds to the same event with a distance adjust such that the SNR values are 12, 14, 16, and 20.

2.4.2. Binary Neutron Stars

The resulting localization regions for the full parameter set BNS study are displayed in Figure 2.3 for all considered spin configurations. We recover the expected scaling of sky localization areas with SNR. In general, there is no discernible difference between signals with zero and non-zero spin when considered at the same SNR and network configuration. While only one sky location has been examined, we expect similar results for most BNS signal parameters, scaled appropriate by sky location. Table 2.2 contains a full list of localization areas at 90% credibility.

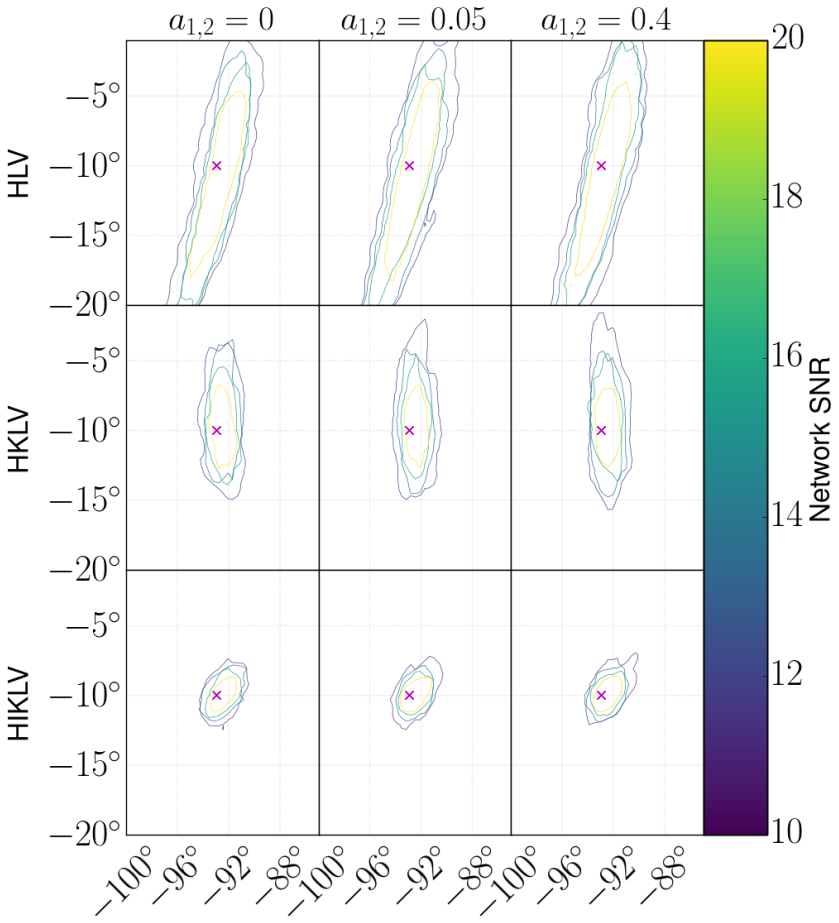

Figure 2.3. The 90% localization regions for a canonical BNS system (1.4 $M_\odot$ + 1.4 $M_\odot$) at each of the three network configurations and spin magnitude values. Superimposed in each panel are the localization regions at different network SNRs (12, 14, 16, and 20). Networks HLV, HKLV, and HIKLV are read top to bottom, and spins start on the left, iterating through 0, 0.05, and 0.4. Spin configurations examined here have little influence on the region size and shape.

Fairhurst (2011b) predicts a localization region size between 10 and 150 deg^2 for a canonical BNS event in the HLV network with a reference SNR near 14. We obtain a value of 43 deg^2, near the median of areas predicted in Fairhurst (2011b), for our

comparable zero-spin and SNR of 14 localizations in the HLV configuration. As KAGRA is added to the network[3], Fairhurst (2011b) predicts localization regions to shrink to between 4 and 22 deg^2. We recover a localization region around 21 deg^2 for the HKLV network, remaining broadly consistent with the predictions of Fairhurst (2011b). While the inclusion of LIGO-India was not examined in Fairhurst (2011b), we recover a median localization of 9.3 deg^2 for the HIKLV network.

2.4.3. Comparison With Previous Studies

We can compare our result to several studies of advanced network sky localization which have already been performed. We compared our results to those from analytic expectations of Wen & Chen (2010) and Fairhurst (2011b) throughout Sections 2.4.1 and 2.4.2, respectively. The expression used to calculate the expected error regions from Wen & Chen (2010) produces values which are consistent with both Fairhurst (2011b) and our studies. In addition, our study remains broadly consistent with the analytic results of Vitale & Zanolin (2011), recovering similar scalings in localization improvement for successive detector networks for a canonical BNS to our results in Table 2.2.

Studies such as Singer et al. (2014) have examined the sky localization capabilities of two- and three-interferometer networks of LIGO and LIGO-Virgo, using more realistic assumptions. In particular, they carried out an end-to-end study of the localizations from the outputs of one compact binary search pipeline used in the first two observing runs (Messick et al., 2017). They use a stream of data with colored, but Gaussian, noise and apply a minimum network SNR cut of 12 for each event. Singer et al. (2014)

[3]Note that Fairhurst (2011b) and most other previous studies refer to KAGRA as "J".

projected that Virgo would join the LIGO instruments during the second observation run at the sensitivity indicated in Abbott et al. (2016c). They examine a population of BNSs in the HLV configuration, obtaining a median sky localization of 235 $\deg^2$ at the 90% credible level. For our study of NSBH localization, we obtain a median sky localization of 193 $\deg^2$, seemingly contrary to the expectation that BNS sources are better localized than NSBHs. However, the detector networks in our study have better sensitivities over a given frequency range compared to Singer et al. (2014), leading to improvements in the effective bandwidth measured by a given instrument. So, our improved localization from that predicted by Singer et al. (2014) can be attributed to our use of 2018-era instruments as opposed to the less-sensitive 2016 configuration.

Rodriguez et al. (2014) resolve sky localization for a BNS population in which each event realizes a network SNR of 20. On the contrary, our NSBH study samples a wide distribution of network SNRs, meeting a minimum SNR threshold.[4] Therefore, our study probes the SNR regime at which detections are most likely to occur, while Rodriguez et al. (2014) ignores this low network SNR range. Nevertheless, our Figure 2.1 is qualitatively comparable to Figures 6 and 7 in Rodriguez et al. (2014). Particularly, the increased isotropy of a three- to four-instrument network and the subsequent, near-universal reduction of arc-like error regions to more compact forms are comparable.

Veitch et al. (2012) examine the improvement between the HLV and HKLV configurations for a set of 1.4 $M_\odot$ + 1.4 $M_\odot$ BNS events, distributed at a fixed distance but otherwise isotropically in orientation. Veitch et al. (2012) obtain a median sky localization of 10 $\deg^2$ at the 90% credible level with a four-site network, while for a similar network

[4]We require an SNR of at least 5.5 in the second-loudest detector.

we obtain a median of 19 deg^2 for our set of NSBHs. This increase in sky localization by a factor of 1.9 is consistent with the naïve expected improvement of $1.35^2 \approx 1.8$, based on the decrease of effective bandwidth as discussed in Section 2.2.

Nissanke et al. (2013b) track localization improvement for a set of 5 $M_\odot$ + 1.4 $M_\odot$ NSBH events, with non-spinning binary components. For a three-detector network, Nissanke et al. (2013b) recover a median localization of 50 deg^2 with a maximum localization of 170 deg^2 for all events studied. They recover an analogous five-detector median localization of 6 deg^2 with a maximum of 65 deg^2. These results are consistent with our NSBH localizations recorded in Table 2.1, with slight differences largely attributed to differences in NSBH mass and spin.

Chen & Holz (2016) examine a population of BNS in both a three instrument HLV as well as five instrument HIKLV configuration with a volumetrically and isotropically distributed population. Our fiducial event in the HLV configuration falls above their median for all SNRs, but is comparable for their median in the five instrument configuration, when the SNR 20 case is considered.

2.5. Electromagnetic Follow-Up

We can use the electromagnetic follow-up campaigns of GW150914 (Abbott et al., 2016d) and GW170817 (Abbott et al., 2017a) as examples of how the electromagnetic observation of a potential NSBH event would develop. The follow-up of GW150914 and GW170817 included several facilities which are likely to continue operation as the three-instrument network reaches design sensitivity. Potential electromagnetic counterparts to BNS and NSBH signals should be accessible to many of these instruments (see Chapter 4),

as the peak gravitational-wave emission exceeds the instruments' limiting sensitivities for both BNS (approximately $\sim$ 500 Mpc, $z \sim 0.1$) and NSBH (approximately $\sim$ 2 Gpc, $z \sim 0.4$ for a 10 $M_\odot$ + 1.4 $M_\odot$ merger) systems (Abbott et al., 2020a; Chen et al., 2021). If we are able to confidently separate the true source from a transient background, then the limiting factors under ideal conditions for electromagnetic counterpart identification become slew time, observation time, and FoV.

GW170817 was relatively nearby and well-localized, allowing a manageable area to be searched through electromagnetic campaigns. GW170817's localization lies well below the median expected localization for the second observing run (Abbott et al., 2016c) and near the median expected for the fully advanced LIGO-Virgo network (Veitch et al., 2012). Given the population of NSBHs in this work, it is likely that a NSBH source will lie further away than GW170817 (given the accessible volume of space for just the three-instrument network) and thus the sky localization will expand accordingly. If the cadence and FoV of current and upcoming telescopes are typical of follow-up instruments for NSBH events, prospects of joint detection before a fourth instrument activates will be challenging. Several of the current and upcoming wide field instruments, such as the Dark Energy Camera (Flaugher et al., 2015), Zwicky Transient Facility (Bellm et al., 2019), and the Vera Rubin Observatory's Legacy Survey of Space and Time (Ivezić et al., 2019), have FoVs between 1 deg^2 and 10 deg^2 while slew and observation times can vary significantly (see Table 4 in Cowperthwaite & Berger 2015). In the four- and five-detector era, NSBH sources will typically be localized to less than 20 deg^2, thus allowing these instruments to survey localization regions with a few to several pointings. Detection of an electromagnetic counterpart in these localization regions depends on several factors

including magnitude and observation time. Such factors will motivate optimal follow-up campaigns to search localization regions for possible multi-messenger sources.

2.6. Conclusions

We have made the first examination of the localization capabilities for a set of astrophysically-motivated NSBH events projected through the expected evolution of the advanced gravitational-wave network. When additional independent baselines are added, the coverage of the network becomes more isotropic and reduces 90% confidence regions drastically, sometimes by an order of magnitude between the three- and five-instrument networks. With the five-instrument network, there are few patches of the sky where sky localization would exceed 100 deg^2, and in some cases, the required search area is less than a few square degrees. NSBH sources are localized at the 90% credible region to a median of 60 deg^2 in the three-detector era. Analogous localization is reduced to 19 deg^2 in the four-detector era and 11 deg^2 with five detectors. Detected event populations tend to cluster in regions of the sky where the network response is most sensitive, and the antenna response of the HLV network is qualitatively different from HKLV and HIKLV. Adding an instrument can never decrease the localization capability, and broadly speaking, adding additional long baselines (specifically those added with Japan and India) provides the potential for better localization. However, localization capability is not necessarily correlated with network response — and hence where in the sky events are detected — so it does not immediately follow that the medians presented here are conservative. These improvements should facilitate complete and regular electromagnetic follow-up campaigns by many observatories at nominal coverage rates. The results presented here are in broad agreement with

both analytical treatments as well as previous studies which have addressed the question of BNS localization in late advanced detector eras and a variety of potential network configurations.

Finally, while we have pinned our studies to the fully advanced LIGO design sensitivity, it is likely that this will not be representative of the state of GW interferometry in the late 2020s. Particularly, it is possible that the five instrument network may have at least some of the interferometers in a so-called "A+" configuration which may add another factor of two or three to the ranges from the advanced LIGO/Virgo design sensitivity (Abbott et al., 2017g). If realized, these instruments will further improve sky localization capabilities with both increased SNR and narrower timing uncertainty.

2.7. Final Notes

This study was later expanded by Pankow et al. (2020), which uses a realistic population of NSBH events to infer sky localization regions. The authors model detector duty cycles, estimations a typical BNS sky localization of 28 deg^2 and NSBH sky localization of 50–120 deg^2 in the five-detector era.

CHAPTER 3

Mitigation of the Instrumental Noise Transient in Gravitational-Wave Detector Data Surrounding GW170817

In this chapter, I describe multiple strategies to remove and/or mitigate an instrumental noise transient coincident with an astrophysical signal in gravitational-wave interferometer data. I then quantify the effects of each mitigation method on astrophysical parameter estimation of both intrinsic and extrinsic source properties. This work was initially published in Pankow et al. (2018b) and has been updated to reflect recent changes in detection rate estimates and instrument timelines. This study was first conducted as part of the detection of GW170817 (Abbott et al., 2017b) and later adapted into a separate publication. This work demonstrates that astrophysical parameter estimates of GW170817 (Abbott et al., 2019b) were not biased by glitch mitigation. Similar glitch mitigation methods have since been used in the detection of eight GW candidate events in the first half of the third observing run (O3a; Abbott et al., 2021), including in the detection of BNS event GW190425 (Abbott et al., 2020b). All eight of these events rely on this study to confirm the accuracy of parameter estimates.

3.1. Introduction

The discovery of GW170817 (Abbott et al., 2017b) was a watershed moment in astrophysics. It was the first detection of a BNS through GWs, and its association with GRB170817A (Abbott et al., 2017c) spurred a world-wide effort which revealed emission

throughout the electromagnetic spectrum (Abbott et al., 2017a). The signal is the loudest GW event detected so far, exhibiting a total SNR of up to 33 (Abbott et al., 2019a).

Initially identified by low-latency compact binary searches (Messick et al., 2017; Nitz et al., 2018), coincidence and rapid localization (Singer & Price, 2016) were hindered because of a nonastrophysical transient present in the LIGO-Livingston detector about one second before the estimated merger time of the signal (Abbott et al., 2017b). This transient signal (colloquially referred to as a *glitch*; Nuttall et al., 2015; Abbott et al., 2016e; Davis et al., 2021) was a high-amplitude, short-duration excursion of unknown origin in the control loop used to sense the differential motion of the interferometer arms, which are calibrated to produce GW strain data (Aasi et al., 2015). This excursion caused an overflow in the digital-to-analog converter of the optic drive signal and prevented the searches from registering an event trigger for GW170817 in the LIGO-Livingston detector in low-latency. The cause of the excursion is unknown, but such *overflow* glitches occur independently at a rate of roughly once every few hours in both LIGO detectors (Abbott et al., 2018a).

After the signal was visually identified in both LIGO detectors, it was clear that the noise transient in LIGO-Livingston would need to be mitigated in order to provide accurate sky localization maps and estimate the parameters of GW170817.

Three types of glitch removal were employed. The first method excised 0.2 seconds of time series data corrupted by the noise transient using the PyCBC *gating* algorithm (Usman et al., 2016; Nitz et al., 2021). The second method is a variation on the first which allows for better fidelity in the process. The gating methods were developed in the context of detection, since glitches can corrupt the output of matched filtering searches (Usman

et al., 2016; Messick et al., 2017). They are applied in an automated processes which identify statistically significant excursions in the data stream and excise them. Cognizant that any electromagnetic counterpart was likely to fade on the order of hours to days (see Chapter 4), the first method of data excision was used to produce and promptly disseminate an accurate sky map for GW170817 (LVC, 2017). This resulted in the successful discovery of a counterpart electromagnetic signal (Arcavi et al., 2017; Coulter et al., 2017; Cowperthwaite et al., 2017; Lipunov et al., 2017; Tanvir et al., 2017; Valenti et al., 2017). However, while such data excision techniques are speedy to apply, portions of the underlying signal are also removed in the process. A third, more sophisticated, technique used the `BayesWave` algorithm (Cornish & Littenberg, 2015) to model the glitch and subtract it from the data, preserving more of the signal. The glitch-subtracted data, produced days after the initial detection, was used for parameter estimation (Abbott et al., 2017b) and more detailed studies of the signal properties (Abbott et al., 2018b, 2019b).

The focus of this work is to evaluate the efficacy and fidelity of these techniques — *gating* and `BayesWave` — in the context of characterization of the intrinsic properties of the signal. In our analysis we use the `LALInference` package (Veitch et al., 2015), a standard parameter estimation analysis for GW signals from compact binaries. This analysis models the signal with existing theoretical waveform templates and assumes that the noise is *stationary*, namely that its properties do not change appreciably on the timescale of the signal, and *Gaussian*, namely that the noise follows a colored Gaussian distribution. The presence of the noise transient in the data breaks both assumptions about noise behavior.

For a true GW source, such as GW170817, no control case is available for a glitch mitigation study; the true waveform and intrinsic source parameters are not known a priori. We circumvent this problem with a set of synthetic event injection studies, using data stretches which exhibit instrumental transients similar to the one afflicting GW170817. We inject synthetic GW170817-like signals concurrently with those noise transients and then apply the transient removal methods. We then recover the signal parameters, and compare the known properties of the injected synthetic signal to the posterior distributions obtained by analyzing the data with and without the subtraction procedure applied. As a reference, we also perform the same parameter estimation analysis with a zero-noise realization. This provides an ideal case for comparison with the real-noise analyses.

We find that modeling and subtracting the glitch using the `BayesWave` algorithm leads to robust and unbiased estimation of the parameters of the signal, including the masses, spins, and tidal deformabilities of the binary components. The latter is particularly relevant in the case of GW170817. The tidal deformability quantifies the deformation of a body in the presence of an external field (Flanagan & Hinderer, 2008) and depends sensitively on the equation of state of matter at supranuclear densities (Hinderer, 2008; Hinderer et al., 2010). Since it affects the binary evolution mostly during the latest stages (Read et al., 2009) of its evolution, its main effect on the waveform temporally coincides with the glitch in the data (which, as mentioned above, happened roughly 1 second before the estimated merger time). Despite this, we show that the measurement of the tidal deformability presented in Abbott et al. (2017b), Abbott et al. (2018b), and Abbott et al. (2019b) are only minimally affected by the glitch once it has been successfully modeled and removed.

3.2. Mitigation Techniques

In the presence of a nonastrophysical transient and a GW signal, the measured strain time series can be expressed (Finn & Chernoff, 1993; Flanagan & Hughes, 1998) as

$$s(t) = n(t) + h(t, \vec{\lambda}) + g(t, \Delta t)\,. \tag{3.1}$$

In the above equation $n(t)$ is a stream of stationary and Gaussian noise, $h(t)$ is the GW signal that depends on the binary parameters $\vec{\lambda}$ (Allen et al., 2012), and $g(t)$ is the non-Gaussian, instrumentally-induced transient of duration Δt. The spectral profile of the noise is characterized by the one-sided PSD denoted $S(f)$. The detection and parameter estimation algorithms make explicit assumptions about the nature of the data — namely that the Fourier transform of $n(t)$, $\tilde{n}(f)$ is related to the PSD by $2\langle\tilde{n}(f)\tilde{n}^*(f')\rangle = S(f)\delta(f - f')$. In other words, the noise is stationary and Gaussian distributed, given its ensemble average in the Fourier domain is proportional to the spectral density (Sathyaprakash & Schutz, 2009).

In the context of GW parameter estimation both of these assumptions determine the form of the log-likelihood function for the data, given a model for the GW signal $h(\vec{\lambda}')$ (Veitch et al., 2015), defined as:

$$\log L(s|\vec{\lambda}') \propto \langle\tilde{s} - \tilde{h}(\vec{\lambda}')|\tilde{s} - \tilde{h}(\vec{\lambda}')\rangle. \tag{3.2}$$

where the quantities with a tilde are the Fourier-domain transformed quantities from the time-domain equivalents in Eq. (3.1). The brackets denote a noise-weighted inner-product defined as $\langle a|b\rangle \equiv 4\Re\int_0^\infty \tilde{a}^*\tilde{b}/S(f)df$.

Eq. (3.2) is calculated from the residual after subtracting the expected signal $\tilde{h}(\vec{\lambda}')$ from the data $\tilde{s}$. In the presence of a glitch, the residual consists of both Gaussian noise and the instrumentally-induced transient. Moreover, the parameters of the signal can be severely biased as the analysis attempts to return residuals that are consistent with our assumption of Gaussian noise. The intrinsic amplitude of the glitch relative to the Gaussian noise sets the scale of the mismatched residual (e.g. with which h can g be matched), and if the glitch is comparable in SNR relative to the signal, it can overwhelm the likelihood calculated for the signal alone (Powell, 2018). We next describe strategies to mitigate glitch-induced biases by removing the glitch from the data, $s(t)$, with minimal impact of the recovered signal.

3.2.1. Frequency-independent subtraction

The initial solution to mitigating the noise transient near GW170817 was to smoothly taper the time series data to zero while the glitch was present (Usman et al., 2016; Nitz et al., 2021), see Figure 2 of Abbott et al. (2017b),

$$W(t) = [1 - w(t, t_0, t_w, t_{\rm taper})] \ . \tag{3.3}$$

In the above a windowing function w — typically a Tukey window — is applied around the center of the noise transient time t_0. The shape of the window is set by t_w, the half-duration of the data to zero out, and $t_{\rm taper}$, the duration of the Tukey tapering on each side of the gated data. For GW170817, $t_0 = 1187008881.389$, $t_w = 0.1s$, and $t_{\rm taper} = 0.5s$. The duration of the data affected by the gating window $\Delta t = 2t_w + 2t_{\rm taper}$ (Abbott et al., 2017b). Clearly, this also removes the signal $h(t)$ during Δt from the data series.

Therefore, while this method is effective in removing the high amplitude power in the glitch, it might induce a different bias because the signal waveform template would also need to be windowed in the same way to match optimally. Section 3.3.1 shows that, for a zeroed time window of $2t_w = 0.25$ seconds or less, this bias is within the tolerances set by the uncertainties in the posterior distributions for a preliminary analysis, and so the trade-off is acceptable.

3.2.2. Time-frequency area subtraction

A similar, but *frequency-dependent* solution was developed to further reduce damaging the fidelity of the noise-transient-subtracted data, $s'(t)$:

$$s'(t) = s(t) - g_{\mathrm{TFA}}(t, t_0, \Delta t, \Delta f)\,, \tag{3.4}$$

where $g_{\mathrm{TFA}}(t, t_0, \Delta t, \Delta f)$ is the glitch estimate produced by the time-frequency area (TFA) algorithm.

The TFA algorithm starts by band-passing the data around the noise transient in the frequency band effected by the glitch (e.g., 50 to 800 Hz). This is done in the time-domain after detrending and windowing the time series.

The FFT of the band-passed data is then computed, and the amplitudes of frequencies corresponding to known strong features (e.g., calibration lines) are set to zero. If desired, additional band-passing can also be done in the frequency domain by setting the amplitude of out of band frequencies to zero as well. For the results presented here, frequencies near 300 Hz and 500 Hz were set to zero to remove strong narrow lines due to injected

calibration lines and mechanical resonances (Abbott et al., 2016e), and frequencies above 700 Hz were zeroed to improve the band-pass filtering.

Finally, the band-passed and line-removed frequency-domain data are converted back to the time domain with an inverse FFT operation, and the glitch estimate $g_{\mathrm{TFA}}(t, t_0, \Delta t, \Delta f)$ is produced by windowing this time series around the time of the glitch. The Tukey window function, which is equal to 1 in the central region, is used throughout the TFA algorithm to ensure that the amplitude of the deglitched time series is not modified by the windowing operation.

3.2.3. Noise-transient fitting and removal

Apart from generic considerations about the duration and bandwidth of the noise transient, the methods described in Secs. 3.2.1 and 3.2.2 are mostly agnostic to the morphology of the transient itself. They are expedient to apply, and significantly reduce biases in the recovered signal parameters. However, the signal is still modified in some way because of the excision applied. A more sophisticated treatment can be applied if one considers the coherent and incoherent decompositions of the data from the two instruments. While a true GW signal is *coherent* across the detector network, any instrumentally-induced transient is *incoherent*, assuming that the noise in the various detectors is uncorrelated. The morphology-independent algorithm `BayesWave` (Cornish & Littenberg, 2015) exploits this distinction to reconstruct any coherent and incoherent power in the detectors through a continuous wavelet basis. `BayesWave` uses Morlet-Gabor wavelets, with morphologies

$$\Psi(t; A, f_0, \tau, t_0, \phi_0) = Ae^{-(t-t_0)^2/\tau^2} \cos\left[2\pi f_0(t-t_0)+\phi_0\right] \tag{3.5}$$

to simultaneously model both the coherent signal and the incoherent noise transient in Eq. (3.1). Each wavelet depends on five parameters: its amplitude A, quality factor $Q \equiv 2\pi f_0 \tau$ (where τ is the wavelet duration), central frequency f_0, central time t_0, and phase ϕ_0.

`BayesWave` harnesses the inherent efficiency of Bayesian inference (Cornish & Littenberg, 2015). When a signal is coherent across the detector network it can be fully described in all detectors by the same set of Morlet-Gabor wavelets plus four extrinsic parameters characterizing its sky location, polarization, and the ratio of the two independent GW polarization amplitudes (ellipticity). An incoherent signal, on the other hand, can only be reconstructed with independent sets of wavelets in each detector. Since the incoherent model (termed the "glitch model" in `BayesWave` literature) has more parameters ($5N_dN$, where N_d is the number of detectors and N the number of wavelets) than the coherent model ($5N + 4$, usually referred to as the "signal model"), the latter will be preferred assuming both models fit the data equally well (Veitch & Vecchio, 2010). Any coherent signal can be separated from the incoherent power, as it can be modeled with fewer parameters (Kanner et al., 2016).

In practice and for the signal and glitch near GW170817, this process is aided by the fact that a BNS inspiral and an overflow glitch are reconstructed by wavelets of largely different quality factors, Q. A BNS signal is characterized by a long duration (of order seconds to minutes), and is therefore best modeled by wavelets with a large quality factor. On the contrary, the glitch has a short duration and a more compact time-frequency signature, which is best recovered with wavelets with a small quality factor.

Once the coherent and the incoherent part of the signal have been simultaneously reconstructed, the incoherent portion of the data is subtracted from the individual instrument data streams. The instrumental transient — present only in the LIGO-Livingston detector — is removed while the coherent GW signal is only minimally affected, giving

$$s'(t) = s(t) - g_I(t), \tag{3.6}$$

where $g_I(t)$ is `BayesWave`'s reconstruction of the incoherent part of the data.

In effect, `BayesWave` fits for the shape of $g(t)$ while leaving $h(t)$ and $n(t)$ unaffected in Eq. (3.1). As a consequence, the assumptions of stationary and Gaussian residuals once the GW signal has been subtracted are explicitly restored and normal parameter estimation techniques are applicable. We show in Section 3.3.2 that this procedure leads to negligible biases in the parameters of the signal.

3.3. Signal Characterization

The *overflow* glitch described in Section 3.1 preceded the merger time of GW170817 in the LIGO-Livingston instrument by about 1.1 seconds. As a result, the signal was originally only identified in the LIGO-Hanford detector. In addition to automated monitors (Biswas et al., 2013; Essick et al., 2013), manual checks and visual inspections of the data revealed both the glitch in LIGO-Livingston and the coincident nature of the signal. The glitch intersected the time-frequency track of the merger signal, immediately revealing the need to mitigate the impact of the glitch. In order to produce a timely alert of the event to partner astronomers, the frequency-independent data excision method of Section 3.2.1 was used to generate a rapid sky position posterior. On longer timescales,

the methods in 3.2.2 and 3.2.3 were applied, and ultimately, the final results presented in Abbott et al. (2017b), Abbott et al. (2018b), and Abbott et al. (2019b) used the data set produced with the method in 3.2.3.

In this section, we compare the performance and fidelity of methods 3.2.1, 3.2.2, and 3.2.3 by injecting synthetic signals with parameters comparable to GW170817 in data from the two LIGO detectors. In Section 3.3.1 we compare the effect of glitch-mitigation methods of Secs. 3.2.1, 3.2.2, and 3.2.3 on a simulated signal in the absence of a glitch. Since the data are completely excised, the absence of a glitch is irrelevant to the investigation of the two gating methods. The use of `BayesWave` glitch-removal method on data where there is no glitch present should meanwhile change the results very little, which we confirm. We then explore the performance of `BayesWave` glitch removal in the analysis of signals injected on top of actual instrumental glitches in 3.3.2. For all the analyses of this section the PSD is calculated from on-source data with the technique presented in Littenberg & Cornish (2015). We also marginalize over the calibration uncertainty of the detector as explained in Farr et al. (2015). For simplicity, we assume priors on the the amplitude (phase) marginalization spline points of 5% (3°).

3.3.1. Comparison of Mitigation Methods

In this subsection, we study the effect of the three glitch-mitigation methods described in Section 3.2 on source characterization. We select a time less than a half-hour after GW170817 in a contiguous set of data and hence preserve the state of the instruments as closely as possible and add a simulated GW170817-like signal to the data, using the `IMRPhenomPv2` waveform family, see Section 3.3.2. For this specific time, no glitch was

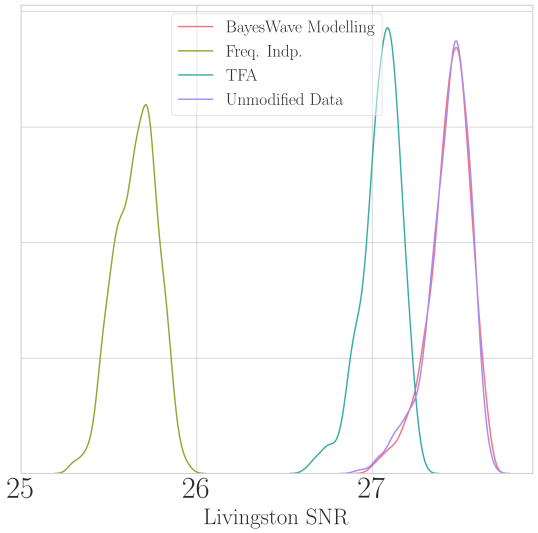

Figure 3.1. Comparison of mitigation methods on posterior density function of SNR in LIGO-Livingston. The posteriors are computed after applying the frequency-independent excision method of Section 3.2.1 (yellow, "Freq. Indp."), the frequency-dependent excision method of Section 3.2.2 (purple, "TFA"), after modeling and subtracting the glitch as described in Section 3.2.3 (pink, "BayesWave Modelling"), and when analysing the signal without any additional modification (green, "No Gating"). The two excision methods lead to decreases in SNR, while BayesWave preserves the SNR.

present within the duration of the simulated signal. The methods from 3.2.1, 3.2.2, and 3.2.3 were applied to the simulated signal in exactly the same manner and temporal offset relative to GW170817.

In particular, understanding the consequences of the two glitch excision methods (Secs. 3.2.1 and 3.2.2) is important since the methods are straightforward and quick to apply, and will likely continue to be used for rapid response to interesting GW events, especially as the detection rate increases and the probability of signals overlapping with glitches rises. The initial data excision is expected to impact the extracted parameters depending on the intersection of the excision and time-frequency track of the signal. In

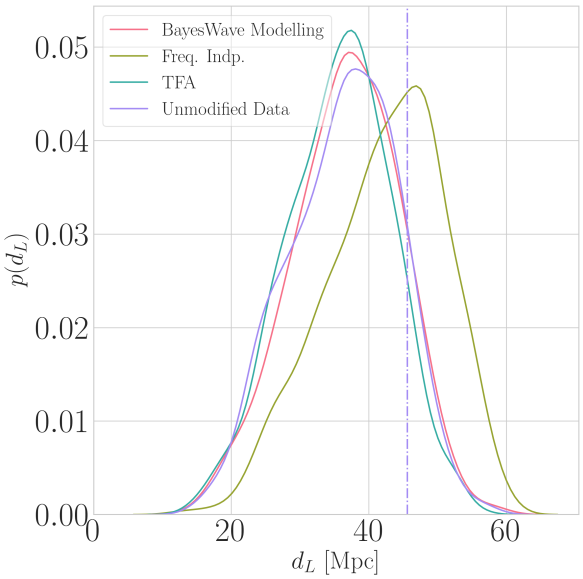

Figure 3.2. Comparison of mitigation methods on posterior density function of the source's luminosity distance. The vertical dot–dashed line indicates the known, injected distance of the source.

the case of GW170817, the intersection point of the track with the excision is relatively close to the merger time; the fixed time interval in between the glitch peak time and the signal implies the intersection point in the time-frequency plane is near $\sim$ 100 Hz. As a result, the sweep of the signal through the most sensitive part of the instrument bandwidth — where many physical effects are most well measured — could be affected. While the mass parameters are typically well measured from lower frequencies, the effects of spin and tidal parameters on the waveform phasing begin to become measurable in this region. Relative to the length-in-band of GW170817 ($\sim$ 100 s from 25 Hz to merger), the glitch duration is small (the overflow itself is less than 5 ms), as is the excision duration ($\sim$ 0.5 s). Ideally, handling this excision would require a modification of the signal template to similarly excise the portion of the signal which is removed with the data. While

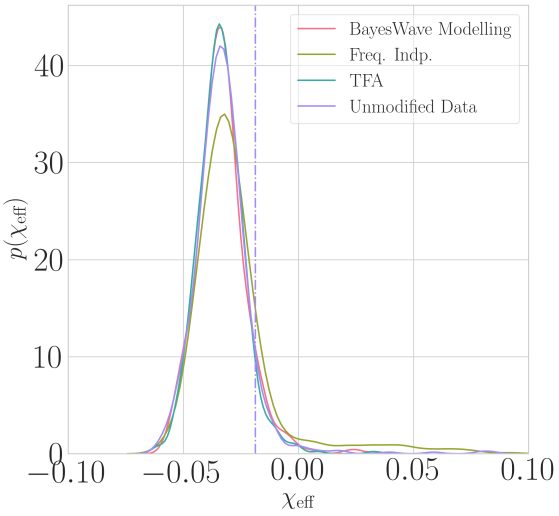

Figure 3.3. Comparison of mitigation methods on posterior density function of the effective spin parameter (Racine, 2008). The vertical dot–dashed line indicates the known, injected effective spin parameter.

not conceptually complex, adding this capability to the existing low-latency GW searches would increase computational costs.

For this example, no significant glitching is present near the merger time of the injection. The methods in Section 3.2.1 and 3.2.2 each remove a fixed time-frequency volume from the data, and so the impact on the SNR of the signal should be the same with or without a glitch present. For the `BayesWave` method in Section 3.2.3, the absence of a glitch means that only a small amount of power is expected to be removed in this case. Comparisons between the different glitch-mitigation methods are displayed in Figures 3.1-3.4. We present posterior distributions for numerous parameters of an signal injected for the various mitigation techniques presented in Section 3.2, The SNR computed from data s and template $h(\vec{\lambda}')$ is proportional to $\langle \tilde{s} | \tilde{h}(\vec{\lambda}') \rangle$, and as such, it is clear that removing

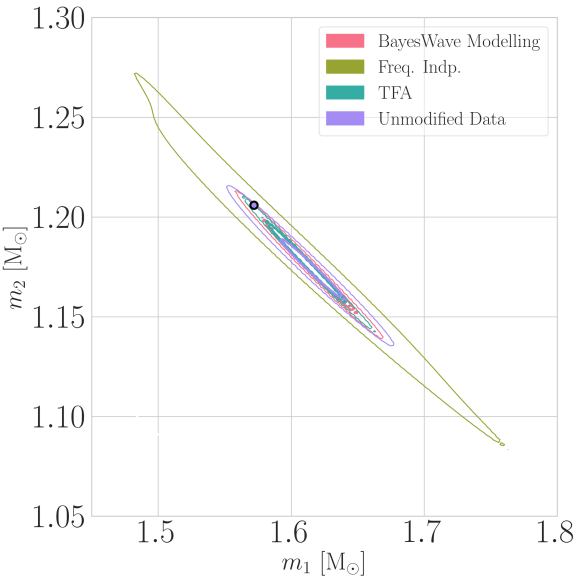

Figure 3.4. Comparison of mitigation methods on two-dimensional posterior density functions of the primary and secondary component masses. The scatterpoint indicates the injected component masses. The width of the posterior distribution directly relates to the recovered SNR.

some part of s will incur a systematic reduction in the SNR distribution over the parameter set. This effect is apparent as the SNR distribution in the LIGO-Livingston data is reduced by about two units ($\sim 7\%$) in the case of frequency-independent data excision and less than one unit ($\sim 2\%$) for the frequency-dependent subtraction method (Figure 3.1). The distance distribution is similarly modified as it is inversely proportional to the SNR, and the event appears to be slightly further away than in reality (Figure 3.2). On the contrary, the SNR and distance distributions after the application of the `BayesWave` glitch subtraction are very similar to the ones obtained when the signal is injected but otherwise unmodified. This is the expected behavior, since there is no glitch to remove.

In Figure 3.3, we show the effect of excision methods on the recovered one-dimensional posterior on the effective spin parameter, $\chi_{\rm eff}$,[1] while Figure 3.4 shows the recovered detector-frame component masses. The two dimensional marginalized posterior for the component masses shows that mass posteriors derived from different mitigation methods are broadly consistent with each other and give similar credible intervals along the small axis (chirp mass) of the posterior ellipse. However, the data excision methods lead to mass posteriors that encompass a broadened set of component masses and mass ratios.

This difference in the mass ratio estimate could affect the measurement of the spin parameters, due to the well-known spin-mass correlation (Cutler & Flanagan, 1994). Indeed, the posteriors for the effective spin parameter, shown in Figure 3.3, exhibit a minor tail in the posteriors derived from excised data, reflecting the larger mass ratio uncertainty exhibited by the frequency independent and TFA excision data.

Overall, we find that both data excision methods recover a smaller SNR and, in the case of the frequency-independent method, can introduce small parameter biases, which are largely absent when the glitch is modeled and removed. These simple excision methods are an appealing option for quick glitch mitigation, due to their applicability to a large range of glitch morphologies, especially when rapid sky-localization is necessary. However, for follow-up studies the glitch-fitting method seems preferable, since it never introduce biases, and can deal with cases where the glitch is of comparable length to the signal. In the next section we examine the performances of the glitch-fitting method using simulated signals.

[1]The effective spin parameter is the mass-weighted sum of the binary components' spins along the orbital angular momentum (Racine, 2008) and one of the best measured spin combinations with GW data.

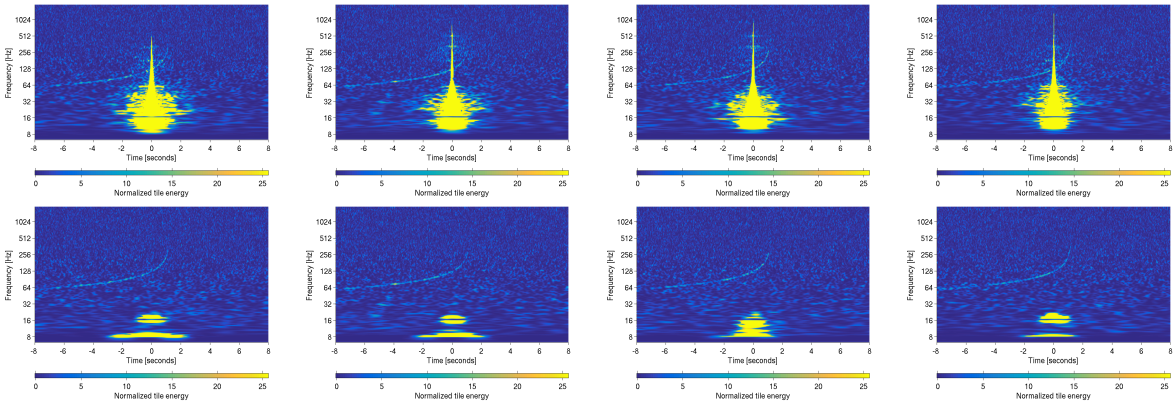

Figure 3.5. Normalized signal amplitude (color axis) in the Livingston instrument for four synthetic events added to real interferometric data, as examined in a time-frequency representation. The top row is before the glitch-mitigation is applied, and the bottom row is after we have modeled and removed the glitch with `BayesWave`. The simulated chirping signal is clearly visible in the background of all. The glitch extends in frequency below the lowest frequency used in either the glitch fitting and removal or the parameter estimation procedures, and as such was not completely removed. However, since those frequencies are excluded from the analyses, the result is unaffected by the remaining glitch power.

3.3.2. Efficacy and Veracity of Transient Removal

In the previous subsection we demonstrated that simple data excision techniques can lead to rapid source characterization with a tolerable degree of parameter biases. However, the recovered signal SNR is decreased, which implies that useful information about the signal has been lost. In this section we study in more detail the technique presented in Section 3.2.3, which attempts to fit the glitch and remove it while preserving the underlying signal and the Gaussian detector noise.

We produce GW170817-like signals and add them to the data of the LIGO-Livingston detector around four overflow glitches. To produce the signals we use the `IMRPhenomPv2` (Hannam et al., 2014; Schmidt et al., 2015; Husa et al., 2016; Khan et al., 2016) and

Glitch GPS time		True Value	Recovered Values: Zero-Noise	No Mitigation	With Mitigation
Event 1 (1186164816)	m_1 [$M_\odot$]	1.64	$1.64^{+0.24}_{-0.23}$	$24.44^{+2.62}_{-0.92}$	$1.64^{+0.25}_{-0.23}$
	m_2 [$M_\odot$]	1.16	$1.16^{+0.18}_{-0.13}$	$2.79^{+0.20}_{-0.92}$	$1.16^{+0.17}_{-0.14}$
	q	0.71	$0.70^{+0.24}_{-0.16}$	$0.11^{+0.02}_{-0.03}$	$0.70^{+0.23}_{-0.17}$
	$\chi_{\rm eff}$	0.007	$-0.01^{+0.04}_{-0.02}$	$0.38^{+0.02}_{-0.69}$	$-0.01^{+0.05}_{-0.03}$
	Λ_1	0	-	-	-
	Λ_2	0	-	-	-
Event 2 (1186691156)	m_1 [$M_\odot$]	1.38	$1.64^{+0.26}_{-0.24}$	$61.19^{+0.17}_{-0.96}$	$1.60^{+0.29}_{-0.20}$
	m_2 [$M_\odot$]	1.37	$1.16^{+0.19}_{-0.14}$	$8.19^{+0.07}_{-0.13}$	$1.19^{+0.16}_{-0.17}$
	q	0.99	$0.71^{+0.26}_{-0.17}$	$0.13^{+0.00}_{-0.00}$	$0.75^{+0.22}_{-0.20}$
	$\chi_{\rm eff}$	0	$0.04^{+0.05}_{-0.03}$	$0.88^{+0.00}_{-0.01}$	$0.02^{+0.05}_{-0.02}$
	Λ_1	275	193^{+529}_{-180}	1429^{+45}_{-14}	248^{+568}_{-227}
	Λ_2	309	503^{+1516}_{-467}	2621^{+2051}_{-2222}	668^{+1395}_{-599}
Event 3 (1186885739)	m_1 [$M_\odot$]	1.38	$1.60^{+0.28}_{-0.21}$	$40.18^{+0.44}_{-0.14}$	$1.59^{+0.28}_{-0.19}$
	m_2 [$M_\odot$]	1.37	$1.18^{+0.17}_{-0.16}$	$6.17^{+0.04}_{-0.07}$	$1.20^{+0.16}_{-0.17}$
	q	0.99	$0.74^{+0.23}_{-0.19}$	$0.15^{+0.001}_{-0.001}$	$0.75^{+0.21}_{-0.20}$
	$\chi_{\rm eff}$	0	$0.02^{+0.05}_{-0.03}$	$0.33^{+0.02}_{-0.02}$	$0.01^{+0.05}_{-0.02}$
	Λ_1	1018	588^{+1084}_{-525}	4958^{+40}_{-144}	645^{+1070}_{-574}
	Λ_2	1062	1566^{+2461}_{-1411}	$5.00^{+1.01}_{-1.40}$	1545^{+2420}_{-1382}
Event 4 (1186300855)	m_1 [$M_\odot$]	1.68	$1.63^{+0.25}_{-0.23}$	$38.71^{+0.08}_{-0.05}$	$1.62^{+0.26}_{-0.22}$
	m_2 [$M_\odot$]	1.13	$1.16^{+0.18}_{-0.14}$	$5.80^{+0.02}_{-0.02}$	$1.17^{+0.17}_{-0.15}$
	q	0.67	$0.71^{+0.25}_{-0.17}$	$0.15^{+0.001}_{-0.001}$	$0.72^{+0.23}_{-0.18}$
	$\chi_{\rm eff}$	0	$0^{+0.04}_{-0.03}$	$0.33^{+0.01}_{-0.01}$	$-0.01^{+0.04}_{-0.02}$
	Λ_1	77	240^{+605}_{-220}	4991^{+8}_{-27}	211^{+576}_{-193}
	Λ_2	973	728^{+1686}_{-668}	$0.14^{+0.02}_{-0.03}$	591^{+1502}_{-539}

Table 3.1. Properties of the four simulated signals analyzed. The first column gives the GPS time of the overflow glitch around which we make the BNS injections; the second column list the binary parameters we study; the third column gives they injected (true values). The remaining three columns give the median recovered value for each parameter, as well as the 90% credible intervals in the case of a zero-noise-realization injection (fourth column), a parameter estimation analysis on data that include the glitch (fifth column) and on data obtained after glitch mitigation with `BayesWave` (sixth column).

the `TaylorF2` (Damour et al., 2002), including tidal corrections (Vines et al., 2011), waveform models[2] and we place the signals with end times 1.2 seconds after the time assigned to the Livingston overflow glitch we are studying. Table 3.1 provides details for these simulated signals. We follow the same procedure from Abbott et al. (2017b) in applying `BayesWave` to model and subtract the glitch from the Livingston data following the method described in Section 3.2.3. Figure 3.5 shows the time-frequency representation of each glitch together with the simulated signal before and after glitch subtraction. The simulated signal is clearly visible as a characteristic "chirp" in both cases.

We then perform a coherent Bayesian analysis to estimate the posterior probability distribution of the physical parameters of the simulated signals using the parameter estimation code `LALInference` (Veitch et al., 2015). We obtain results by analyzing three instances of the synthetic event: (i) real data including the glitch, (ii) real data where the glitch has been subtracted, and (iii) simulated data with a zero-noise realization.[3] In all cases, the PSD used to compute the likelihood in Eq. (3.2) is fit to the data surrounding and including the event and glitch time Littenberg & Cornish (2015) to ensure an even comparison between different runs. Of particular astrophysical interest are the physical aspects of the binary measurable through the gravitational-wave signal: its component masses (m_1, m_2) via total mass and mass ratio, mass-weighted spins ($\chi_{\rm eff}$), and tidal deformabilities (Λ_1, Λ_2). In order to check the efficacy of recovery for either, we used

[2]When our study was started, no readily available waveform family which allows for both spin-precessional and finite-size tidal effects existed, though such a model has since become available (Dietrich et al., 2019).
[3]A zero-noise realization run assumes that the noise is exactly zero at all frequencies, while the PSD stays finite. This is a tool often used in the gravitational-wave literature, for example in Littenberg et al. (2013), Rodriguez et al. (2014), and Vitale & Chen (2018), to assess parameter estimation in an controlled environment. Statistically, results obtained with a zero-noise realization are equivalent to the average results that would be obtained with a large sample of runs on Gaussian noise (Nissanke et al., 2010; Vallisneri, 2011).

the IMRPhenomPv2 family to synthesize and insert three examples of a precessing signal, and the TaylorF2 to insert three tidally influenced, but spin-aligned, waveforms into the data. In Figure 3.6 we present a selection of two-dimensional posteriors over combinations of the parameters for a precessing signal simulated with IMRPhenomPv2 (top row) and three signals simulated with TaylorF2 (second to fourth row). In all cases, we use the same waveform family to simulate the signal added into the data and as template in the parameter estimation algorithm.

In all four events shown in Figure 3.6, we verify the recovery of the detector-frame mass parameters, since they dominate the phase evolution of the waveform. The left column of Figure 3.6 displays the total mass – chirp mass posterior for all four simulated signals, with the zero-noise-realization and glitch-removed cases shown. The glitch-present recovery is often badly biased, enough so that we do not include it in Figure 3.6 and instead refer to Table 3.1 to indicate their credible regions. The posteriors for the glitch removed and zero-noise cases are qualitatively very similar. From Figure 3.6 it is seen that the mass recovery is consistent with the injected value in all cases, and the zero-noise and glitch-removed recovery encompasses similar values. This validates the premise that the glitch removal method does not bias the lower PN order parameters which influence the waveform.

The second column of Figure 3.6 shows the two-dimensional posteriors for the mass ratio and the effective spin. We again find no bias in the parameter estimates due to the glitch removal. The posteriors for the glitch removal and the zero-noise analyses are minimally shifted with respect to each other, which is consistent with the expected effect of noise realization on signal recovery and not evidence for a bias. Indeed, the specific

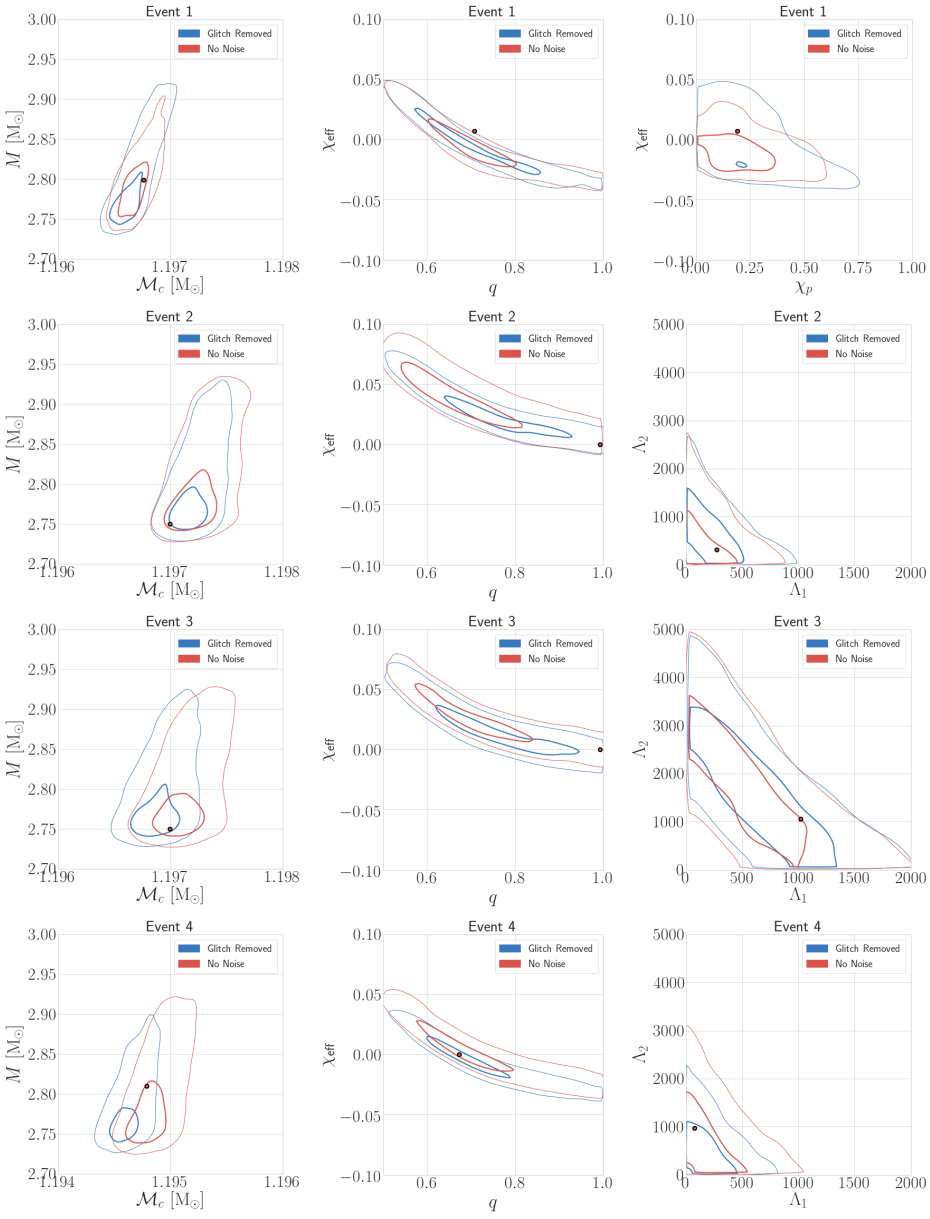

Figure 3.6. Posterior densities for the masses, spins, and tidal deformabilities for four overflow glitches (top to bottom). The left column shows the posteriors in total mass and chirp mass (in the detector frame); the middle column shows mass ratio versus $\chi_{\rm eff}$; the last column shows $\chi_{\rm eff}$ versus $\chi_{\rm p}$ (first event, top row) or component tidal parameter posteriors Λ_1 and Λ_2 (remaining three events). Thick (thin) lines show the 50% (90%) credible regions. The true values of the parameters are represented by the black edged marker. In all cases the parameter estimates after removing the overflow glitch are consistent with estimates from injections in zero noise.

noise realization of the data induces an additional shift on the posterior estimates of the order of the posterior variance. In addition, the top-right panel shows the posterior for the effective spin $\chi_{\rm eff}$ and the spin parameter $\chi_{\rm p}$ (Schmidt et al., 2015). The latter parameter is an estimate of spin-precession in the waveform. As expected we again see no biases due to glitch removal.

Finally, the tidal parameter estimation also seems unaffected by the glitch removal procedure. The two dimensional marginalized posteriors for the component tidal parameters are presented in the right column, second through fourth row of Figure 3.6. The posteriors obtained with our two analyses are both consistent with each other and capture the known value well within their credible intervals. Moreover, the recovered posterior structure is very similar to the actual posterior measured for GW170817 in Abbott et al. (2017b), exhibiting similar boundaries and degeneracies.

Credible intervals for the parameters, as well as their injected values, are quoted in Table 3.1 for all three analyses (with glitch mitigation, without glitch mitigation, and with a zero-noise realization). The 90% credible intervals computed from the glitch-mitigated data are consistent with the ones from the zero-noise analysis. This is in stark contrast to the parameter estimates computed if the glitch in included in the data analyzed. The values recovered are well outside of the posterior in the glitch-free examples, and nowhere near the known values. In all four cases, the mass ratio is pushed to extremely high values. The same extreme displacement occurs for the tidal parameters, producing tidal deformability values in the thousands, strongly peaked for Λ_1 and nearly unmeasurable for Λ_2. The uncertainties from the posteriors are wider than their glitch-free counterparts. Despite this, the credible intervals miss the known value by a wide margin, several

times their own width. This implies that without mitigation, not only is the most basic parameter estimation biased, but simply incorrect.

3.4. Conclusions

The focus of this work is to examine potential biases induced by various noise transient subtraction methods. There is a trade off between speed and fidelity in terms of their efficacy. Simple but fast methods which ignore the morphology of the noise transient or the data spectra are likely to introduce noticeable and predictable biases in signal amplitude recovery. Also worth noting is that the bias and widening of uncertainty induced by these methods may be more severe for weaker (lower SNR) signals. Amelioration of these biases by introducing the same gating procedure to the template waveform remains impractical. In a low-latency environment where sky maps are required without waiting for a full pass of a glitch extraction method like `BayesWave`, the time-frequency data excision in Section 3.2.2 seems best suited and of appropriate latency. While parameter biases are reduced for more careful treatments of data excision, they are not a substitute for full glitch subtraction — particularly when high data fidelity is required to retrieve an accurate estimation of physical parameters. Indeed we find that the data produced after glitch-mitigation by `BayesWave` are consistent with our zero-noise study to within shifts that can be attributed to the presence of noise.

The consistent recovery of the spin and tidal parameters are important tests: the frequencies affected are not only in the most sensitive bandwidth of the GW interferometers, but also where subdominant effects on the phase of the waveform, such as those from spin and tidal deformabilities, become measurable. If the glitch removal procedure

damaged the structure or coherence of the signal, then it would be expected that those parameters would exhibit significant bias. Another study which examines the biases in physical parameter recovery for binary black hole signals where the merger time overlaps a glitch can be found in Powell (2018).

The overflow glitch studied here is, in some sense, a best case scenario for glitch subtraction with `BayesWave`, because the signal and glitch have sufficiently different morphology. In particular, while the signal and glitch overlap in time-frequency (T-F) space, they are fit by wavelets having very different quality factor Q (which governs the number of cycles in the wavelet)–high Q for the BNS and low Q for the glitch. Generally, when glitches and signals do not overlap in T-F-Q space, a straightforward application of `BayesWave` will provide clean residuals for the PE analysis. Fortunately, that was the scenario presented by GW170817. Higher mass GW signals, such as BBH mergers, use lower Q wavelets and would therefore be more difficult to separate from a similar glitch with the current analysis tools. To mitigate against such a scenario in the future, we are developing glitch subtraction algorithms which include information about the network coherence of the signal, and lack thereof for any glitches.

Since multi-messenger astronomy involving NSs in compact binaries is expected to be highly featured in the upcoming Advanced LIGO/Virgo/KAGRA observing runs (Abbott et al., 2020a), confidence in the measured properties of GW signals is paramount. In the presence of short-duration noise transients near a merger signal, gating and data subtraction procedures are acceptable stopgap measures to obtain data products needed for rapid identification of electromagnetic counterparts. However, to obtain unbiased

results without inflating uncertainties, we find that data-tailored glitch-removal techniques such as `BayesWave` are required.

CHAPTER 4

Kilonova Detectability with Wide-Field Instruments

In this chapter, I quantify the ability of 13 wide field-of-view instruments to detect kilonovae, leveraging a large grid of over 900 radiative transfer simulations with 54 viewing angles per simulation (Wollaeger et al., 2021). I consider both current and upcoming instruments, collectively spanning the full kilonova spectrum. The Roman Space Telescope has the highest redshift reach of any instrument in the study, observing kilonovae out to $z \sim 1$ within the first day post-merger. I demonstrate that BlackGEM, DECam, GOTO, the Vera C. Rubin Observatory's LSST, ULTRASAT, and VISTA can observe some kilonovae out to $z \sim 0.1$ ($\sim$475 Mpc), while DDOTI, MeerLICHT, PRIME, *Swift*/UVOT, and ZTF are confined to more nearby observations. Furthermore, this chapter provide a framework to infer kilonova ejecta properties following non-detections and explore variation in detectability with these ejecta parameters. An adapted version of this chapter has been submitted for publication (Chase et al., 2021).

4.1. Introduction

Neutron star mergers have long been invoked as a cosmic source of heavy elements, produced through rapid neutron capture (r-process) nucleosynthesis (Lattimer & Schramm, 1974; Lattimer et al., 1977; Symbalisty & Schramm, 1982; Eichler et al., 1989; Freiburghaus et al., 1999; Côté et al., 2018). Heavy lanthanides and actinides fuse in material gravitationally unbound during the coalescence of either BNS or NSBH binaries with near-equal

mass ratios (Metzger, 2019). The residual radioactive decay of these r-process elements spurs electromagnetic emission, called a kilonova (Li & Paczyński, 1998; Kulkarni, 2005; Metzger et al., 2010).

Kilonova emission spans UVOIR wavelengths, with lower wavelength "blue" emission fading within a day of merger, giving way to "red" emission persisting for over a week. Observations of a kilonova's rapid evolution can reveal the role of neutron star mergers in Galactic r-process enrichment, while holding promise for additional discoveries in cosmology, nuclear physics, and stellar astrophysics.

Gamma-ray burst emission may also accompany a neutron star merger (Blinnikov et al., 1984; Paczynski, 1986; Eichler et al., 1989; Narayan et al., 1992), with later theories (Popham et al., 1999; Fryer et al., 1999) linking neutron star mergers to sGRBs: transient signals with hard gamma-ray emission persisting for less than two seconds (Norris et al., 1984; Kouveliotou et al., 1993). Numerous follow-up observations of sGRBs reveal viable kilonova candidates (Perley et al., 2009; Tanvir et al., 2013; Berger et al., 2013; Yang et al., 2015; Jin et al., 2016; Troja et al., 2018; Gompertz et al., 2018; Ascenzi et al., 2019; Lamb et al., 2019; Troja et al., 2019a; Jin et al., 2020; Rossi et al., 2020; Fong et al., 2021; Rastinejad et al., 2021; O'Connor et al., 2021), strengthening the theorized connection between sGRBs, kilonovae, and neutron star mergers. Astronomers solidified this connection with the joint detection of GW event GW170817 (Abbott et al., 2017b), GRB 170817A (Abbott et al., 2017c; Goldstein et al., 2017; Savchenko et al., 2017), and kilonova AT 2017gfo (Andreoni et al., 2017; Arcavi et al., 2017; Chornock et al., 2017; Coulter et al., 2017; Covino et al., 2017; Cowperthwaite et al., 2017; Drout et al., 2017; Evans et al., 2017; Kasliwal et al., 2017; Lipunov et al., 2017; Nicholl et al., 2017; Pian

et al., 2017; Shappee et al., 2017; Smartt et al., 2017; Tanvir et al., 2017; Troja et al., 2017; Utsumi et al., 2017; Valenti et al., 2017). GW170817 also serves as the first GW detection containing a neutron star (Abbott et al., 2017b) and the first multi-messenger detection with GWs (Abbott et al., 2017a).

Several serendipitous circumstances allowed for detection of the kilonova associated to GW170817. The source's comparatively tight sky localization (31 $\deg^2$ at 90% credible level; LVC, 2017; Abbott et al., 2020a) combined with its nearby distance estimate (40^{+8}_{-8} Mpc; LVC, 2017) promoted prompt detection of an UVOIR counterpart within 12 hours post-merger (Arcavi et al., 2017; Coulter et al., 2017; Cowperthwaite et al., 2017; Lipunov et al., 2017; Tanvir et al., 2017; Valenti et al., 2017). Due to its nearby distance, GW170817 was confined to a localization volume of ~ 520 Mpc^3 at the 90% credible level (LVC, 2017), leaving only a few dozen plausible host galaxies, which were efficiently observed with galaxy-targeted observations. Additionally, GW170817's favorable viewing angle ($\lesssim 20^\circ$; Ghirlanda et al., 2019; Troja et al., 2019b) aided coincident detection of a sGRB without excessive afterglow contamination of the kilonova signal.

However, detecting a kilonova at further distances becomes increasingly difficult, often requiring the use of wide FoV instruments. For example, large sky localization, exacerbated by the lack of coincident sGRB detection, spurred fruitless counterpart searches (Hosseinzadeh et al., 2019; Paterson et al., 2020) following the GW detection of GW190425 (Abbott et al., 2020b; LVC, 2019). This BNS merger's sky localization was constrained to a massive 10,183 $\deg^2$ at the 90% credible level (LVC, 2019), requiring an area of the sky over 300 times the size of GW170817's localization to be rapidly searched for transient signals. Additionally, the source was more distant than GW170817 (155^{+45}_{-45} Mpc; LVC,

2019) and confined to a larger localization volume (9.7×10^6 Mpc^3; LVC, 2019), making efficient galaxy-targeted kilonova searches unfeasible.

As GW detector sensitivity increases, wide-field instruments will remain necessary tools for kilonova detection. The advent of more sensitive GW detectors will lead to compact binary merger detection at farther distances, which jointly increases the sky volume required for counterpart searches in addition to reducing the effectiveness of galaxy-targeted searches. In the third Observing Run (O3) of advanced LIGO (Aasi et al., 2015) and advanced Virgo (Acernese et al., 2015), the average redshift horizon of a $1.4M_\odot$ + $1.4M_\odot$ BNS was 300 Mpc, 240 Mpc, and 100 Mpc for the LIGO Livingston, LIGO Hanford, and Virgo detectors, respectively.[1] We note that mergers comprised of more massive objects (e.g., NSBHs) are detectable at even farther distances.

The fourth Observing Run (O4) will considerably increase the sensitivity, with BNS horizon redshifts anticipated to increase to 360–430 Mpc, 200–270 Mpc, and 70–290 Mpc for advanced LIGO, advanced Virgo, and KAGRA (Akutsu et al., 2019), respectively (Abbott et al., 2020a). Furthermore, in the 2030s, proposed third-generation GW detectors including Einstein Telescope (Punturo et al., 2010) and Cosmic Explorer (Abbott et al., 2017g) will detect BNS mergers out to cosmological redshifts of $z \sim 4$ and $z \sim 10$, respectively (Hall & Evans, 2019), far beyond the reaches of currently existing instruments.

Although sky localization is expected to significantly improve with larger networks of GW detectors (Schutz, 2011; Nissanke et al., 2013b; Abbott et al., 2020a), localization estimates will still encompass significant areas of the sky. In O4, the four-detector network of advanced LIGO, advanced Virgo, and KAGRA will observe BNS (NSBH) systems

[1]Horizon redshifts computed by multiplying the BNS detectability ranges in Abbott et al. 2021 by the standard factor of 2.26 described in Finn & Chernoff 1993 and Chen et al. 2021.

with a median sky localization area of 33 deg^2 (50 deg^2) and volume of 52,000 Mpc^3 (430,000 Mpc^3), encapsulating thousands of plausible host galaxies (Abbott et al., 2020a). Moreover, the addition of a fifth GW detector in India will improve sky localization areas by approximately a factor of two (see Chapter 2). However, even in the era of third-generation GW detectors, sky localization areas will remain large for distant BNS mergers with more than 50% of BNS mergers at $z \gtrsim 0.4$ constrained to localization areas in excess of 100 deg^2 with a network of three Cosmic Explorer instruments (Mills et al., 2018). Therefore, wide-field instruments will remain a necessary tool for kilonova detection into the 2030s.

In this paper, we assess kilonova detectability with 13 wide-field instruments, quantifying the redshift out to which kilonovae are detectable for a variety of filters. This study builds upon previous detectability studies (Scolnic et al., 2018) by employing the Los Alamos National Laboratory (LANL) grid of radiative transfer kilonova simulations (Wollaeger et al., 2021) to explore detectability for a diverse range of kilonova ejecta masses, velocities, morphologies, compositions, and inclinations.

We describe the set of wide-field instruments selected for the study in Section 4.2 and then quantify the typical redshift reach of each instrument in Section 4.3. In Section 4.4, we explore how each instrument's ability to observe a kilonova varies with ejecta properties. We build upon these results in Section 4.5 to provide a framework for inferring kilonova properties from non-detections. We summarize each instrument's capacity for kilonova detection in Section 4.6 and offer suggestions for future kilonova searches in Section 4.7. Throughout the study, we adopt a standard Λ-CDM cosmology with parameters

$H_0 = 67.4$, $\Omega_M = 0.315$, and $\Omega_\Lambda = 0.685$ (Planck Collaboration et al., 2020). Data products and software produced through this study are available on GitHub.[2]

4.2. Wide-Field Instruments

The optimal observing strategy for multi-wavelength follow-up of LIGO/Virgo/KAGRA candidate events is an evolving science (e.g., Kasliwal & Nissanke, 2014; Gehrels et al., 2016; Artale et al., 2020), and varies greatly depending on the instrument FoV, wavelength range, and sensitivity (see, e.g., Gehrels et al., 2015; Bartos et al., 2016; Cowperthwaite et al., 2019; Graham et al., 2019). Wide-field instruments provide the ability for rapid searches of GW sky localization regions with high cadence. In the next decade, a number of ground- and space-based facilities will be dedicated to these types of follow-up, enabling the ability to cover large sky regions in a short amount of time. We base our kilonova detectability study on a selection of current and future wide-field instruments with planned follow-up of LIGO/Virgo/KAGRA candidate events. In addition, we include instruments that have the sensitivity and wavelength coverage to contribute significantly to the kilonova detection rate, but that lack a formal GW follow-up strategy (i.e., LSST, Roman; Cowperthwaite et al., 2019; Foley et al., 2019).

We note that this study is focused on the ability of wide-field instruments to detect kilonovae arising from poorly-localized mergers. We primarily focus on kilonova searches following a LIGO/Virgo/KAGRA candidate BNS or NSBH event. However, the results of this study apply to kilonova searches following sGRB detections with large sky localization areas, such as some sGRBs detected with the *Fermi Gamma-Ray Burst Monitor* (Goldstein et al., 2020). The follow-up strategy for well-localized events is significantly

[2] `https://github.com/eachase/kilonova_detectability/`

different (as it does not require covering large sky areas), and is beyond the scope of this work.

All instruments in this study are either already active or plan to see first light within the 2020s, in the advanced ground-based GW detector era. Our study includes several existing instruments such as the Deca-Degree Optical Transient Imager (DDOTI; Watson et al., 2016), the Dark Energy Camera (DECam; Flaugher et al., 2015), the Gravitational-wave Optical Transient Observer (GOTO; Dyer et al., 2018, 2020), MeerLICHT (Bloemen et al., 2015), *Swift*'s Ultra-Violet Optical Telescope (UVOT; Roming et al., 2005), the Visible and Infrared Survey Telescope for Astronomy (VISTA; Sutherland et al., 2015), and the Zwicky Transient Facility (ZTF; Bellm et al., 2019). In addition, we include numerous near-term instruments such as BlackGEM (Bloemen et al., 2015), the Vera C. Rubin Observatory's Legacy Survey of Space and Time (LSST; Ivezić et al., 2019), the PRime-focus Infrared Mirolensing Experiment (PRIME[3]), the Nancy Grace Roman Space Telescope (Roman; Spergel et al., 2015), the Ultraviolet Transient Astronomy Satellite (ULTRASAT; Sagiv et al., 2014), and the Wide-Field Infrared Transient Explorer (WINTER; Lourie et al., 2020). This study is not a comprehensive selection of all wide-field instruments available in the coming decade.

The selected wide-field instruments span UVOIR wavelengths (∼2,000-22,000 Å) typical of kilonova emission. The 5σ limiting magnitudes were compiled from the literature based either on the instrument design sensitivity (i.e., BlackGEM, LSST, PRIME, Roman, ULTRASAT, WINTER) or the instrument performance during previous LIGO/Virgo observing runs (i.e., DECam, DDOTI, GOTO, MeerLICHT, UVOT, VISTA, ZTF). For

[3]`http://www-ir.ess.sci.osaka-u.ac.jp/prime/index.html`

instruments that have already demonstrated their capability to effectively cover GW localization regions, we focus our study on the filters used in those searches. The filter selection[4] and limiting magnitudes are outlined here for each instrument (see also Table 4.1):

[4]When available, filter response functions were taken from the SVO Filter Profile Service (Rodrigo & Solano, 2020). The filter response functions for BlackGEM, DDOTI, GOTO, PRIME, and WINTER were obtained through private communication with the instrument teams.

Instrument	FoV (deg^2)	Exp. Time (s)	Filter	$\lambda_{\rm eff}$ (Å)	$m_{\rm lim}$ (AB)	$z_{50\%}$	$z_{95\%}$	$z_{5\%}$	Ref.
BlackGEM	8.1	300	u	3800	21.5	0.037	0.013	0.091	1
			g	4850	22.6	0.057	0.011	0.21	
			q	5800	23.0	0.072	0.027	0.23	
			r	6250	22.3	0.052	0.022	0.14	
			i	7650	21.8	0.044	0.013	0.13	
			z	9150	20.7	0.025	0.011	0.069	
DDOTI	69	7200	w	6190	20.5[a]	0.023	0.0083	0.073	2,3
DECam	2.2	90	i	7870	22.5	0.058	0.022	0.18	4
			z	9220	21.8	0.042	0.014	0.12	
GOTO	40[b]	360	L	5730	21.0	0.029	0.0097	0.097	5,6
LSST	9.6	30	u	3690	23.6	0.078	0.012	0.28	7
			g	4830	24.7	0.14	0.035	0.48	
			r	6220	24.2	0.12	0.043	0.43	
			i	7570	23.8	0.099	0.038	0.31	
			z	8700	23.2	0.079	0.029	0.24	
			y	9700	22.3	0.052	0.021	0.14	
MeerLICHT	2.7	60	u	3800	19.1	0.013	0.0052	0.035	1,8
			g	4850	20.2	0.019	0.0032	0.073	
			q	5800	20.6	0.024	0.010	0.074	
			r	6250	19.9	0.019	0.0067	0.046	
			i	7650	19.4	0.016	0.0053	0.047	
			z	9150	18.3	0.0085	0.0023	0.024	

PRIME	1.56	100	Z	9030	20.5	0.023	0.0099	0.067	9
			Y	10200	20.0	0.019	0.0079	0.048	
			J	12400	19.6	0.017	0.0067	0.044	
			H	16300	18.4	0.0088	0.0023	0.023	
Roman	0.28	67	R	6160	26.2	0.29	0.10	0.96	10,11
			Z	8720	25.7	0.24	0.10	0.79	
			Y	10600	25.6	0.23	0.10	0.79	
			J	12900	25.5	0.22	0.10	0.65	
			H	15800	25.4	0.22	0.095	0.48	
			F	18400	24.9	0.17	0.037	0.38	
Swift/UVOT	0.08	80	u	3500	19.9	0.015	0.0019	0.061	12
ULTRASAT	200	900	NUV	2550	22.3	0.022	0.0022	0.10	13[c]
VISTA	1.6	360	Y	10200	21.5	0.038	0.012	0.094	14,15
			J	12600	21.0	0.032	0.011	0.071	
			H	16500	21.0	0.031	0.011	0.068	
			K_s	21400	20.0	0.018	0.007	0.045	
WINTER	1.0	360	Y	10200	21.5	0.038	0.012	0.093	16
			J	12500	21.3	0.036	0.012	0.075	
			H_s	15800	20.5	0.023	0.010	0.052	

ZTF	47	30	g	4770	20.8	0.025	0.0063	0.092	17
			r	6420	20.6	0.024	0.0092	0.074	
			i	8320	19.9	0.019	0.0061	0.059	

Table 4.1. The column labeled $z_{50\%}$ represents the maximum redshift at which 50% of LANL kilonova models are observable at any one time in a given band. Columns labeled $z_{95\%}$ and $z_{5\%}$ enumerate similar redshifts for 95% and 5% of modeled kilonovae, respectively.
[a]10σ limiting magnitude.
[b]FoV of one GOTO-8 system.
[c]ULTRASAT filter modeled with a top-hat function between 2200 and 2800 Å. Limiting magnitudes were taken from the instrument website (see footnote 6)
References: (1) Paul Groot, 2021, Private Communication; (2) Thakur et al. (2020); (3) Becerra et al., in prep.; (4) Soares-Santos et al. (2016); (5) Ben Gompertz & Martin Dyer, 2021, Private Communication; (6) Dyer (2020); (7) Ivezić et al. (2019); (8) de Wet et al. (2021); (9) Takahiro Sumi, 2021, Private Communication; (10) Scolnic et al. (2018); (11) Hounsell et al. (2018); (12) Oates et al., in prep.; (13) Sagiv et al. (2014); (14) McMahon et al. (2013); (15) Banerji et al. (2015); (16) Nathan Lourie & Danielle Frostig, 2021, Private Communication; (17) Bellm et al. (2019)

BlackGEM – BlackGEM is a planned array of wide-field optical telescopes located at the La Silla Observatory in Chile. It will initially consist of three 0.65-m optical telescopes, each with a 2.7 deg^2 FoV (Bloemen et al., 2015; Groot, 2019). Each telescope is equipped with a six-slot (*ugriz* and broad q) filter wheel. The main focus of the BlackGEM mission is the follow-up of LIGO/Virgo/KAGRA candidate events, with a goal of achieving a cadence of two hours on low-latency sky localization using the u, q, and i filters. In order to determine the most sensitive filters for KN detection, we also include g, r, and z in our study. The 5σ limiting magnitude for a 300 s integration time under photometric observing conditions (1 seeing) is $q \gtrsim 23$ mag (Paul Groot, 2021, Private Communication).

DDOTI – DDOTI is a wide-field, robotic imager located at the Observatorio Astronómico Nacional (OAN) in Sierra San Pedro Mártir, Mexico (Watson et al., 2016). The instrument is comprised of six 28-cm telescopes with a combined 69 deg^2 FoV. DDOTI produces unfiltered images, referred to as the w-band. It has previously been using in the follow-up of GW190814 (Thakur et al., 2020). Based on DDOTI follow-up during O3 (Becerra et al., in prep.), we adopt a median exposure time of $\sim$2 hr, yielding a median 10σ limiting magnitude $w \gtrsim 20.5$ mag.

DECam – DECam is mounted on the 4-m Victor M. Blanco telescope at the Cerro Tololo Inter-American Observatory (CTIO) in Chile. The instrument has a 2.2 deg^2 FoV, and was designed for the purpose of wide-field optical (*ugrizY*) surveys (Flaugher et al., 2015). Electromagnetic follow-up of LIGO/Virgo candidate events has been carried out in previous observing runs by the Dark Energy Survey GW (DESGW) Collaboration (e.g., Soares-Santos et al., 2016, 2017; Andreoni et al., 2020; Herner et al., 2020; Morgan et al.,

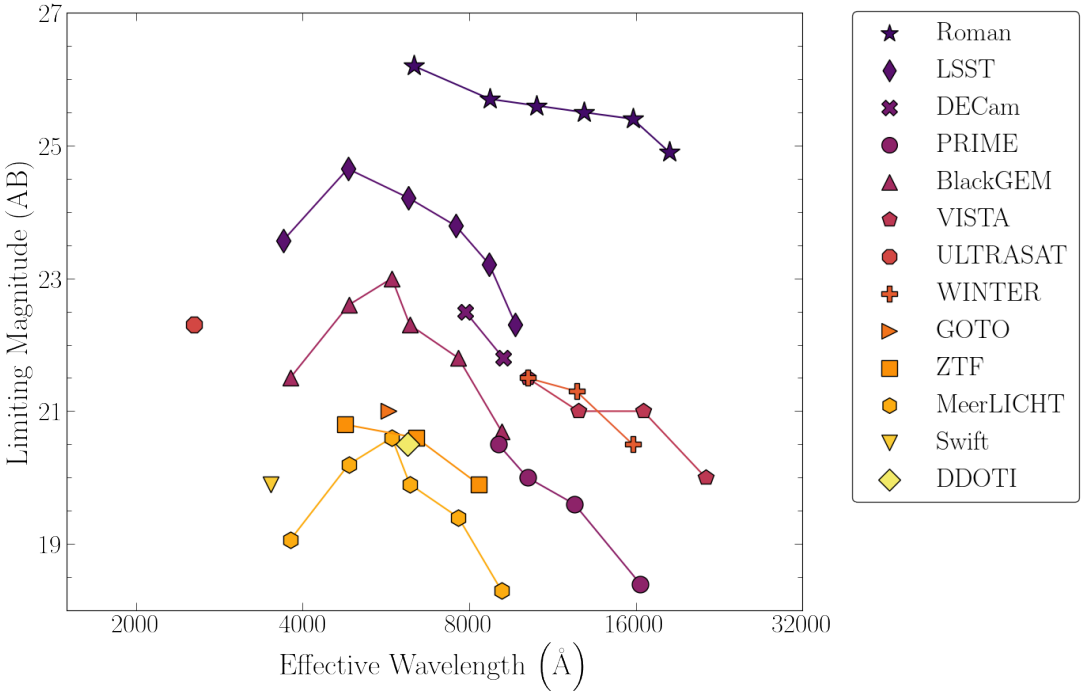

Figure 4.1. Limiting magnitudes for a selection of wide-field instruments. Each symbol corresponds to one instrument, with an instrument's filters represented by its bandpass filter function's effective wavelength. Lines connect filters from the same instrument. All limiting magnitudes are presented at the 5σ confidence level, unless otherwise indicated in Table 4.1.

2020) using the i- and z-bands. In this work, we focus on kilonova detection by DECam at these wavelengths.

GOTO – At design specifications, GOTO will include an array of 16× 40-cm telescopes on two robotic mounts (producing a 160 deg^2 FoV) at two separate locations in Spain and Australia, allowing for coverage of both hemispheres (Dyer et al., 2018, 2020; Dyer, 2020). A prototype, referred to as GOTO-4 (18 deg^2 FoV), was instituted in La Palma, Spain in 2017 with an initial array of 4 telescopes. This was upgraded to an 8 telescope array in 2020 (GOTO-8), yielding a 40 deg^2 FoV (Dyer et al., 2020). The prototype mission, GOTO-4 has demonstrated its capability to cover large GW localization

regions during O3 with good sensitivity to optical transients (Gompertz et al., 2020). In a 360 s integration time, GOTO can reach depths of $L \gtrsim 21.0$ mag (Ben Gompertz & Martin Dyer, 2021, Private Communication), where L is a wide-band filter[5], approximately equivalent to $g + r$.

LSST − The Vera C. Rubin Observatory, currently under construction on Cerro Pachon in Chile, has a planned first light in 2023. The observatory consists of an 8.4-m wide-field, optical telescope covering a 9.6 deg^2 FoV. The Rubin Observatory's LSST will survey half the sky every three nights in the *ugrizy* filters. The planned Wide-Fast-Deep (WFD) survey will reach $r \gtrsim 24.2$ mag (assuming airmass $\sim$1.2) for a 30 s integration time (Ivezić et al., 2019). Despite the lack of a formal GW follow-up strategy, we have included LSST within this study to highlight the sensitivity of the WFD survey (see also, e.g., Scolnic et al., 2018; Cowperthwaite et al., 2019) in order to encourage GW follow-up, and demonstrate the prospect of serendipitous detection.

MeerLICHT − MeerLICHT is a fully robotic 0.65-m optical telescope located at the South African Astronomical Observatory (SAAO) in Sutherland, South Africa (Bloemen et al., 2015). MeerLICHT was designed as the prototype instrument for the BlackGEM array (Groot, 2019). The telescope has a 2.7 deg^2 FoV, and covers the same $ugr(q)iz$ wavelengths as BlackGEM. MeerLICHT has been used for GW follow-up during past LIGO/Virgo observing runs (e.g., GW190814; de Wet et al., 2021) with observations in the u, q, and i filters. For comparison to BlackGEM, we likewise include the g, r, and z filters in our study. MeerLICHT is sky background limited in 60 s exposures, yielding a limiting magnitude $q \gtrsim 20.6$ mag.

[5] `https://github.com/GOTO-OBS/public_resources/tree/main/throughput`

PRIME − PRIME is a 1.8-m wide-field infrared telescope under construction at SAAO. The telescope has a 1.56 deg^2 FoV, and covers wavelengths $ZYJH$. In a 100 s integration time PRIME reaches depths of $z \gtrsim 20.5$ mag and $Y \gtrsim 20.0$ mag (Takahiro Sumi, 2021, Private Communication).

Roman − The 2.4-m Roman Space Telescope (formerly WFIRST), with planned launch in 2025, will cover a 0.28 deg^2 FoV ($\sim$200 times larger than *HST*; Spergel et al., 2015). The Wide Field Instrument (WFI) is sensitive to optical/infrared wavelengths between 5000–20000 Å. In this study, we focus on the $RZYJHF$ filters. We have chosen to include Roman within this study in order to encourage GW follow-up (see also Foley et al., 2019), and demonstrate its sensitivity to kilonovae out to cosmological distances. The instrument sensitivity is adopted following Hounsell et al. (2018) and Scolnic et al. (2018).

UVOT − The UVOT onboard the *Neil Gehrels Swift Observatory* has a wavelength coverage of 1600–8000 Å, and a 0.08 deg^2 FoV (Roming et al., 2005). Despite its smaller FoV, *Swift* is able to cover large regions of the sky in < 24 hr with a rapid response (a few hours) to LIGO/Virgo alerts (Evans et al., 2016, 2017; Klingler et al., 2019; Page et al., 2020; Klingler et al., 2021). In addition, *Swift* has the added benefit of simultaneous X-ray coverage from the X-ray Telescope (XRT). UVOT follow-up has been optimized for its smaller FoV by targeting galaxies with high probabilities of being the host, ensuring they are completely within the FoV (Klingler et al., 2019). The large majority of UVOT tiles are observed with the u-band, and, therefore, we focus our analysis on this filter. Based on GW follow-up during O3, we adopt a median 5σ limiting magnitude $u \gtrsim 19.9$ mag (Oates et al., in prep.).

ULTRASAT − ULTRASAT[6] is an ultraviolet telescope with planned launch to geostationary orbit in 2024. The instrument will have a 200 deg^2 FoV, and cover wavelengths between 2200–2800 Å, referred to as NUV. The estimated limiting magnitude in 900 s integration time is $NUV \gtrsim 22.3$ mag. Since ULTRASAT does not have a publicly available filter function, we approximated the filter response with a top-hat function between 2200 and 2800 Å.

VISTA − VISTA is a 4-m wide-field survey telescope equipped with the VISTA InfraRed CAMera (VIRCAM) covering wavelengths $ZYJHK_s$ with a 1.6 deg^2 FoV (Sutherland et al., 2015). VISTA is located at the Cerro Paranal Observatory in Chile, and operated by the European Southern Observatory (ESO). Follow-up of LIGO/Virgo candidate events has largely occurred through the Vista Near infra-Red Observations Uncovering Gravitational wave Events (VINROUGE) project in the Y, J, and K_s filters (e.g, Tanvir et al., 2017; Ackley et al., 2020). The 5σ limiting magnitudes were taken from the Vista Hemisphere Survey (McMahon et al., 2013; Banerji et al., 2015) and re-scaled to a 360 s exposure time, yielding $Y \gtrsim 21.5$ mag, $J \gtrsim 21.0$ mag, $H \gtrsim 21.0$ mag, and $K_s \gtrsim 20.0$ mag.

WINTER − WINTER is a new infrared instrument, with planned first light in mid-2021 (Lourie et al., 2020; Frostig et al., 2020). WINTER will use a 1-m robotic telescope located at the Palomar Observatory in California, United States. The instrument has a $\sim$1 deg^2 FoV, and covers infrared wavelengths YJH_s. In a 360 s integration time, WINTER reaches 5σ depth $Y \gtrsim 21.5$ mag, $J \gtrsim 21.3$ mag, and $H_s \gtrsim 20.5$ mag (Nathan Lourie & Danielle Frostig, 2021, Private Communication).

[6] `https://www.weizmann.ac.il/ultrasat/mission/mission-design-overview`

ZTF – ZTF employs a wide-field camera (47 deg^2 FoV) on the Palomar 48-in (P48) Oschin (Schmidt) telescope in San Diego County, California, United States (Bellm et al., 2019). Using 30 s exposures, it can cover 3760 deg^2 hr^{-1} to limiting magnitude $r \gtrsim$ 20.6 mag (Graham et al., 2019). This capability makes ZTF an effective tool for kilonova searches, both for GW candidate events (Coughlin et al., 2019; Kasliwal et al., 2020) and serendipitous discovery (Andreoni et al., 2021).

We note that the follow-up strategy and sensitivity of these instruments varies greatly depending on a number of factors, such as the observing conditions, sky location, and the size of the GW localization region. The sensitivity assumed in this work is considered to be an approximate limiting magnitude for GW follow-up, while noting that this sensitivity is variable day-to-day for each ground-based instrument. We also note that the limiting magnitudes are computed for "snapshot" exposures, and more sensitive images can be obtained by stacking multiple exposures over the course of a night. Figure 4.1 displays the assumed limiting magnitudes, indicating separate filters by their effective wavelength. For consistency, we compute effective wavelengths from all filter response functions using Eq. 1 of King (1952). These instruments provide an excellent coverage of the range of wavelengths expected for kilonovae. In Table 4.1, we present the FoV, typical exposure time of GW tiling, filter effective wavelengths, and limiting magnitudes for each instrument.

4.3. Assessing Kilonova Detectability

We employ the Los Alamos National Laboratory (LANL) grid of kilonova simulations (Wollaeger et al., 2021) to assess each instrument's ability to observe a kilonova.

Property	Values
Dyn. ejecta mass	$\{0.001, 0.003, 0.01, 0.03, 0.1\}\ M_\odot$
Wind ejecta mass	$\{0.001, 0.003, 0.01, 0.03, 0.1\}\ M_\odot$
Dyn. ejecta velocity	$\{0.05, 0.15, 0.3\}\ c$
Wind ejecta velocity	$\{0.05, 0.15, 0.3\}\ c$
Dyn. ejecta morphology	Toroidal (T; Korobkin et al. 2021)
Wind ejecta morphology	Spherical (S) or "Peanut" (P; Korobkin et al. 2021)
Dyn. ejecta composition	initial $Y_e = 0.04$ (see Wollaeger et al. 2021)
Wind ejecta composition	initial $Y_e = 0.27$ or 0.37 (see Wollaeger et al. 2021)

Table 4.2. Properties of LANL kilonova simulations (adapted from Wollaeger et al. 2021).

Rather than limiting our study to AT 2017gfo-like kilonovae, these radiative transfer simulations span a wide range of ejecta parameters, including expected values from both BNS and NSBH progenitors. The LANL simulations are two-component, multi-dimensional, axisymmetric kilonova models, generated with the Monte Carlo radiative transfer code `SuperNu` (Wollaeger et al., 2013; Wollaeger & van Rossum, 2014). These simulations rely on nucleosynthesis results from the `WinNet` code (Winteler et al., 2012; Korobkin et al., 2012) in addition to a set of tabulated binned opacities (Fontes et al., 2020) from the LANL suite of atomic physics codes (Fontes et al., 2015). The most recent LANL grid of kilonova simulations (Wollaeger et al., 2021) includes a full set of lanthanides and fourth row elements, some of which were not included in previous datasets (Wollaeger et al., 2018).

These radiative transfer simulations simultaneously evolve two ejecta components: a dynamical ejecta and wind ejecta component. The dynamical ejecta component is initiated with a low electron fraction ($Y_e = 0.04$), and corresponds to the lanthanide-rich or "red" emission. This component has composition consistent with the robust "strong"

r-process pattern such as the one repeatedly found in metal-poor r-process enriched stars and in the Solar r-process residuals (Sneden et al., 2009; Holmbeck et al., 2020). The second, lanthanide-poor wind ejecta component corresponds to the "blue" kilonova emission and is primarily composed of wind-driven ejecta from the post-merger accretion disk. The wind ejecta is initiated with two separate wind compositions, representing either high- ($Y_e = 0.37$) or mid- ($Y_e = 0.27$) latitude wind composition, consistent with winds induced by a wide range of post-merger remnants (Lippuner et al., 2017; Wollaeger et al., 2021). Dynamical ejecta is initiated with a toroidal morphology, constrained near the binary's orbital plane, while the wind ejecta is modeled by either a spherical or "peanut-shaped" geometry (Korobkin et al., 2021). Figure 4.2 presents the two morphological configurations used in the simulation set. Models span five ejecta masses (0.001, 0.003, 0.01, 0.03, and $0.1 M_{\odot}$) and three ejecta velocities (0.05, 0.15, and $0.3c$) for each component, covering the full range of kilonova properties anticipated from numerical simulations (see Wollaeger et al. 2021 and references therein). By considering all possible combinations of ejecta properties, the LANL grid includes 900 kilonova simulations. The full set of simulation parameters are compiled in Table 4.2.

These 900 simulations have previously been used to estimate kilonova properties associated with follow-up of GW190814 (Thakur et al., 2020) and targeted observations of two cosmological sGRBs (O'Connor et al., 2021; Bruni et al., 2021). Additionally, the LANL simulation grid is the basis for an active learning-based approach to a kilonova lightcurve surrogate modeling and parameter estimation framework (Ristic et al., 2021).

All 900 multi-dimensional simulation are rendered in 54 viewing angles, each subtending an equal solid angle of $4\pi/54$ sr. In this study, we use spectra from all 54 viewing angle

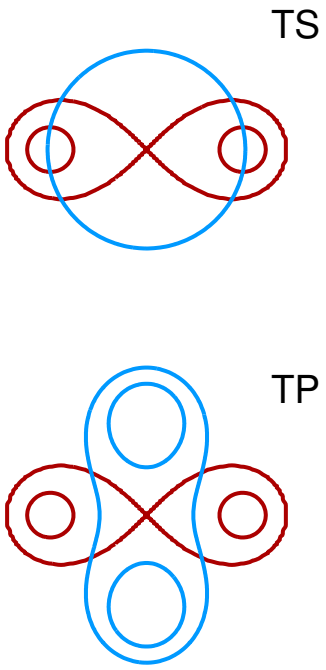

Figure 4.2. Schematics of the two combined morphologies used in the simulation grid (Wollaeger et al., 2021). All models have a toroidal (T, red) dynamical ejecta, 450 models are simulated with a spherical wind (S, blue), and 450 models are simulated with a peanut-shaped wind (P, blue). Each component is varied over the mass-velocity grid in Table 4.2, and hence is not necessarily drawn to scale here (adapted from Korobkin et al. 2021 and Wollaeger et al. 2021).

renditions to quantify detectability, making the generous assumption that a GW event has equal probability of detection with all viewing angles.[7] This differs from kilonova searches aimed at sGRBs, such as in O'Connor et al. 2021, where we limit our simulation grid to face-on viewing angles ($\theta_v \lesssim 15.64°$) as sGRBs are typically detected on-axis. By

[7]Gravitational waves from compact-binary coalescences are preferentially detected near face-on and face-off inclinations (Finn & Chernoff, 1993; Nissanke et al., 2010; Schutz, 2011), although a wide range of viewing angles are detectable at small distances (Abbott et al., 2019a, 2020c,d). We can further constrain kilonova detectability by including low-latency estimates on inclination.

including all 54 viewing angles of the 900 LANL kilonova simulations, our detectability study incorporates a full suite of 48,600 kilonova models.

Each model includes a set of time-dependent spectra, which are converted to lightcurves by computing a magnitude associated with each spectrum. Spectra are not simulated for the first three hours post-merger (rest frame). We render each simulated spectra set into a lightcurve for various redshifts, z, and for a broad range of filters with corresponding wavelength-dependent bandpass filter functions $R(\lambda_0)$. Magnitudes are computed according to

$$m_{\mathrm{AB}} = -2.41 - \frac{\int_0^\infty f\left(\lambda_0 (1+z)^{-1}\right) R(\lambda_0)\, \lambda_0 d\lambda_0}{(1+z)\int_0^\infty R(\lambda_0)\, \lambda_0^{-1} d\lambda_0}, \tag{4.1}$$

where λ_0 is the observed wavelength and $f(\lambda_0)$ is the wavelength-dependent spectral flux density (Hogg et al., 2002; Blanton et al., 2003). In Equation 4.1, we account for cosmological K-corrections (Humason et al., 1956; Oke & Sandage, 1968) by converting rest-frame spectral emission to observer-frame wavelengths.

We define a kilonova as detectable in a given filter if it outshines the limiting magnitude of the filter, as listed in Table 4.1. Then, we trace the detectability's variation with redshift, by considering lightcurves at various cosmological distances. Figure 4.3 displays detectability constraints for two representative filters: the LSST r-band (optical) and the Roman Space Telescope's H-band (near-infrared). We present detectability, defined as the fraction of detectable kilonova simulations, as a function of both redshift and observer-frame time. Detectability in the LSST/r-band decreases over time, as kilonovae optical emission fades within $\sim$1 day post-merger. However, the higher wavelength Roman/H-band reaches peak detectability two days post-merger, with 5% of nearby ($<$ 1 Gpc)

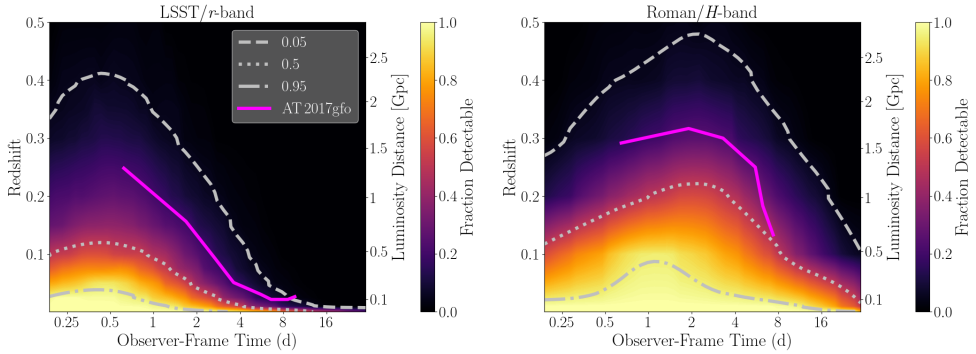

Figure 4.3. Detectability constraints for two filters: LSST/r-band (*left*) and Roman/H-band (*right*). Contours indicate the fraction of 48,600 simulated kilonovae (900 simulations each rendered at 54 viewing angles) with apparent magnitudes brighter than the limiting magnitude in each filter, for a given redshift and observer-frame time. The three white contours demarcate regions where 5%, 50%, and 95% of simulated kilonovae are detectable. The magenta curve represents each filter's ability to detect AT 2017gfo-like kilonovae.

kilonovae detectable over two weeks after merger. For comparison, Figure 4.3 includes detectability constraints for AT 2017gfo-like kilonovae, computed from spectroscopic data (Chornock et al., 2017; Cowperthwaite et al., 2017; Nicholl et al., 2017; Pian et al., 2017; Shappee et al., 2017; Smartt et al., 2017).[8] We do not present AT 2017gfo-like detectability within 12 hours of merger, as no spectra were collected at this point in the kilonova evolution.

Our AT 2017gfo-like detectability metrics are broadly consistent with previous studies (Scolnic et al., 2018; Rastinejad et al., 2021). Similar figures for all filters in Table 4.1 are available in Appendix A.

For each filter, we compute the maximum redshift at which 50% of simulated kilonovae are detectable at any one time, $z_{50\%}$, called the "typical redshift reach." With

[8]Compiled on `kilonova.space` (Guillochon et al., 2017)

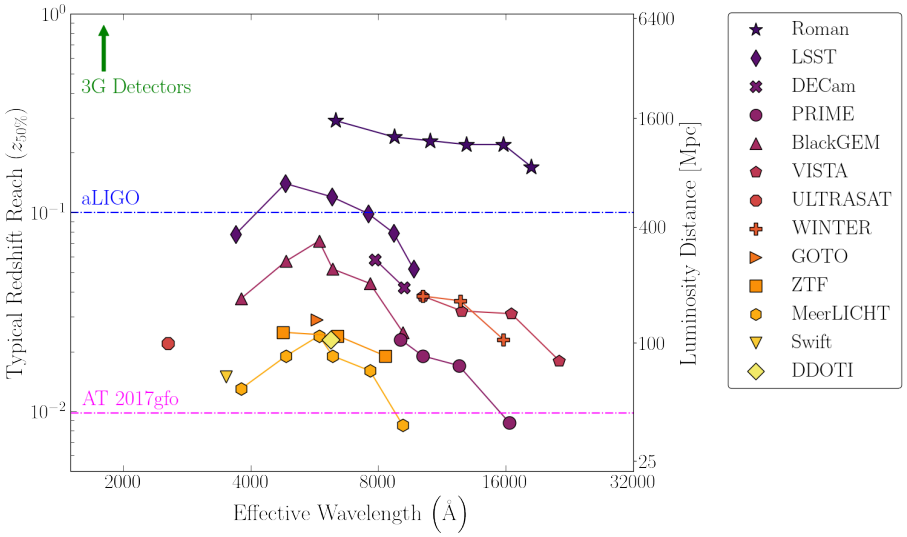

Figure 4.4. Typical redshift reach for a selection of instruments. The vertical axis indicates the maximum redshift at which 50% of the LANL simulated lightcurves are detectable in a given filter at any one time. Similarly to Figure 4.4, each symbol corresponds to one instrument, with an instrument's filter represented by their bandpass filter function's effective wavelength. Lines connect filters from the same instrument. The magenta horizontal line indicates the redshift of AT 2017gfo's host galaxy (Kourkchi & Tully, 2017), while the blue line indicates the redshift horizon for a $1.4M_{\odot}$ + $1.4M_{\odot}$ BNS at advanced LIGO's design sensitivity (Hall & Evans, 2019). Horizon redshifts for third-generation GW detectors, including Cosmic Explorer and Einstein Telescope, exceed the maximum redshift in the figure.

this definition, we ascribe a typical redshift reach of $z_{50\%} = 0.12$ and $z_{50\%} = 0.22$ to the LSST/r-band and Roman/H-band in Figure 4.3, respectively. Table 4.1 lists the typical redshift reaches for all instruments and filters, in addition to compiling maximum detectable redshifts for both 95% and 5% of simulated kilonovae as $z_{95\%}$ and $z_{5\%}$, respectively.

Additionally, Figure 4.4 compares the typical redshift reach for all instruments in this study, highlighting the differences as a function of their effective wavelengths (see

Table 4.1). Typical redshift reaches vary from $z_{50\%} = 0.0085$ ($\sim$38 Mpc) for the MeerLICHT/z-band up to $z_{50\%} = 0.29$ ($\sim$1.5 Gpc) for the Roman/R-band. As anticipated, the typical redshift reach for each instrument correlates significantly with the limiting magnitude distribution in Figure 4.1. We remind the reader that simulated lightcurves are not available earlier than three hours post-merger (rest frame), resulting in no detectability predictions in this time range. This omission may bias the detectability estimates of low-wavelength (ultraviolet) filters, such as the ULTRASAT/NUV-band, LSST/u-band, and UVOT/u-band.

4.4. Detectability Variations with Kilonova Properties

The typical redshift reach often varies significantly with kilonova properties, such as the ejecta mass or velocity. Larger ejecta masses generally result in more luminous kilonova emission, allowing for detection at higher redshifts, while kilonovae containing lower ejecta masses are only detectable at nearby distances. This mass dependency makes it difficult to determine whether a GW candidate event will produce an observable kilonova for a given instrument. Robust detectability metrics are further muddled by compounding degeneracies with other parameters such as velocity of the expanding ejecta, viewing angle, and composition.

Differing kilonova properties induce variations in kilonova detectability. For example, a kilonova with large wind ejecta mass and small dynamical ejecta mass may be easily detectable in the ultraviolet but difficult to observe in near-infrared filters, while other kilonova parameters may produce emission that is primarily detectable in the infrared. Lower-wavelength filters probe the wind ejecta, with peak emission in optical wavelengths

at early times. At the low-wavelength extreme, ultraviolet instruments capture the early structure of the outermost wind-driven ejecta (Arcavi, 2018; Banerjee et al., 2020). However, these low-wavelength filters offer little insight into the dynamical ejecta, which peaks at redder wavelengths. Additionally, a filter's variation with kilonova parameters depends on the source redshift: high-redshift kilonova emission is shifted to higher wavelengths, requiring subsequently redder filters to capture variability in dynamical ejecta mass. If kilonovae properties are unknown, multi-band observations across UVOIR wavelengths are necessary to maximize the probability of kilonova detection.

Figure 4.5 demonstrates the variation in kilonova detectability in the Roman/H-band for different ejecta masses. The left (right) column restricts the simulation set to one dynamical (wind) ejecta mass, while allowing all other parameters to vary, resulting in 9720 simulations per panel (180 simulations each with 54 viewing angles). In the left column, dynamical ejecta mass varies from the lowest ($0.001M_{\odot}$) to the largest ($0.1M_{\odot}$) values in the LANL simulation grid. Larger ejecta masses enhance detectability, as 50% of simulations with dynamical ejecta masses of $0.1M_{\odot}$ are detectable out to $z = 0.31$, with peak emission three days post-merger. Lower ejecta masses induce both dimmer emission and an earlier peak timescale (e.g., Kasen et al., 2017), as shown by the diminished late-time detectability and smaller typical redshift reach ($z = 0.16$) for dynamical ejecta masses of $0.001M_{\odot}$. However, a small subset of kilonovae with low dynamical ejecta masses remain detectable at redshifts $z > 0.3$, consistent with the addition of a large wind ejecta mass. The variation is a bit more pronounced for wind ejecta: 50% of simulated kilonovae with large wind ejecta masses ($0.1M_{\odot}$) are detectable out to $z = 0.37$, while less than 5% of low wind ejecta ($0.001M_{\odot}$) kilonovae are detectable at such high redshifts.

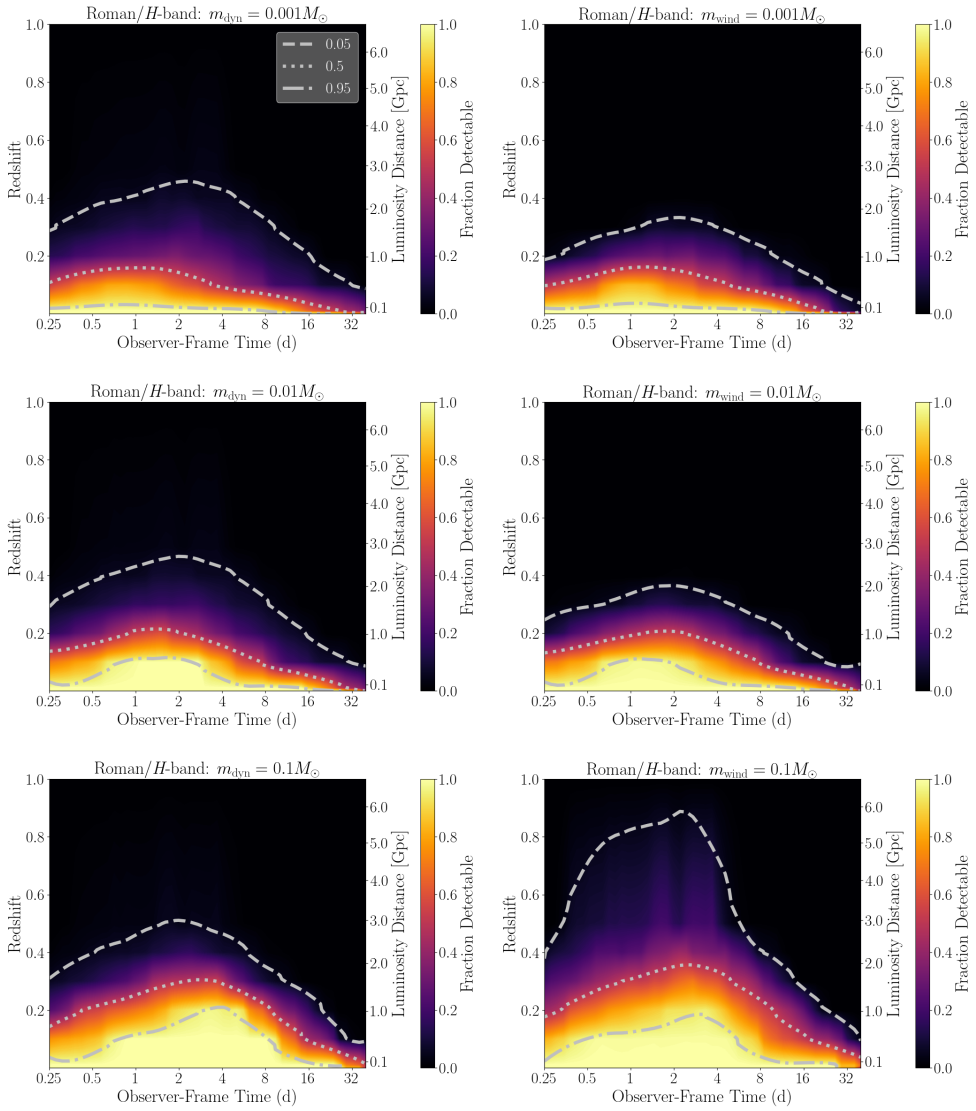

Figure 4.5. Detectability constraints for the Roman/H-band for six sets of kilonova simulations. The left column represents variation with dynamical ejecta mass, while the right presents variation with wind ejecta mass. The top row corresponds to lower masses ($0.001 M_\odot$), middle row corresponds to an intermediate mass ($0.01 M_\odot$), while the bottom row present high ejecta masses ($0.1 M_\odot$). We place no restrictions on ejecta velocities, morphology, composition, or viewing angle, such that each panel includes 9720 simulations (180 simulated kilonovae each with 54 viewing angles) of the full set of 48,600 LANL kilonovae.

Additionally, as higher redshift ($z \gtrsim 0.4$) kilonova emission is proportionally shifted to higher wavelengths, the Roman/H-band becomes less effective at detecting emission from high dynamical ejecta mass mergers. As a result, variation with dynamical ejecta mass decreases with redshift.

Different wavelength bands exhibit varying dependency on ejecta mass. Similarly to in the near-infrared (Roman/H-band), detectability at optical and ultraviolet wavelengths varies significantly with wind ejecta masses. However, optical and ultraviolet bands show little variability with dynamical ejecta masses. We define the variable v to quantify a given filter's sensitivity to a kilonova property such as ejecta mass. As an example, we can quantify the Roman/H-band's dependence on wind ejecta mass by comparing the 50% detectability contours (dot–dashed lines) in Figure 4.5. We label the 50% detectability contour for the lowest ejecta mass (top panel) and highest ejecta mass (bottom panel) as $g(t)$ and $f(t)$, respectively. We then quantify variability with mass as:

$$v = \frac{\int_{t_{\min}}^{t_{\max}} |f(t) - g(t)|\, dt}{\frac{1}{2}\int_{t_{\min}}^{t_{\max}} [f(t) + g(t)]\, dt}, \tag{4.2}$$

integrating from the smallest rest-frame time, $t_{\min} = 0.125$ d, to a maximum time of $t_{\max} = 20$ d. Values of v close to zero indicate negligible variation with a given parameter, while higher values of v indicate a significant dependence. There is no upper limit on v, although we note that a value of $v = 1$ corresponds to a three-fold enhancement in $z_{50\%}$ between two subsets of parameters (i.e. $f(t) = 3g(t)$). Based on the 50% contours in Figure 4.5, the Roman/H-band produces $v = 0.91$ for dynamical ejecta mass (left column) and $v = 0.94$ for wind ejecta mass (right column), suggesting that the Roman/H-band's detectability is slightly more dependent on wind ejecta mass than dynamical ejecta mass.

Figure 4.6 presents the variability scores for all filters in Figure 4.4 as a function of both dynamical ejecta mass (purple) and wind ejecta mass (orange). As anticipated, variability with dynamical ejecta mass increases with filter wavelength, while wind ejecta mass variability decreases with wavelength. Ultraviolet filters exhibit the largest dependence on wind ejecta mass, with the UVOT/u-band and ULTRASAT/NUV-band both yielding $v = 1.7$. The PRIME/H-band demonstrates the largest variability with dynamical ejecta mass, with $v = 1.3$. Variability scores directly relate to a filter's ability to constrain a given parameter from photometric observations (see Section 4.5).

The interplay between various kilonova parameters must be considered to fully capture variations in detectability. For example, masses for both dynamical and wind ejecta alter kilonova emission, and thus affect detectability. We explore the interrelation of dynamical and wind ejecta masses in Figure 4.7, using the Roman/H-band as an example. The left (right) panel restricts total ejecta mass to the lowest (highest) simulated mass, where total mass is the sum of both dynamical and wind ejecta masses. In both panels, the total mass is fixed while composition, morphology, viewing angles, and ejecta velocities vary, resulting in 1944 simulations in each panel (36 simulations each rendered at 54 viewing angles). Total mass significantly alters kilonova detectability in the Roman/H-band, with a variability $v = 1.6$ between the total masses of $0.002M_{\odot}$ (left panel) and $0.2M_{\odot}$ (right panel). Kilonovae with higher total ejecta masses are detectable at significantly higher redshifts than their low mass counterparts.

In addition to mass, other properties of neutron star mergers affect kilonova detectability. Luminosity may vary with viewing angle due to morphological effects (Korobkin et al., 2021) and lanthanide curtaining (Kasen et al., 2015). Additionally, ejecta composition

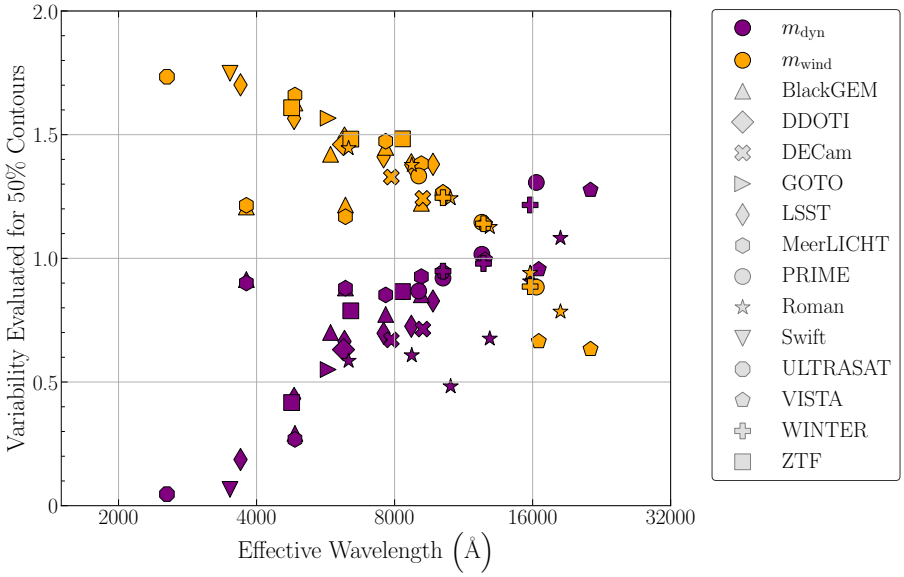

Figure 4.6. Mass-dependent variability for a selection of filters. Each symbol corresponds to one instrument, with an instrument's filters represented by their bandpass filter function's effective wavelength. The vertical axis represents each filter's dependence to either dynamical ejecta mass (purple) or wind ejecta mass (orange), as defined in Equation 4.2. Higher-wavelength filters are increasingly sensitive to variations in dymamical ejecta mass, while dependence on wind ejecta mass decreases with increasing filter wavelength.

significantly alters detectability in some filters, as lanthanide-poor ejecta yields significantly less luminous emission in the redder optical and infrared filters than mergers with lanthanide-rich ejecta. Ejecta velocity also has a pronounced effect on detectability, with higher ejecta velocities leading to earlier peak emission and subsequently more luminous kilonovae (e.g., Kasen et al., 2017). Numerous other factors alter simulated lightcurves and kilonova detectability including decay product thermalization and nuclear mass models (Lippuner & Roberts, 2015; Hotokezaka & Nakar, 2020). Considerably more uncertain nuclear physics may be propagated by allowing synthesized r-process abundance patterns

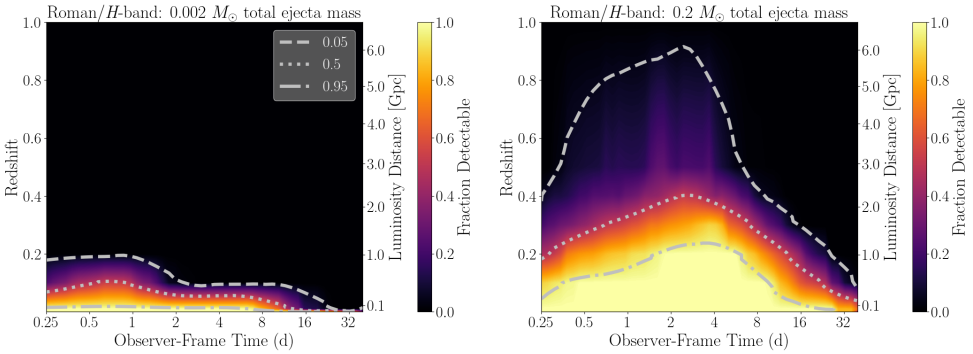

Figure 4.7. Detectability constraints for the Roman/H-band for two total ejecta masses, corresponding to the sum of dynamical and wind ejecta masses. The left panel displays the smallest total ejecta mass ($0.002M_\odot$), while the right panel corresponds to the largest total ejecta mass ($0.2M_\odot$). We place no restrictions on morphology, composition, viewing angle, or ejecta velocity, such that each panel includes 1944 simulations (36 simulations each with 54 viewing angles) of the full set of 48,600 LANL kilonova simulations.

to differ from the robust "strong" pattern, as done in Barnes et al. (2020) and Zhu et al. (2021).

4.5. Inferring Kilonova Properties with Wide-Field Observations

We can leverage parameter-dependent variations in kilonova detectability to infer ejecta properties and guide future observations. By coupling non-detections in wide-field transient searches with the kilonova detectability metrics presented in this work, constraints can be placed on kilonova ejecta properties. Non-detections are particularly constraining when a very large fraction of the GW sky localization is covered by multiple instruments or filters in a short period of time. To explore this, we consider observations in the Roman/H-band taking place two days post-trigger for a merger with a predicted

redshift of $z = 0.2$ (an ambitious $\sim$1 Gpc for current GW detectors). If these observations yield no transient detection, the total ejecta mass of an associated kilonova can be constrained to lower masses. This relationship is supported by Figure 4.7, as nearly 100% of simulated kilonovae with total ejecta masses of $0.2M_{\odot}$ are detectable two days post-merger at $z = 0.2$, while no kilonovae with total ejecta masses of $0.002M_{\odot}$ are detectable. Thus, a non-detection rules out the presence of a high-ejecta mass kilonova at $z = 0.2$.

This method has previously been employed by Thakur et al. 2020 to constrain parameters for a plausible kilonova associated with GW190814 (Abbott et al., 2020d). The authors compare upper limits from wide-field searches (including DDOTI) to the LANL kilonova grid, ruling out the presence of a high-mass ($> 0.1M_{\odot}$) and fast-moving (mean velocity $\geq 0.3c$) wind ejecta. Total ejecta masses $\geq 0.2M_{\odot}$ are also strongly disfavored by the upper limits.

Non-detections in wide-field searches may also guide subsequent observing schedules. For example, assume that you are planning additional follow-up observations after a non-detection in the BlackGEM/q-band at 12 hours post-merger for an event at $z = 0.05$ ($\sim$230 Mpc) that has not been detected by any other instrument. Of all the instruments in this study intended to follow-up GW candidate events (i.e. not including LSST or Roman), an additional BlackGEM observation is best suited for follow-up observations. This conclusion was reached by searching the 48,600 LANL kilonova models to identify kilonovae that are undetectable with BlackGEM at this redshift and time, but detectable with other instruments between 12 and 36 hours post-merger. Based on the LANL kilonova grid, 8% of simulated kilonovae are detectable 36 hours post-merger in the BlackGEM/q-band, but not detectable 12 hours post-merger. A selection of detectable

lightcurves is highlighted in the top panel of Figure 4.8, suggesting the presence of high mass ($\geq 0.03 M_{\odot}$) and slow-moving (mean velocity $< 0.15c$) wind ejecta. BlackGEM's q-band does not offer strong constraints on dynamical ejecta properties, consistent with the discussion in Section 4.4 and Figure 4.6. DECam can also provide useful follow-up observations after a non-detection at 12 hours, with 6% of simulated kilonovae detectable in DECam but not BlackGEM at the aforementioned times. Several instruments, including DDOTI, GOTO, VISTA, and PRIME, have negligible probability of detecting a kilonova at $z = 0.05$ following a BlackGEM non-detection. However, we note that both LSST and Roman have the highest probability of detecting a kilonova in this scenario, further highlighting their utility in kilonova searches.

We performed a similar analysis assuming a non-detection with WINTER (J-band) 12 hours post-merger for a GW event at $z = 0.05$ ($\sim$230 Mpc). Again, we searched the 48,600 LANL kilonova models for kilonovae that are undetectable with the WINTER/J-band at this redshift and time, but detectable with other instruments between 12 and 36 hours post-merger. Based on the LANL kilonova grid, 16% of simulated kilonovae are detectable with the WINTER/J-band 36 hours post-merger but not detectable 12 hours post-merger. These lightcurves are highlighted in the bottom panel of Figure 4.8. The WINTER non-detection and subsequent detection are consistent with large ejecta masses, with over 70% of orange lightcurves in Figure 4.8 corresponding to total ejecta masses $\geq 0.1 M_{\odot}$. WINTER's J-band offers constraints on both dynamical and wind ejecta parameters, as expected from Figure 4.6. In addition to WINTER, several instruments in this study are capable of observing kilonovae following a WINTER non-detection. For example, over

40% of simulated lightcurves are observable in the BlackGEM/q-band at 36 hours post-merger following a WINTER non-detection 24 hours earlier. Additional instruments have non-zero probabilities of detecting a kilonova under this scenario: GOTO can observe 6% of simulated kilonovae following a WINTER non-detection, DDOTI can observe 12%, VISTA can observe 15%, ZTF can observe 3%, and ULTRASAT can observe 1%.

These examples demonstrate how non-detections offer powerful constrains on kilonova ejecta properties. However, targeted observations with large aperture telescopes are better suited to sample kilonova emission after an initial detection in a wide-field search, providing multi-band observations over the duration of kilonova evolution. The LANL set of kilonova models provides a rich data set for thorough statistical analysis and optimization of kilonova observing strategies, beyond the study of non-detections in wide-field surveys, which we reserve for future work. In addition, we refer the reader to several other studies on the efficacy of Bayesian parameter estimation to infer kilonova parameters (i.e. Coughlin et al., 2018; Barbieri et al., 2019; Nicholl et al., 2021; Heinzel et al., 2021; Ristic et al., 2021).

4.6. Instrument Results

In this section, we briefly summarize each instrument's capacity for kilonova detection. We describe the accessible redshifts for each filter and the most probable times for kilonova detection. Additional figures for each instrument are presented in Appendix A.

BlackGEM − BlackGEM's optical and near-infrared filters are well-suited to detect kilonova emission, especially within two days post-merger. The broad q-band provides the best opportunities for detection, with 50% of simulated kilonovae detectable at $z = 0.072$

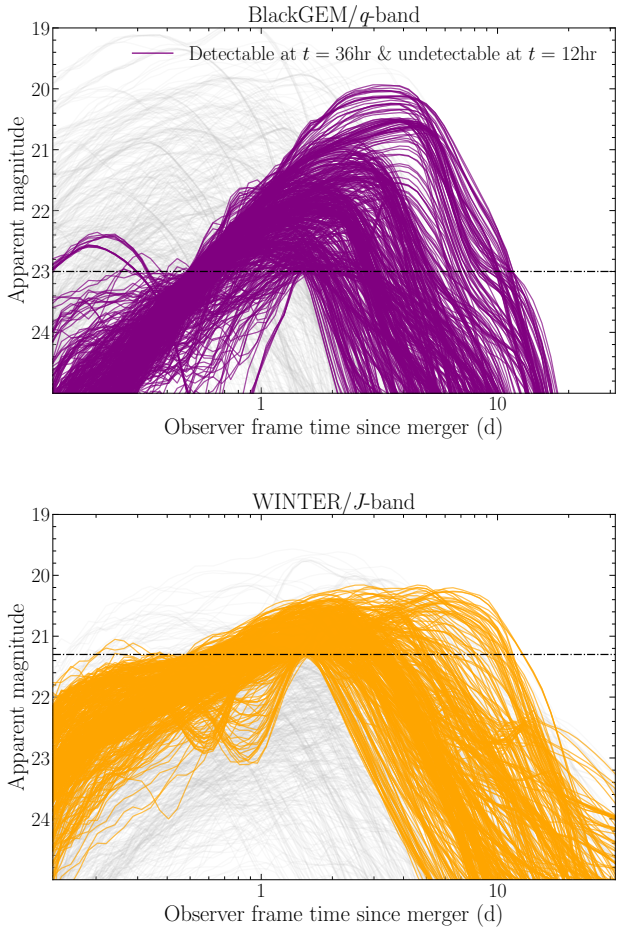

Figure 4.8. Simulated kilonova lightcurves, in the observer frame, in the BlackGem/q-band (*top*) and WINTER/J-band (*bottom*) for a merger at $z = 0.05$ ($\sim$230 Mpc). Purple and orange lightcurves are detectable at 36 hours but undetectable at 12 hours in the selected filter. Gray lightcurves do not meet this criterion. Horizontal dot–dashed lines correspond to limiting magnitudes in each filter. Only a subset of the full LANL kilonova grid is displayed, for clarity. These panels also highlight the variation in lightcurve behavior between optical (BlackGEM) and near-infrared (WINTER) filters.

($\sim$340 Mpc) and high wind ejecta mass kilonovae detectable out to $z \sim 0.2$. Our results largely support BlackGEM's plan to follow-up with the u, q, and i filters. However, we note that the z-band increases the detectable kilonova parameter space at later times

($t \geq 2$ d). As an example, nearly 10% of modeled kilonovae at $z = 0.01$ ($\sim$45 Mpc) are only observable in the z-band at $t = 4$ d (observer frame) and not observable in any other BlackGEM filters.

DDOTI − DDOTI's w filter can detect 50% of simulated kilonovae out to $z = 0.023$ ($\sim$100 Mpc), with a peak detectability 12 hours post-merger. DDOTI can follow-up some LIGO/Virgo/KAGRA candidate events with inferred redshifts out to $z = 0.073$ ($\sim$340 Mpc).

DECam − DECam's i- and z-bands are sensitive to kilonova detection, reaching $z_{50\%}$ of 0.058 ($\sim$270 Mpc) and 0.042 ($\sim$190 Mpc), respectively. Despite its lesser sensitivity the z-band may be better suited to detect kilonovae than the i-band, as nearly all simulated kilonovae detectable in the i-band are also detectable by the z-band. DECam is able to observe high ejecta mass kilonovae out to $z = 0.18$ ($\sim$900 Mpc).

GOTO − GOTO's L-band achieves a $z_{50\%} = 0.029$ ($\sim$130 Mpc), with peak detectability $\sim$8 hr post-merger. GOTO is able to follow-up high wind ejecta mass LIGO/Virgo/KAGRA candidate events with inferred redshifts out to $z = 0.097$ ($\sim$460 Mpc).

LSST − LSST can observe the most distant kilonovae out of all other ground-based instruments in the study. The g-band reaches the highest typical redshift reach, with a $z_{50\%} = 0.14$ peaking $\sim$8 hr post-merger. We especially encourage the use of LSST's g, r, and i filters for follow-up of relatively distant LIGO/Virgo/KAGRA candidate events ($z = 0.15 - 0.5$) that may not be observable with other ground-based, wide-field instruments.

MeerLICHT − Similarly to BlackGEM, MeerLICHT's broad q filter is the most sensitive at detecting kilonovae. MeerLICHT has better chances to observe kilonovae located

at $z < 0.074$ ($\sim$345 Mpc). For comparison, BlackGEM can detect kilonovae at over twice the distance of MeerLICHT.

PRIME − This ground-based infrared instrument is useful for late-time kilonova searches, with peak detectability between one and eight days post-merger. The most sensitive filter reaches a $z_{50\%} = 0.023$ ($\sim$100 Mpc), with some high ejecta mass kilonovae detectable out to $z = 0.067$ ($\sim$300 Mpc). Additionally, the PRIME/H-band may offer strong constraints on dynamical ejecta masses.

Roman − Roman provides an excellent tool for kilonova detection and GW follow-up. The Roman/R-band is the most sensitive filter in our study, reaching $z_{50\%} = 0.29$ with some kilonovae detectable out to $z \sim 1$. However, Roman's relatively small FoV precludes follow-up of GW candidate events with large localization areas. We encourage the use of the Roman Space Telescope for GW follow-up (see also Foley et al., 2019), especially for distant and/or well-localized candidate events.

UVOT − *Swift*/UVOT's u-band reaches a $z_{50\%} = 0.015$ ($\sim$70 Mpc), with a peak detectability around four hours post-merger. The u-band is well-suited to follow-up LIGO/Virgo/KAGRA candidate out to $z = 0.061$ ($\sim$280 Mpc). UVOT's detectability estimates may be biased by the lack of simulated lightcurves within three hours post-merger.

ULTRASAT − ULTRASAT provides an excellent tool for early kilonova detection. It's 200 deg^2 *NUV* filter can detect 50% of simuilated kilonovae out to $z = 0.022$ ($\sim$100 Mpc), with high wind ejecta mass mergers detectable out to $z = 0.1$ within the first 12 hours post-merger. We caution the reader in their interpretation of ULTRASAT results. This study is based on an approximate ULTRASAT filter, as no finalized filter is publicly

available. We anticipate that ULTRASAT's detectability estimate would increase with the availability of simulated lightcurves before three hours.

VISTA − VISTA is one of the most sensitive ground-based infrared facilities in the study, with $z_{50\%} = 0.038$ (∼170 Mpc) for the Y-band. VISTA is able to follow-up high ejecta mass LIGO/Virgo/KAGRA candidate events out to $z = 0.094$ (∼450 Mpc) one day post-merger. Additionally, VISTA observations may provide strong constraints on dynamical ejecta masses.

WINTER − Similarly to VISTA, WINTER is one of the most sensitive ground-based infrared facilities in the study, with $z_{50\%} = 0.038$ (∼170 Mpc) for the Y-band. WINTER is capable of follow-up some nearby (within $\sim$ 100 Mpc) mergers over two weeks post-merger. WINTER can observe high ejecta mass kilonovae out to $z = 0.093$ (∼440 Mpc) one day post-merger, in addition to offering tight constraints on dynamical ejecta mass.

ZTF − ZTF is well-suited to search large sky localization regions for relatively nearby kilonovae ($z \lesssim 0.1$), with a typical redshift reach of $z \sim 0.02$ (∼100 Mpc) in the g-, r-, and i-bands. ZTF is able to detect a subset of high ejecta mass kilonovae out to $z = 0.094$ (∼445 Mpc).

4.7. Discussion & Conclusions

This study explores kilonova searches with current and upcoming wide-field instruments. This analysis relies on the LANL grid of kilonova simulations (Wollaeger et al., 2021), a set of 48,600 radiative transfer models which span a variety of ejecta parameters. Based on these simulations, we quantify each instrument's ability to detect a kilonova, recording the fraction of observable kilonovae from the simulation grid for various times

and redshifts. The 44 filters in this study have significant variations in their typical redshift reach; ultraviolet filters are restricted to observing nearby kilonovae ($z < 0.3$), while the Roman Space Telescope can observe a subset of kilonovae out to $z \sim 1$. We concentrate on wide-field kilonova searches following a GW candidate event, although the conclusions of this study are equally relevant to kilonova searches following poorly-localized short GRBs. Additionally, the framework presented in this study is easily adaptable, and can be applied to searches performed by more sensitive, smaller FoV instruments (e.g., Gemini, Keck, GTC, VLT, SALT, *HST*, *JWST*) following the detection of a kilonova. Additionally, we remind the reader that the facilities studied in this work do not constitute a comprehensive selection of wide-field instruments.

Detecting, analyzing, and modeling kilonovae is a new and evolving science; many uncertainties remain after only a single confident multi-messenger observation with GWs (Abbott et al., 2017a). As a result, the models that lay the foundation of this study rely on numerous physical assumptions, including the use of a specific nuclear mass model (FRDM, Möller et al., 1995) and decay product thermalization (Barnes et al., 2016; Rosswog et al., 2017). While the LANL grid of kilonova models covers a wide range of kilonova parameters (see Section 4.3 and Table 4.2), this simulation grid does not span all possible ejecta scenarios. For instance, the simulations do not encompass all possible variations in ejecta morphology (Korobkin et al., 2021) or composition (Even et al., 2019). We also ignore changes in the detected UVOIR emission due to extinction or the presence of contamination from either a sGRB afterglow or host galaxy, which will be expanded upon in a future work.

Our work produces results that are consistent with the detectability study presented by Scolnic et al. (2018), which determined kilonova detectability using an AT 2017gfo-like model. Scolnic et al. (2018) predict a redshift range of $z = 0.02-0.25$ for LSST, consistent with our redshift range of $z = 0.035 - 0.48$ for the most sensitive LSST filter. Our results are also broadly consistent with the detectability estimates presented by Rastinejad et al. (2021), which leveraged three kilonova models (in addition to AT 2017gfo) to infer the maximum redshift of kilonova detection.

Similarly to Scolnic et al. (2018), we focus only on the ability of these instruments to detect a kilonova, and not its unambiguous identification (as this outcome depends on multi-epoch observations across a range of filters). Wide-field searches are likely to uncover numerous other transient signals (e.g., supernovae), potentially masquerading as a kilonova signal (see Cowperthwaite & Berger 2015 for a discussion of kilonova contaminants). LIGO/Virgo/KAGRA candidate events constrained to large localization volumes are increasingly likely to reveal false positive kilonova candidates, further necessitating the need for repeated observations of each field to rapidly distinguish a kilonova candidate. In future work, we intend to provide methods to disentangle kilonova candidates from other transients with a limited number of photometric observations.

We caution the reader in the interpretation of our results and emphasize that the typical redshift reach values presented in Table 4.1 and Figure 4.4 refer to the redshifts at which 50% of *simulated kilonovae* are detectable. This is not equivalent to the probability of detection for the full population of kilonovae. For example, our results claim that 50% of simulated kilonovae are observable in the LSST/r-band at $z = 0.12$. This does not imply that the LSST/r-band has a 50% probability of observing a kilonova at $z = 0.12$. Such a

statement relies on a realistic astrophysical distribution of kilonova ejecta properties, while our study is based on a uniformly sampled grid of models. This study could be expanded to draw from a distribution of kilonova models with the availability of more robust models for binary neutron star populations, neutron star equation of state, and mappings between compact object progenitors and ejecta. Additionally, this work could be further expanded to include redshift-dependent rates of neutron star mergers and associated GW detection.

Multi-band observations capture variability in kilonova emission and provide tighter constraints on kilonova properties, such as the composition and ejecta mass. Once a kilonova is identified, targeted follow-up observations at several wavelengths (and times) are necessary to constrain ejecta properties. Additionally, instruments must be distributed in geographically disparate locations, similarly to the Las Cumbres Observatory Global Telescope Network (Brown et al., 2013), to maximize the probability of kilonova detection. Instrument response time may also vary significantly based on the location of a neutron star merger on the sky. We stress the utility of both ground-based and space-based detectors to allow for rapid follow-up post-trigger, aiding in kilonova detection.

Kilonova searches also benefit from a variety of fields-of-view and exposure times, such as the collection of instruments in this study. Wide FoV instruments with short exposure times are best suited to rapidly scan the sky for GW candidate events localized to large regions of the sky, while smaller FoV instruments with longer exposure times are better suited for well-localized ($\lesssim 10$ deg^2) events. For example, while the Roman Space Telescope has the largest typical redshift reach in this study, less sensitive, wider FoV instruments are better able to follow-up GW candidate events with large localization areas.

Based on the results of our study, we present the following findings to guide observing strategies and commissioning of future instruments:

(1) This study demonstrates the utility of a diversity of wide-field instruments to search for kilonovae following GW detections. This includes a variety in instrument location, sensitivity, FoV, cadence, exposure time, and wavelength coverage. Additionally, rapid dissemination of both GW and electromagnetic search results is critical to optimize counterpart searches among this diverse array of instruments.

(2) Early observations increase the probability of observing a kilonova, especially at ultraviolet and optical wavelengths. Based on the results in this study, we stress the importance of early-time observations for kilonova detection. Although not a focus of this study, we note that early observations offer the most stringent constraints on wind ejecta properties.

(3) More sensitive wide-field ultraviolet instruments are needed for kilonova detection as LIGO/Virgo/KAGRA reach design sensitivity. The ultraviolet instruments in this study can observe only a small fraction of kilonovae beyond $z \sim 0.1$, which is equivalent to the BNS horizon redshift of advanced LIGO at design sensitivity (Abbott et al., 2020a).

(4) We promote the construction of additional wide-field near-infrared instruments. Compared to optical instruments, few ground-based near-infrared instruments are available for GW follow-up, potentially reducing the probability of kilonova detection. Near-infrared instruments hold immense promise for kilonova detection,

as they are able to detect kilonovae within several days post-merger as opposed to the limited timescale accessible to ultraviolet and optical instruments.

(5) We recommend using this work as a guide for scheduling future kilonova observations. Based on the results of this study, we encourage observations if more than 5% of simulated kilonovae are detectable at a given time and redshift based on the figures in Appendix A.

(6) Low-latency GW products, such as sky localization and distance estimates, should be used to alter observing strategies. We recommend comparing low-latency distance estimates to the detectability estimates provided in this work.

The current and upcoming wide-field instruments in this study are well-poised to observe kilonovae coincident with GW events in the advanced detector era. However, the landscape of multi-messenger astronomy with GWs will change through the construction of new detectors. Sky localization will improve as additional GW detectors are commissioned (Abbott et al., 2020a), allowing larger aperture instruments to cover higher percentages of the localization region. Simultaneously, enhanced GW detector sensitivity will reveal neutron star mergers at cosmic distances previously inaccessible through GWs alone, with the Einstein Telescope and Cosmic Explorer detecting BNS mergers at redshifts of out to $z \sim 4$ and $z \sim 10$, respectively (Hall & Evans, 2019). To match the increase in GW detector sensitivity, innovative UVOIR instruments must be constructed to observe kilonovae in the era of third-generation GW detectors.

CHAPTER 5

Concluding Remarks

GW170817, the first MM detection with GWs (Abbott et al., 2017a), ushered a new era of astronomy. This single detection confirmed long-standing theories in astronomy while providing a laboratory for additional studies in nuclear physics, cosmology, and general relativity. However, addition MM observations of NSMs are needed to build upon the discovered of GW170817 and further test fundamental physical theories. These observations offer a unique laboratory to explore the nuclear EOS of matter at extreme densities (i.e. Lattimer & Prakash, 2007, 2016; Özel & Freire, 2016; Abbott et al., 2018b), with nuclear physics constraints tightening with each additional observation. Additionally, MM observations allow additional tests of general relativity (Damour & Taylor, 1992; Kramer & Wex, 2009; Damour, 2009; Abbott et al., 2019c), beyond tests available with single-messenger observations (i.e. only GW or only EM). These observations also offer an independent measure of the Hubble parameter (Schutz, 1986; Holz & Hughes, 2005; Dalal et al., 2006; Nissanke et al., 2013a; Abbott et al., 2017e), testing key theories in cosmology. More observations of BNS and NSBH mergers, both with or without EM signatures, will also significantly increase our understanding of neutron star populations, such as the mass distribution (Zhu et al., 2018; Farrow et al., 2019; Wysocki et al., 2019), in addition to the formation and rates of neutron star mergers (see Kalogera et al. 2007, Tauris et al. 2017, and Abadie et al. 2010 for reviews). Lastly, additional observations of NSMs are necessary to further constrain the role of mergers in Galactic r-process enrichment (i.e.

Côté et al., 2018, 2019). We can constrain the typical rate of r-process production in a NSM by repeatedly coupling UVOIR observations of kilonovae to detailed radiative transfer simulations.

Through this thesis, I have demonstrated that the prospects for additional MM observations of NSMs are immensely promising. Robust data analysis techniques and glitch mitigation methods allow for the production of sky localization maps within minutes of GW detection, and sky localization will continue to improve as additional GW detectors are commissions. I have also demonstrated that a diverse range of UVOIR wide-field instruments are well suited to detect kilonovae throughout the advanced detector era.

There are an infinite number of avenues to expand this work, which cannot be tersely compiled in this thesis. Instead, I offer a brief selection of opportunities to expand this study below:

(1) Radiative transfer simulations of kilonova emission can be leveraged to produce Bayesian parameter estimation techniques for kilonova ejecta parameters (the foundations for this are set in numerous papers including Coughlin et al. 2018; Barbieri et al. 2019; Nicholl et al. 2021; Heinzel et al. 2021; Ristic et al. 2021). Parameter estimation can potentially be combined with GW emission.

(2) The study presented in Chapter 4 can easily be adapted to include additional instruments, albeit other wide-field instruments or smaller FoV telescopes.

(3) We can combine models of UVOIR emission from sGRB afterglows to further refine the detectability statements in Chapter 4.

(4) Radiative transfer simulations of kilonova emission can be compared to simulations of other transient signals, such as Type Ia supernovae, to establish a

statistically rigorous method to discriminate kilonova and supernova transient signals with limited photometric observations.

(5) Work is underway to use machine learning techniques in conjunction with the radiative transfer simulations in Wollaeger et al. (2021) and Ristic et al. (2021) to infer kilonova parameters (i.e. viewing angle) in addition to optimizing kilonova observing strategies.

We note that numerous studies within this dissertation rely on specific astrophysical models, such as GW waveform calculations or radiative transfer models of kilonova emission. These models contain multiple approximations and assumptions, which may bias some of the presented results. All studies presented in this dissertation can be reproduced and further constrained as models continue to improve.

5.1. Additional Projects

I have made significant contributions to numerous other publications throughout graduate school, in addition to the chapters presented in this thesis. I summarize some of these additional projects below, in order of publication:

Astrophysical Prior Information and Gravitational-wave Parameter Estimation (Pankow et al., 2017) – In this paper, we explore how MM observations of NSMs improve GW parameter estimates. We assume several extrinsic GW properties are known from EM observations, including inclination, distance, and sky localization, and explore how this parameter constraint improved parameter recovery of intrinsic astrophysical parameters such as masses and spins. We conclude that the use of additional

information from EM observations does not improve the measurement of the intrinsic parameters significantly.

Constraining Formation Models of Binary Black Holes with Gravitational-wave Observations (Zevin et al., 2017) – We employ a hierarchical Bayesian analysis to determine the number of BBH observations needed to infer the relative fraction of mergers formed in globular clusters as opposed to isolated binary evolution, concluding that at least $\mathcal{O}(100)$ observations are needed to constrain BBH formation mechanisms. I directly contributed to the implementation of Fisher matrix parameter estimates in this publication.

GW170608: Observation of a 19 Solar-mass Binary Black Hole Coalescence (Abbott et al., 2017h) – This LVC publication describes the detection of a low-mass BBH with the advanced LIGO detectors. At the time of detection, this event was the lowest mass BBH system ever detected. I jointly led data analysis and parameter estimation for this event on behalf of the entire collaboration. Additionally, I was a member of the paper editorial team, leading the astrophysical interpretations section of the publication.

GWTC-1: A Gravitational-Wave Transient Catalog of Compact Binary Mergers Observed by LIGO and Virgo during the First and Second Observing Runs (Abbott et al., 2019a) – This LVC publication presents a full set of eleven confident GW detections in advanced LIGO and Virgo's first and second observing runs. I jointly led parameter estimation for GW170608 on behalf of the collaboration and provided updated astrophysical constraints from Abbott et al. (2017h).

GW190425: Observation of a Compact Binary Coalescence with Total Mass 3.4 Solar Masses (Abbott et al., 2020b) – This LVC publication presents the detection of a GW event consistent with the merger of two neutron stars. The neutron stars in this merger are higher-mass than typically observed neutron stars. I jointly led a review of the waveform systematics related to the `IMRPhenomP_NRTidal` waveform, resulting in an associated data release (Baylor et al., 2019).

A search for optical and near-infrared counterparts of the compact binary merger GW190814 (Thakur et al., 2020) – This publication presents wide-field and galaxy-targeted observations following the GW detection of GW190814. No EM counterpart was detected for this observation. I directly contributed to kilonova data analysis of this event, comparing wide-field non-detections to radiative transfer simulations to constrain parameters of a potential kilonova associated with this binary.

A tale of two mergers: constraints on kilonova detection in two short GRBs at z $\sim$ 0.5 (O'Connor et al., 2021) – This publication presents broadband observations following two sGRB observations: GRB 160624A and GRB 200522A. I directly contributed to kilonova data analysis for both events, comparing observations to a set of radiative transfer kilonova simulations, inferring parameters of a potential kilonova associated with each merger.

Axisymmetric Radiative Transfer Models of Kilonovae (Korobkin et al., 2021) – This publication provides a large set of radiative transfer simulation exploring how kilonova spectra and lightcurves vary with ejecta morphology and viewing angle. We demonstrate that morphology has a significant effect on kilonova emission.

GWTC-2: Compact Binary Coalescences Observed by LIGO and Virgo during the First Half of the Third Observing Run (Abbott et al., 2021) – This LVC publication presents 39 additional GW detections made during the first half of advanced LIGO and Virgo's third observing run (O3a). I jointly led GW parameter estimation for GW190727, a BBH merger. Additionally, I served a leading role in education and public outreach associated with the announcement of this publication.

Interpolating Detailed Simulations of Kilonovae: Adaptive Learning and Parameter Inference Applications (Ristic et al., 2021) – In this study, we apply machine learning techniques to iteratively choose additional input parameters to create new kilonova radiative transfer simulations. We also demonstrate how these radiative transfer simulations can be used for Bayesian parameter estimation of kilonova ejecta parameters.

A Broad Grid of 2D Kilonova Emission Models (Wollaeger et al., 2021) – In this publication, we present a set of 900 radiative transfer kilonova simulations for a wide range of input parameters. I was a main contributing member of this publication and directly contributed to an analysis on variation in kilonova emission with viewing angle. This simulations are used in numerous other publications including Thakur et al. (2020), O'Connor et al. (2021), Chase et al. (2021), Ristic et al. (2021), and Bruni et al. (2021).

References

Aasi, J., Abbott, B. P., Abbott, R., et al. 2015, Classical and Quantum Gravity, 32, 074001, doi: 10.1088/0264-9381/32/7/074001

Abadie, J., Abbott, B. P., Abbott, R., et al. 2010, Classical and Quantum Gravity, 27, 173001, doi: 10.1088/0264-9381/27/17/173001

Abbott, B. P., Abbott, R., Abbott, T. D., et al. 2016a, PhRvL, 116, 061102, doi: 10.1103/PhysRevLett.116.061102

—. 2016b, ApJL, 832, L21, doi: 10.3847/2041-8205/832/2/L21

—. 2016c, Living Reviews in Relativity, 19, 1, doi: 10.1007/lrr-2016-1

—. 2016d, ApJL, 826, L13, doi: 10.3847/2041-8205/826/1/L13

—. 2016e, Classical and Quantum Gravity, 33, 134001, doi: 10.1088/0264-9381/33/13/134001

—. 2017a, ApJL, 848, L12, doi: 10.3847/2041-8213/aa91c9

—. 2017b, PhRvL, 119, 161101, doi: 10.1103/PhysRevLett.119.161101

—. 2017c, ApJL, 848, L13, doi: 10.3847/2041-8213/aa920c

—. 2017d, ApJL, 850, L39, doi: 10.3847/2041-8213/aa9478

—. 2017e, Nature, 551, 85, doi: 10.1038/nature24471

—. 2017f, PhRvL, 119, 141101, doi: 10.1103/PhysRevLett.119.141101

—. 2017g, Classical and Quantum Gravity, 34, 044001, doi: 10.1088/1361-6382/aa51f4

—. 2017h, ApJL, 851, L35, doi: 10.3847/2041-8213/aa9f0c

—. 2018a, Classical and Quantum Gravity, 35, 065010, doi: 10.1088/1361-6382/aaaafa

—. 2018b, PhRvL, 121, 161101, doi: 10.1103/PhysRevLett.121.161101

—. 2019a, Physical Review X, 9, 031040, doi: 10.1103/PhysRevX.9.031040

—. 2019b, Physical Review X, 9, 011001, doi: 10.1103/PhysRevX.9.011001

—. 2019c, PhRvL, 123, 011102, doi: 10.1103/PhysRevLett.123.011102

—. 2020a, Living Reviews in Relativity, 23, 3, doi: 10.1007/s41114-020-00026-9

—. 2020b, ApJL, 892, L3, doi: 10.3847/2041-8213/ab75f5

Abbott, R., Abbott, T. D., Abraham, S., et al. 2020c, PhRvD, 102, 043015, doi: 10.1103/PhysRevD.102.043015

—. 2020d, ApJL, 896, L44, doi: 10.3847/2041-8213/ab960f

—. 2021, Physical Review X, 11, 021053, doi: 10.1103/PhysRevX.11.021053

Acernese, F., Agathos, M., Agatsuma, K., et al. 2015, Classical and Quantum Gravity, 32, 024001, doi: 10.1088/0264-9381/32/2/024001

Ackley, K., Amati, L., Barbieri, C., et al. 2020, A&A, 643, A113, doi: 10.1051/0004-6361/202037669

Akutsu, T., Ando, M., Arai, K., et al. 2019, Nature Astronomy, 3, 35, doi: 10.1038/s41550-018-0658-y

Alekseev, E. N., Alekseeva, L. N., Volchenko, V. I., & Krivosheina, I. V. 1987, Soviet Journal of Experimental and Theoretical Physics Letters, 45, 589

Allen, B., Anderson, W. G., Brady, P. R., Brown, D. A., & Creighton, J. D. E. 2012, PhRvD, 85, 122006, doi: 10.1103/PhysRevD.85.122006

Amaro-Seoane, P., Audley, H., Babak, S., et al. 2017, arXiv e-prints, arXiv:1702.00786. https://arxiv.org/abs/1702.00786

Andreoni, I., Ackley, K., Cooke, J., et al. 2017, PASA, 34, e069, doi: 10.1017/pasa.2017.65

Andreoni, I., Goldstein, D. A., Kasliwal, M. M., et al. 2020, ApJ, 890, 131, doi: 10.3847/1538-4357/ab6a1b

Andreoni, I., Coughlin, M. W., Kool, E. C., et al. 2021, arXiv e-prints, arXiv:2104.06352. https://arxiv.org/abs/2104.06352

Antoniadis, J., Freire, P. C. C., Wex, N., et al. 2013, Science, 340, 448, doi: 10.1126/science.1233232

Arcavi, I. 2018, ApJL, 855, L23, doi: 10.3847/2041-8213/aab267

Arcavi, I., Hosseinzadeh, G., Howell, D. A., et al. 2017, Nature, 551, 64, doi: 10.1038/nature24291

Artale, M. C., Bouffanais, Y., Mapelli, M., et al. 2020, MNRAS, 495, 1841, doi: 10.1093/mnras/staa1252

Arzoumanian, Z., Baker, P. T., Brazier, A., et al. 2018, ApJ, 859, 47, doi: 10.3847/1538-4357/aabd3b

Ascenzi, S., Coughlin, M. W., Dietrich, T., et al. 2019, MNRAS, 486, 672, doi: 10.1093/mnras/stz891

Baade, W., & Zwicky, F. 1934, Physical Review, 46, 76, doi: 10.1103/PhysRev.46.76.2

Banerjee, S., Tanaka, M., Kawaguchi, K., Kato, D., & Gaigalas, G. 2020, ApJ, 901, 29, doi: 10.3847/1538-4357/abae61

Banerji, M., Jouvel, S., Lin, H., et al. 2015, MNRAS, 446, 2523, doi: 10.1093/mnras/stu2261

Barbieri, C., Salafia, O. S., Perego, A., Colpi, M., & Ghirlanda, G. 2019, A&A, 625, A152, doi: 10.1051/0004-6361/201935443

Bardeen, J. M., Press, W. H., & Teukolsky, S. A. 1972, ApJ, 178, 347, doi: 10.1086/151796

Barnes, J., Kasen, D., Wu, M.-R., & Martínez-Pinedo, G. 2016, ApJ, 829, 110, doi: 10.3847/0004-637X/829/2/110

Barnes, J., Zhu, Y. L., Lund, K. A., et al. 2020, arXiv e-prints, arXiv:2010.11182. https://arxiv.org/abs/2010.11182

Bartos, I., Huard, T. L., & Márka, S. 2016, ApJ, 816, 61, doi: 10.3847/0004-637X/816/2/61

Baylor, A., Smith, R., & Chase, E. 2019, IMRPhenomPv2_NRTidal_GW190425_narrow_Mc, Zenodo, doi: 10.5281/zenodo.3478659

Bellm, E. C., Kulkarni, S. R., Graham, M. J., et al. 2019, PASP, 131, 018002, doi: 10.1088/1538-3873/aaecbe

Berger, E. 2014, ARA&A, 52, 43, doi: 10.1146/annurev-astro-081913-035926

Berger, E., Fong, W., & Chornock, R. 2013, ApJL, 774, L23, doi: 10.1088/2041-8205/774/2/L23

Berry, C. P. L., Mandel, I., Middleton, H., et al. 2015, ApJ, 804, 114, doi: 10.1088/0004-637X/804/2/114

Bionta, R. M., Blewitt, G., Bratton, C. B., et al. 1987, PhRvL, 58, 1494, doi: 10.1103/PhysRevLett.58.1494

Biswas, R., Blackburn, L., Cao, J., et al. 2013, PhRvD, 88, 062003, doi: 10.1103/PhysRevD.88.062003

Blanton, M. R., Brinkmann, J., Csabai, I., et al. 2003, AJ, 125, 2348, doi: 10.1086/342935

Blinnikov, S. I., Novikov, I. D., Perevodchikova, T. V., & Polnarev, A. G. 1984, Soviet Astronomy Letters, 10, 177. https://arxiv.org/abs/1808.05287

Bloemen, S., Groot, P., Nelemans, G., & Klein-Wolt, M. 2015, in Astronomical Society of the Pacific Conference Series, Vol. 496, Living Together: Planets, Host Stars and Binaries, ed. S. M. Rucinski, G. Torres, & M. Zejda, 254

Breu, C., & Rezzolla, L. 2016, MNRAS, 459, 646, doi: 10.1093/mnras/stw575

Broekgaarden, F. S., Berger, E., Neijssel, C. J., et al. 2021, arXiv e-prints, arXiv:2103.02608. https://arxiv.org/abs/2103.02608

Brown, T. M., Baliber, N., Bianco, F. B., et al. 2013, PASP, 125, 1031, doi: 10.1086/673168

Bruni, G., O'Connor, B., Matsumoto, T., et al. 2021, MNRAS, doi: 10.1093/mnrasl/slab046

Burbidge, E. M., Burbidge, G. R., Fowler, W. A., & Hoyle, F. 1957, Reviews of Modern Physics, 29, 547, doi: 10.1103/RevModPhys.29.547

Cameron, A. G. W. 1957, PASP, 69, 201, doi: 10.1086/127051

Chase, E. A., O'Connor, B., Fryer, C. L., et al. 2021, arXiv e-prints, arXiv:2105.12268. https://arxiv.org/abs/2105.12268

Chen, H.-Y., & Holz, D. E. 2016, arXiv e-prints, arXiv:1612.01471. https://arxiv.org/abs/1612.01471

Chen, H.-Y., Holz, D. E., Miller, J., et al. 2021, Classical and Quantum Gravity, 38, 055010, doi: 10.1088/1361-6382/abd594

Chornock, R., Berger, E., Kasen, D., et al. 2017, ApJL, 848, L19, doi: 10.3847/2041-8213/aa905c

Cornish, N. J., & Littenberg, T. B. 2015, Classical and Quantum Gravity, 32, 135012, doi: 10.1088/0264-9381/32/13/135012

Corral-Santana, J. M., Casares, J., Muñoz-Darias, T., et al. 2016, A&A, 587, A61, doi: 10.1051/0004-6361/201527130
Côté, B., Fryer, C. L., Belczynski, K., et al. 2018, ApJ, 855, 99, doi: 10.3847/1538-4357/aaad67
Côté, B., Eichler, M., Arcones, A., et al. 2019, ApJ, 875, 106, doi: 10.3847/1538-4357/ab10db
Coughlin, M. W., Dietrich, T., Doctor, Z., et al. 2018, MNRAS, 480, 3871, doi: 10.1093/mnras/sty2174
Coughlin, M. W., Ahumada, T., Anand, S., et al. 2019, ApJL, 885, L19, doi: 10.3847/2041-8213/ab4ad8
Coulter, D. A., Foley, R. J., Kilpatrick, C. D., et al. 2017, Science, 358, 1556, doi: 10.1126/science.aap9811
Covino, S., Wiersema, K., Fan, Y. Z., et al. 2017, Nature Astronomy, 1, 791, doi: 10.1038/s41550-017-0285-z
Cowperthwaite, P. S., & Berger, E. 2015, ApJ, 814, 25, doi: 10.1088/0004-637X/814/1/25
Cowperthwaite, P. S., Villar, V. A., Scolnic, D. M., & Berger, E. 2019, ApJ, 874, 88, doi: 10.3847/1538-4357/ab07b6
Cowperthwaite, P. S., Berger, E., Villar, V. A., et al. 2017, ApJL, 848, L17, doi: 10.3847/2041-8213/aa8fc7
Cutler, C., & Flanagan, É. E. 1994, PhRvD, 49, 2658, doi: 10.1103/PhysRevD.49.2658
Dalal, N., Holz, D. E., Hughes, S. A., & Jain, B. 2006, PhRvD, 74, 063006, doi: 10.1103/PhysRevD.74.063006
Damour, T. 2009, Binary Systems as Test-Beds of Gravity Theories, ed. M. Colpi, P. Casella, V. Gorini, U. Moschella, & A. Possenti, Vol. 359, 1, doi: 10.1007/978-1-4020-9264-0_1
Damour, T., Iyer, B. R., & Sathyaprakash, B. S. 2002, PhRvD, 66, 027502, doi: 10.1103/PhysRevD.66.027502
Damour, T., & Taylor, J. H. 1992, PhRvD, 45, 1840, doi: 10.1103/PhysRevD.45.1840
Davis, D., Areeda, J. S., Berger, B. K., et al. 2021, arXiv e-prints, arXiv:2101.11673. https://arxiv.org/abs/2101.11673
de Wet, S., Groot, P. J., Bloemen, S., et al. 2021, arXiv e-prints, arXiv:2103.02399. https://arxiv.org/abs/2103.02399
Demorest, P. B., Pennucci, T., Ransom, S. M., Roberts, M. S. E., & Hessels, J. W. T. 2010, Nature, 467, 1081, doi: 10.1038/nature09466
Dietrich, T., Khan, S., Dudi, R., et al. 2019, PhRvD, 99, 024029, doi: 10.1103/PhysRevD.99.024029
Drout, M. R., Piro, A. L., Shappee, B. J., et al. 2017, Science, 358, 1570, doi: 10.1126/science.aaq0049
Dyer, M. J. 2020, PhD thesis, University of Sheffield

Dyer, M. J., Dhillon, V. S., Littlefair, S., et al. 2018, in Society of Photo-Optical Instrumentation Engineers (SPIE) Conference Series, Vol. 10704, Observatory Operations: Strategies, Processes, and Systems VII, 107040C, doi: 10.1117/12.2311865

Dyer, M. J., Steeghs, D., Galloway, D. K., et al. 2020, in Society of Photo-Optical Instrumentation Engineers (SPIE) Conference Series, Vol. 11445, Society of Photo-Optical Instrumentation Engineers (SPIE) Conference Series, 114457G, doi: 10.1117/12.2561008

Eichler, D., Livio, M., Piran, T., & Schramm, D. N. 1989, Nature, 340, 126, doi: 10.1038/340126a0

Einstein, A. 1916, Sitzungsberichte der Königlich Preußischen Akademie der Wissenschaften (Berlin), 1, 688

—. 1918, Sitzungsberichte der Königlich Preußischen Akademie der Wissenschaften (Berlin), 1, 154

Essick, R., Blackburn, L., & Katsavounidis, E. 2013, Classical and Quantum Gravity, 30, 155010, doi: 10.1088/0264-9381/30/15/155010

Evans, P. A., Kennea, J. A., Palmer, D. M., et al. 2016, MNRAS, 462, 1591, doi: 10.1093/mnras/stw1746

Evans, P. A., Cenko, S. B., Kennea, J. A., et al. 2017, Science, 358, 1565, doi: 10.1126/science.aap9580

Even, W., Korobkin, O., Fryer, C. L., et al. 2019, arXiv e-prints, arXiv:1904.13298. https://arxiv.org/abs/1904.13298

Fairhurst, S. 2011a, New Journal of Physics, 13, 069602, doi: 10.1088/1367-2630/13/6/069602

—. 2011b, Classical and Quantum Gravity, 28, 105021, doi: 10.1088/0264-9381/28/10/105021

Farr, B., Berry, C. P. L., Farr, W. M., et al. 2016, ApJ, 825, 116, doi: 10.3847/0004-637X/825/2/116

Farr, W. M., Farr, B., & Littenberg, T. 2015, Modelling Calibration Errors In CBC Waveforms, Tech. Rep. LIGO-T1400682, LIGO Project. https://dcc.ligo.org/LIGO-T1400682/public

Farr, W. M., Sravan, N., Cantrell, A., et al. 2011, ApJ, 741, 103, doi: 10.1088/0004-637X/741/2/103

Farrow, N., Zhu, X.-J., & Thrane, E. 2019, ApJ, 876, 18, doi: 10.3847/1538-4357/ab12e3

Fernández, R., & Metzger, B. D. 2016, Annual Review of Nuclear and Particle Science, 66, 23, doi: 10.1146/annurev-nucl-102115-044819

Finn, L. S., & Chernoff, D. F. 1993, PhRvD, 47, 2198, doi: 10.1103/PhysRevD.47.2198

Flanagan, É. É., & Hinderer, T. 2008, PhRvD, 77, 021502, doi: 10.1103/PhysRevD.77.021502

Flanagan, É. É., & Hughes, S. A. 1998, PhRvD, 57, 4535, doi: 10.1103/PhysRevD.57.4535

Flaugher, B., Diehl, H. T., Honscheid, K., et al. 2015, AJ, 150, 150, doi: 10.1088/0004-6256/150/5/150

Foley, R., Bloom, J. S., Cenko, S. B., et al. 2019, BAAS, 51, 305. https://arxiv.org/abs/1903.04582
Fong, W., Berger, E., Margutti, R., & Zauderer, B. A. 2015, ApJ, 815, 102, doi: 10.1088/0004-637X/815/2/102
Fong, W., Laskar, T., Rastinejad, J., et al. 2021, ApJ, 906, 127, doi: 10.3847/1538-4357/abc74a
Fonseca, E., Pennucci, T. T., Ellis, J. A., et al. 2016, ApJ, 832, 167, doi: 10.3847/0004-637X/832/2/167
Fontes, C. J., Fryer, C. L., Hungerford, A. L., Wollaeger, R. T., & Korobkin, O. 2020, MNRAS, 493, 4143, doi: 10.1093/mnras/staa485
Fontes, C. J., Zhang, H. L., Abdallah, J., J., et al. 2015, Journal of Physics B Atomic Molecular Physics, 48, 144014, doi: 10.1088/0953-4075/48/14/144014
Fragos, T., & McClintock, J. E. 2015, ApJ, 800, 17, doi: 10.1088/0004-637X/800/1/17
Freiburghaus, C., Rosswog, S., & Thielemann, F. K. 1999, ApJL, 525, L121, doi: 10.1086/312343
Freire, P. C. C., Ransom, S. M., Bégin, S., et al. 2008, ApJ, 675, 670, doi: 10.1086/526338
Frostig, D., Baker, J. W., Brown, J., et al. 2020, in Society of Photo-Optical Instrumentation Engineers (SPIE) Conference Series, Vol. 11447, Society of Photo-Optical Instrumentation Engineers (SPIE) Conference Series, 1144767, doi: 10.1117/12.2562842
Fryer, C. L., Woosley, S. E., & Hartmann, D. H. 1999, ApJ, 526, 152, doi: 10.1086/307992
Gaebel, S. M., & Veitch, J. 2017, Classical and Quantum Gravity, 34, 174003, doi: 10.1088/1361-6382/aa82d9
Gehrels, N., Cannizzo, J. K., Kanner, J., et al. 2016, ApJ, 820, 136, doi: 10.3847/0004-637X/820/2/136
Gehrels, N., Spergel, D., & WFIRST SDT Project. 2015, in Journal of Physics Conference Series, Vol. 610, Journal of Physics Conference Series, 012007, doi: 10.1088/1742-6596/610/1/012007
Ghirlanda, G., Salafia, O. S., Paragi, Z., et al. 2019, Science, 363, 968, doi: 10.1126/science.aau8815
Giacconi, R., Gursky, H., Paolini, F. R., & Rossi, B. B. 1962, PhRvL, 9, 439, doi: 10.1103/PhysRevLett.9.439
Gold, T. 1968, Nature, 218, 731, doi: 10.1038/218731a0
—. 1969, Nature, 221, 25, doi: 10.1038/221025a0
Goldstein, A., Veres, P., Burns, E., et al. 2017, ApJL, 848, L14, doi: 10.3847/2041-8213/aa8f41
Goldstein, A., Fletcher, C., Veres, P., et al. 2020, ApJ, 895, 40, doi: 10.3847/1538-4357/ab8bdb
Gompertz, B. P., Levan, A. J., Tanvir, N. R., et al. 2018, ApJ, 860, 62, doi: 10.3847/1538-4357/aac206
Gompertz, B. P., Cutter, R., Steeghs, D., et al. 2020, MNRAS, 497, 726, doi: 10.1093/mnras/staa1845

Graham, M. J., Kulkarni, S. R., Bellm, E. C., et al. 2019, PASP, 131, 078001, doi: 10.1088/1538-3873/ab006c
Groot, P. J. 2019, Nature Astronomy, 3, 1160, doi: 10.1038/s41550-019-0964-z
Guillochon, J., Parrent, J., Kelley, L. Z., & Margutti, R. 2017, ApJ, 835, 64, doi: 10.3847/1538-4357/835/1/64
Hajela, A., Margutti, R., Alexander, K. D., et al. 2019, ApJL, 886, L17, doi: 10.3847/2041-8213/ab5226
Hajela, A., Margutti, R., Bright, J. S., et al. 2021, arXiv e-prints, arXiv:2104.02070. https://arxiv.org/abs/2104.02070
Hall, E. D., & Evans, M. 2019, Classical and Quantum Gravity, 36, 225002, doi: 10.1088/1361-6382/ab41d6
Hannam, M., Schmidt, P., Bohé, A., et al. 2014, PhRvL, 113, 151101, doi: 10.1103/PhysRevLett.113.151101
Heinzel, J., Coughlin, M. W., Dietrich, T., et al. 2021, MNRAS, 502, 3057, doi: 10.1093/mnras/stab221
Herner, K., Annis, J., Brout, D., et al. 2020, Astronomy and Computing, 33, 100425, doi: 10.1016/j.ascom.2020.100425
Hewish, A., Bell, S. J., Pilkington, J. D. H., Scott, P. F., & Collins, R. A. 1968, Nature, 217, 709, doi: 10.1038/217709a0
Hinderer, T. 2008, ApJ, 677, 1216, doi: 10.1086/533487
Hinderer, T., Lackey, B. D., Lang, R. N., & Read, J. S. 2010, PhRvD, 81, 123016, doi: 10.1103/PhysRevD.81.123016
Hirata, K., Kajita, T., Koshiba, M., et al. 1987, PhRvL, 58, 1490, doi: 10.1103/PhysRevLett.58.1490
Hirata, K. S., Kajita, T., Koshiba, M., et al. 1988, PhRvD, 38, 448, doi: 10.1103/PhysRevD.38.448
Hogg, D. W., Baldry, I. K., Blanton, M. R., & Eisenstein, D. J. 2002, arXiv e-prints, astro. https://arxiv.org/abs/astro-ph/0210394
Holmbeck, E. M., Frebel, A., McLaughlin, G. C., et al. 2021, ApJ, 909, 21, doi: 10.3847/1538-4357/abd720
Holmbeck, E. M., Hansen, T. T., Beers, T. C., et al. 2020, ApJS, 249, 30, doi: 10.3847/1538-4365/ab9c19
Holz, D. E., & Hughes, S. A. 2005, ApJ, 629, 15, doi: 10.1086/431341
Hosseinzadeh, G., Cowperthwaite, P. S., Gomez, S., et al. 2019, ApJL, 880, L4, doi: 10.3847/2041-8213/ab271c
Hotokezaka, K., & Nakar, E. 2020, ApJ, 891, 152, doi: 10.3847/1538-4357/ab6a98
Hounsell, R., Scolnic, D., Foley, R. J., et al. 2018, ApJ, 867, 23, doi: 10.3847/1538-4357/aac08b
Hu, Y.-M., Raffai, P., Gondán, L., et al. 2015, Classical and Quantum Gravity, 32, 105010, doi: 10.1088/0264-9381/32/10/105010
Hulse, R. A., & Taylor, J. H. 1975, ApJL, 195, L51, doi: 10.1086/181708

Humason, M. L., Mayall, N. U., & Sandage, A. R. 1956, AJ, 61, 97, doi: 10.1086/107297
Husa, S., Khan, S., Hannam, M., et al. 2016, PhRvD, 93, 044006, doi: 10.1103/PhysRevD.93.044006
IndIGO Collaboration. 2011, LIGO-India, Proposal of the Consortium for Indian Initiative in Gravitational-wave Observations (IndIGO), Tech. Rep. LIGO-M1100296-v2, IndIGO, https://dcc.ligo.org/cgi-bin/DocDB/ShowDocument?docid=75988
Ivezić, Ž., Kahn, S. M., Tyson, J. A., et al. 2019, ApJ, 873, 111, doi: 10.3847/1538-4357/ab042c
Jin, Z.-P., Covino, S., Liao, N.-H., et al. 2020, Nature Astronomy, 4, 77, doi: 10.1038/s41550-019-0892-y
Jin, Z.-P., Hotokezaka, K., Li, X., et al. 2016, Nature Communications, 7, 12898, doi: 10.1038/ncomms12898
Kalogera, V., Belczynski, K., Kim, C., O'Shaughnessy, R., & Willems, B. 2007, PhR, 442, 75, doi: 10.1016/j.physrep.2007.02.008
Kanner, J. B., Littenberg, T. B., Cornish, N., et al. 2016, PhRvD, 93, 022002, doi: 10.1103/PhysRevD.93.022002
Kasen, D., Fernández, R., & Metzger, B. D. 2015, MNRAS, 450, 1777, doi: 10.1093/mnras/stv721
Kasen, D., Metzger, B., Barnes, J., Quataert, E., & Ramirez-Ruiz, E. 2017, Nature, 551, 80, doi: 10.1038/nature24453
Kasliwal, M. M., & Nissanke, S. 2014, ApJL, 789, L5, doi: 10.1088/2041-8205/789/1/L5
Kasliwal, M. M., Nakar, E., Singer, L. P., et al. 2017, Science, 358, 1559, doi: 10.1126/science.aap9455
Kasliwal, M. M., Anand, S., Ahumada, T., et al. 2020, ApJ, 905, 145, doi: 10.3847/1538-4357/abc335
Khan, S., Husa, S., Hannam, M., et al. 2016, PhRvD, 93, 044007, doi: 10.1103/PhysRevD.93.044007
King, I. 1952, ApJ, 115, 580, doi: 10.1086/145583
Klingler, N. J., Kennea, J. A., Evans, P. A., et al. 2019, ApJS, 245, 15, doi: 10.3847/1538-4365/ab4ea2
Klingler, N. J., Lien, A., Oates, S. R., et al. 2021, ApJ, 907, 97, doi: 10.3847/1538-4357/abd2c3
Korobkin, O., Rosswog, S., Arcones, A., & Winteler, C. 2012, Monthly Notices of the Royal Astronomical Society, 426, 1940, doi: 10.1111/j.1365-2966.2012.21859.x
Korobkin, O., Wollaeger, R. T., Fryer, C. L., et al. 2021, ApJ, 910, 116, doi: 10.3847/1538-4357/abe1b5
Kourkchi, E., & Tully, R. B. 2017, ApJ, 843, 16, doi: 10.3847/1538-4357/aa76db
Kouveliotou, C., Meegan, C. A., Fishman, G. J., et al. 1993, ApJL, 413, L101, doi: 10.1086/186969
Kramer, M., & Wex, N. 2009, Classical and Quantum Gravity, 26, 073001, doi: 10.1088/0264-9381/26/7/073001

Kulkarni, S. R. 2005, arXiv e-prints, astro. https://arxiv.org/abs/astro-ph/0510256
Lamb, G. P., Tanvir, N. R., Levan, A. J., et al. 2019, ApJ, 883, 48, doi: 10.3847/1538-4357/ab38bb
Lattimer, J. M. 2015, in American Institute of Physics Conference Series, Vol. 1645, Exotic Nuclei and Nuclear/Particle Astrophysics (V) From Nuclei to Stars: Carpathian Summer School of Physics 2014, 61–78, doi: 10.1063/1.4909560
Lattimer, J. M., Mackie, F., Ravenhall, D. G., & Schramm, D. N. 1977, ApJ, 213, 225, doi: 10.1086/155148
Lattimer, J. M., & Prakash, M. 2007, PhR, 442, 109, doi: 10.1016/j.physrep.2007.02.003
—. 2016, PhR, 621, 127, doi: 10.1016/j.physrep.2015.12.005
Lattimer, J. M., & Schramm, D. N. 1974, ApJL, 192, L145, doi: 10.1086/181612
Li, L.-X., & Paczyński, B. 1998, ApJL, 507, L59, doi: 10.1086/311680
Lippuner, J., Fernández, R., Roberts, L. F., et al. 2017, MNRAS, 472, 904, doi: 10.1093/mnras/stx1987
Lippuner, J., & Roberts, L. F. 2015, ApJ, 815, 82, doi: 10.1088/0004-637X/815/2/82
Lipunov, V. M., Gorbovskoy, E., Kornilov, V. G., et al. 2017, ApJL, 850, L1, doi: 10.3847/2041-8213/aa92c0
Littenberg, T. B., Baker, J. G., Buonanno, A., & Kelly, B. J. 2013, PhRvD, 87, 104003, doi: 10.1103/PhysRevD.87.104003
Littenberg, T. B., & Cornish, N. J. 2015, PhRvD, 91, 084034, doi: 10.1103/PhysRevD.91.084034
Lourie, N. P., Baker, J. W., Burruss, R. S., et al. 2020, in Society of Photo-Optical Instrumentation Engineers (SPIE) Conference Series, Vol. 11447, Society of Photo-Optical Instrumentation Engineers (SPIE) Conference Series, 114479K, doi: 10.1117/12.2561210
LVC. 2017, GRB Coordinates Network, 21513, 1
—. 2019, GRB Coordinates Network, 24168, 1
Manchester, R. N., & IPTA. 2013, Classical and Quantum Gravity, 30, 224010, doi: 10.1088/0264-9381/30/22/224010
McMahon, R. G., Banerji, M., Gonzalez, E., et al. 2013, The Messenger, 154, 35
Messick, C., Blackburn, K., Brady, P., et al. 2017, PhRvD, 95, 042001, doi: 10.1103/PhysRevD.95.042001
Metzger, B. D. 2019, Living Reviews in Relativity, 23, 1, doi: 10.1007/s41114-019-0024-0
Metzger, B. D., & Berger, E. 2012, ApJ, 746, 48, doi: 10.1088/0004-637X/746/1/48
Metzger, B. D., Martínez-Pinedo, G., Darbha, S., et al. 2010, MNRAS, 406, 2650, doi: 10.1111/j.1365-2966.2010.16864.x
Mills, C., Tiwari, V., & Fairhurst, S. 2018, PhRvD, 97, 104064, doi: 10.1103/PhysRevD.97.104064

Möller, P., Nix, J. R., Myers, W. D., & Swiatecki, W. J. 1995, Atomic Data and Nuclear Data Tables, 59, 185, doi: 10.1006/adnd.1995.1002
Morgan, R., Soares-Santos, M., Annis, J., et al. 2020, ApJ, 901, 83, doi: 10.3847/1538-4357/abafaa
Nakar, E., & Piran, T. 2011, Nature, 478, 82, doi: 10.1038/nature10365
Narayan, R., Paczynski, B., & Piran, T. 1992, ApJL, 395, L83, doi: 10.1086/186493
Nicholl, M., Margalit, B., Schmidt, P., et al. 2021, arXiv e-prints, arXiv:2102.02229. https://arxiv.org/abs/2102.02229
Nicholl, M., Berger, E., Kasen, D., et al. 2017, ApJL, 848, L18, doi: 10.3847/2041-8213/aa9029
Nissanke, S., Holz, D. E., Dalal, N., et al. 2013a, arXiv e-prints, arXiv:1307.2638. https://arxiv.org/abs/1307.2638
Nissanke, S., Holz, D. E., Hughes, S. A., Dalal, N., & Sievers, J. L. 2010, ApJ, 725, 496, doi: 10.1088/0004-637X/725/1/496
Nissanke, S., Kasliwal, M., & Georgieva, A. 2013b, ApJ, 767, 124, doi: 10.1088/0004-637X/767/2/124
Nissanke, S., Sievers, J., Dalal, N., & Holz, D. 2011, ApJ, 739, 99, doi: 10.1088/0004-637X/739/2/99
Nitz, A., Harry, I., Brown, D., et al. 2021, gwastro/pycbc: 1.18.0 release of PyCBC, v1.18.0, Zenodo, doi: 10.5281/zenodo.4556907
Nitz, A. H., Dal Canton, T., Davis, D., & Reyes, S. 2018, PhRvD, 98, 024050, doi: 10.1103/PhysRevD.98.024050
Norris, J. P., Cline, T. L., Desai, U. D., & Teegarden, B. J. 1984, Nature, 308, 434, doi: 10.1038/308434a0
Nuttall, L. K., Massinger, T. J., Areeda, J., et al. 2015, Classical and Quantum Gravity, 32, 245005, doi: 10.1088/0264-9381/32/24/245005
O'Connor, B., Troja, E., Dichiara, S., et al. 2021, MNRAS, 502, 1279, doi: 10.1093/mnras/stab132
Oke, J. B., & Sandage, A. 1968, ApJ, 154, 21, doi: 10.1086/149737
Oppenheimer, J. R., & Volkoff, G. M. 1939, Physical Review, 55, 374, doi: 10.1103/PhysRev.55.374
Özel, F., & Freire, P. 2016, ARA&A, 54, 401, doi: 10.1146/annurev-astro-081915-023322
Paczynski, B. 1986, ApJL, 308, L43, doi: 10.1086/184740
Page, K. L., Evans, P. A., Tohuvavohu, A., et al. 2020, MNRAS, 499, 3459, doi: 10.1093/mnras/staa3032
Pankow, C., Chase, E. A., Coughlin, S., Zevin, M., & Kalogera, V. 2018a, ApJL, 854, L25, doi: 10.3847/2041-8213/aaacd4
Pankow, C., Rizzo, M., Rao, K., Berry, C. P. L., & Kalogera, V. 2020, ApJ, 902, 71, doi: 10.3847/1538-4357/abb373

Pankow, C., Sampson, L., Perri, L., et al. 2017, ApJ, 834, 154, doi: 10.3847/1538-4357/834/2/154
Pankow, C., Chatziioannou, K., Chase, E. A., et al. 2018b, PhRvD, 98, 084016, doi: 10.1103/PhysRevD.98.084016
Pannarale, F., & Ohme, F. 2014, ApJL, 791, L7, doi: 10.1088/2041-8205/791/1/L7
Paterson, K., Lundquist, M. J., Rastinejad, J. C., et al. 2020, arXiv e-prints, arXiv:2012.11700. https://arxiv.org/abs/2012.11700
Patricelli, B., Razzano, M., Cella, G., et al. 2016, JCAP, 2016, 056, doi: 10.1088/1475-7516/2016/11/056
Perley, D. A., Metzger, B. D., Granot, J., et al. 2009, ApJ, 696, 1871, doi: 10.1088/0004-637X/696/2/1871
Pian, E., D'Avanzo, P., Benetti, S., et al. 2017, Nature, 551, 67, doi: 10.1038/nature24298
Planck Collaboration, Aghanim, N., Akrami, Y., et al. 2020, A&A, 641, A6, doi: 10.1051/0004-6361/201833910
Popham, R., Woosley, S. E., & Fryer, C. 1999, ApJ, 518, 356, doi: 10.1086/307259
Powell, J. 2018, Classical and Quantum Gravity, 35, 155017, doi: 10.1088/1361-6382/aacf18
Punturo, M., Abernathy, M., Acernese, F., et al. 2010, Classical and Quantum Gravity, 27, 194002, doi: 10.1088/0264-9381/27/19/194002
Racine, É. 2008, PhRvD, 78, 044021, doi: 10.1103/PhysRevD.78.044021
Rantsiou, E., Kobayashi, S., Laguna, P., & Rasio, F. A. 2008, ApJ, 680, 1326, doi: 10.1086/587858
Rastinejad, J. C., Fong, W., Kilpatrick, C. D., et al. 2021, arXiv e-prints, arXiv:2101.03175. https://arxiv.org/abs/2101.03175
Raymond, V., van der Sluys, M. V., Mandel, I., et al. 2009, Classical and Quantum Gravity, 26, 114007, doi: 10.1088/0264-9381/26/11/114007
Read, J. S., Markakis, C., Shibata, M., et al. 2009, PhRvD, 79, 124033, doi: 10.1103/PhysRevD.79.124033
Reisswig, C., Husa, S., Rezzolla, L., et al. 2009, PhRvD, 80, 124026, doi: 10.1103/PhysRevD.80.124026
Rezzolla, L., Most, E. R., & Weih, L. R. 2018, ApJL, 852, L25, doi: 10.3847/2041-8213/aaa401
Ristic, M., Champion, E., O'Shaughnessy, R., et al. 2021, arXiv e-prints, arXiv:2105.07013. https://arxiv.org/abs/2105.07013
Rodrigo, C., & Solano, E. 2020, in Contributions to the XIV.0 Scientific Meeting (virtual) of the Spanish Astronomical Society, 182
Rodriguez, C. L., Farr, B., Raymond, V., et al. 2014, ApJ, 784, 119, doi: 10.1088/0004-637X/784/2/119
Roming, P. W. A., Kennedy, T. E., Mason, K. O., et al. 2005, SSRv, 120, 95, doi: 10.1007/s11214-005-5095-4

Rossi, A., Stratta, G., Maiorano, E., et al. 2020, MNRAS, 493, 3379, doi: 10.1093/mnras/staa479
Rosswog, S., Feindt, U., Korobkin, O., et al. 2017, Classical and Quantum Gravity, 34, 104001, doi: 10.1088/1361-6382/aa68a9
Sagiv, I., Gal-Yam, A., Ofek, E. O., et al. 2014, AJ, 147, 79, doi: 10.1088/0004-6256/147/4/79
Sari, R., Piran, T., & Narayan, R. 1998, ApJL, 497, L17, doi: 10.1086/311269
Sathyaprakash, B. S., & Schutz, B. F. 2009, Living Reviews in Relativity, 12, 2, doi: 10.12942/lrr-2009-2
Savchenko, V., Ferrigno, C., Kuulkers, E., et al. 2017, ApJL, 848, L15, doi: 10.3847/2041-8213/aa8f94
Schmidt, P., Ohme, F., & Hannam, M. 2015, PhRvD, 91, 024043, doi: 10.1103/PhysRevD.91.024043
Schutz, B. F. 1986, Nature, 323, 310, doi: 10.1038/323310a0
—. 2011, Classical and Quantum Gravity, 28, 125023, doi: 10.1088/0264-9381/28/12/125023
Scolnic, D., Kessler, R., Brout, D., et al. 2018, ApJL, 852, L3, doi: 10.3847/2041-8213/aa9d82
Searle, A. C., Scott, S. M., McClelland, D. E., & Finn, L. S. 2006, PhRvD, 73, 124014, doi: 10.1103/PhysRevD.73.124014
Shappee, B. J., Simon, J. D., Drout, M. R., et al. 2017, Science, 358, 1574, doi: 10.1126/science.aaq0186
Shklovsky, I. S. 1967, ApJL, 148, L1, doi: 10.1086/180001
Singer, L. P., & Price, L. R. 2016, PhRvD, 93, 024013, doi: 10.1103/PhysRevD.93.024013
Singer, L. P., Price, L. R., Farr, B., et al. 2014, ApJ, 795, 105, doi: 10.1088/0004-637X/795/2/105
Smartt, S. J., Chen, T. W., Jerkstrand, A., et al. 2017, Nature, 551, 75, doi: 10.1038/nature24303
Sneden, C., Lawler, J. E., Cowan, J. J., Ivans, I. I., & Den Hartog, E. A. 2009, ApJS, 182, 80, doi: 10.1088/0067-0049/182/1/80
Soares-Santos, M., Kessler, R., Berger, E., et al. 2016, ApJL, 823, L33, doi: 10.3847/2041-8205/823/2/L33
Soares-Santos, M., Holz, D. E., Annis, J., et al. 2017, ApJL, 848, L16, doi: 10.3847/2041-8213/aa9059
Spergel, D., Gehrels, N., Baltay, C., et al. 2015, arXiv e-prints, arXiv:1503.03757. https://arxiv.org/abs/1503.03757
Sutherland, W., Emerson, J., Dalton, G., et al. 2015, A&A, 575, A25, doi: 10.1051/0004-6361/201424973
Symbalisty, E., & Schramm, D. N. 1982, Astrophys. Lett., 22, 143
Tanvir, N. R., Levan, A. J., Fruchter, A. S., et al. 2013, Nature, 500, 547, doi: 10.1038/nature12505

Tanvir, N. R., Levan, A. J., González-Fernández, C., et al. 2017, ApJL, 848, L27, doi: 10.3847/2041-8213/aa90b6
Tauris, T. M., Kramer, M., Freire, P. C. C., et al. 2017, ApJ, 846, 170, doi: 10.3847/1538-4357/aa7e89
Taylor, J. H., & Weisberg, J. M. 1982, ApJ, 253, 908, doi: 10.1086/159690
Thakur, A. L., Dichiara, S., Troja, E., et al. 2020, MNRAS, 499, 3868, doi: 10.1093/mnras/staa2798
Troja, E., Piro, L., van Eerten, H., et al. 2017, Nature, 551, 71, doi: 10.1038/nature24290
Troja, E., Ryan, G., Piro, L., et al. 2018, Nature Communications, 9, 4089, doi: 10.1038/s41467-018-06558-7
Troja, E., Castro-Tirado, A. J., Becerra González, J., et al. 2019a, MNRAS, 489, 2104, doi: 10.1093/mnras/stz2255
Troja, E., van Eerten, H., Ryan, G., et al. 2019b, MNRAS, 489, 1919, doi: 10.1093/mnras/stz2248
Troja, E., O'Connor, B., Ryan, G., et al. 2021, arXiv e-prints, arXiv:2104.13378. https://arxiv.org/abs/2104.13378
Usman, S. A., Nitz, A. H., Harry, I. W., et al. 2016, Classical and Quantum Gravity, 33, 215004, doi: 10.1088/0264-9381/33/21/215004
Utsumi, Y., Tanaka, M., Tominaga, N., et al. 2017, PASJ, 69, 101, doi: 10.1093/pasj/psx118
Valenti, S., Sand, D. J., Yang, S., et al. 2017, ApJL, 848, L24, doi: 10.3847/2041-8213/aa8edf
Vallisneri, M. 2008, PhRvD, 77, 042001, doi: 10.1103/PhysRevD.77.042001
—. 2011, PhRvL, 107, 191104, doi: 10.1103/PhysRevLett.107.191104
van der Sluys, M. V., Röver, C., Stroeer, A., et al. 2008, ApJL, 688, L61, doi: 10.1086/595279
Veitch, J., & Vecchio, A. 2010, PhRvD, 81, 062003, doi: 10.1103/PhysRevD.81.062003
Veitch, J., Mandel, I., Aylott, B., et al. 2012, PhRvD, 85, 104045, doi: 10.1103/PhysRevD.85.104045
Veitch, J., Raymond, V., Farr, B., et al. 2015, PhRvD, 91, 042003, doi: 10.1103/PhysRevD.91.042003
Vines, J., Flanagan, É. É., & Hinderer, T. 2011, PhRvD, 83, 084051, doi: 10.1103/PhysRevD.83.084051
Vitale, S., & Chen, H.-Y. 2018, PhRvL, 121, 021303, doi: 10.1103/PhysRevLett.121.021303
Vitale, S., & Zanolin, M. 2011, PhRvD, 84, 104020, doi: 10.1103/PhysRevD.84.104020
Watson, A. M., Lee, W. H., Troja, E., et al. 2016, in Society of Photo-Optical Instrumentation Engineers (SPIE) Conference Series, Vol. 9910, Observatory Operations: Strategies, Processes, and Systems VI, ed. A. B. Peck, R. L. Seaman, & C. R. Benn, 99100G, doi: 10.1117/12.2232898
Weisberg, J. M., Taylor, J. H., & Fowler, L. A. 1981, Scientific American, 245, 66

Wen, L., & Chen, Y. 2010, PhRvD, 81, 082001, doi: 10.1103/PhysRevD.81.082001
Winteler, C., Käppeli, R., Perego, A., et al. 2012, ApJL, 750, L22, doi: 10.1088/2041-8205/750/1/L22
Wollaeger, R. T., & van Rossum, D. R. 2014, ApJS, 214, 28, doi: 10.1088/0067-0049/214/2/28
Wollaeger, R. T., van Rossum, D. R., Graziani, C., et al. 2013, ApJS, 209, 36, doi: 10.1088/0067-0049/209/2/36
Wollaeger, R. T., Korobkin, O., Fontes, C. J., et al. 2018, MNRAS, 478, 3298, doi: 10.1093/mnras/sty1018
Wollaeger, R. T., Fryer, C. L., Chase, E. A., et al. 2021, arXiv e-prints, arXiv:2105.11543. https://arxiv.org/abs/2105.11543
Wysocki, D., Lange, J., & O'Shaughnessy, R. 2019, PhRvD, 100, 043012, doi: 10.1103/PhysRevD.100.043012
Yang, B., Jin, Z.-P., Li, X., et al. 2015, Nature Communications, 6, 7323, doi: 10.1038/ncomms8323
Zevin, M., Pankow, C., Rodriguez, C. L., et al. 2017, ApJ, 846, 82, doi: 10.3847/1538-4357/aa8408
Zhu, X., Thrane, E., Osłowski, S., Levin, Y., & Lasky, P. D. 2018, PhRvD, 98, 043002, doi: 10.1103/PhysRevD.98.043002
Zhu, Y. L., Lund, K. A., Barnes, J., et al. 2021, ApJ, 906, 94, doi: 10.3847/1538-4357/abc69e

APPENDIX A

Supplementary Figures

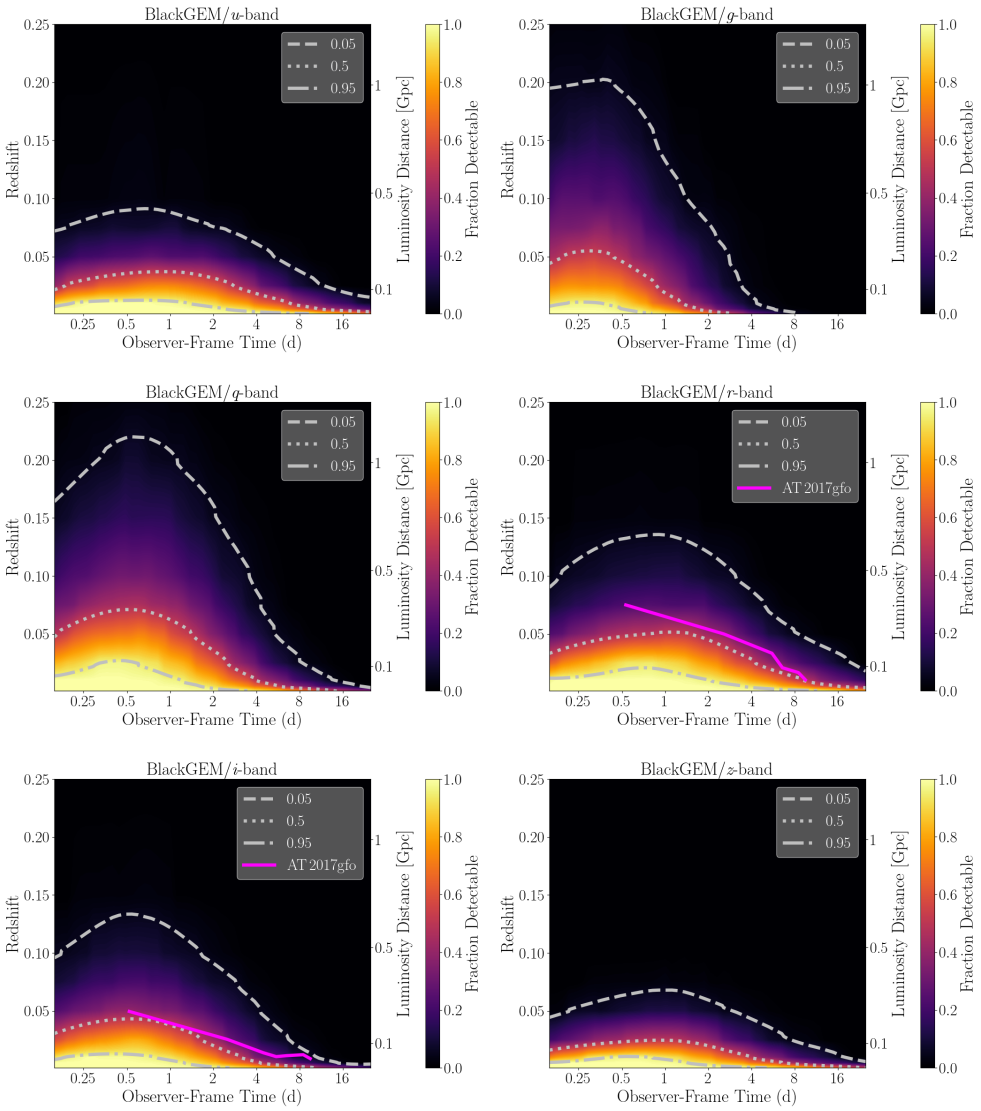

Figure A.1. Detectability constraints for six BlackGEM filters. Contours indicate the fraction of 48,600 simulated kilonovae (900 simulations each rendered at 54 viewing angles) with apparent magnitudes brighter than the limiting magnitude in each filter, for a given redshift and observer-frame time. The three white contours demarcate regions where 5%, 50%, and 95% of simulated kilonovae are detectable. The magenta curve represents each filter's ability to detect AT 2017gfo-like kilonovae; we only present AT 2017gfo-like detectability for filters that are fully spanned by AT 2017gfo spectral observations.

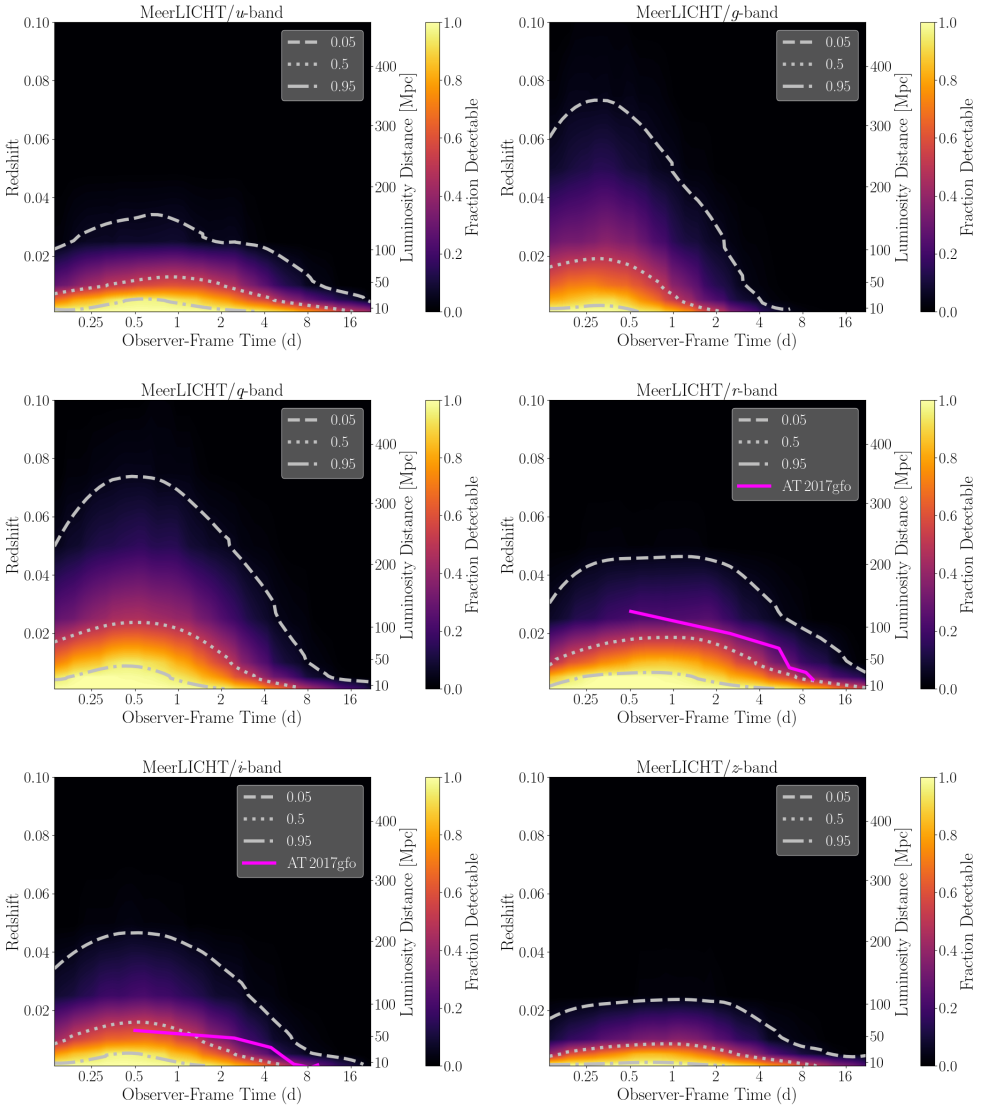

Figure A.2. Detectability contours for MeerLICHT (see Figure A.1 caption).

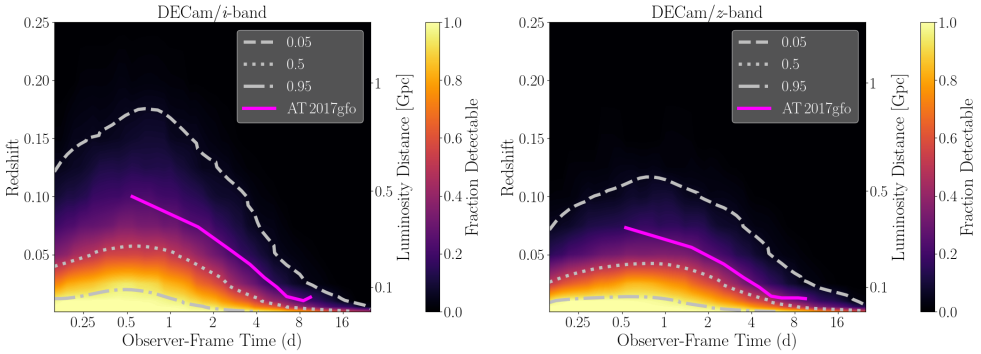

Figure A.3. Detectability contours for DECam (see Figure A.1 caption).

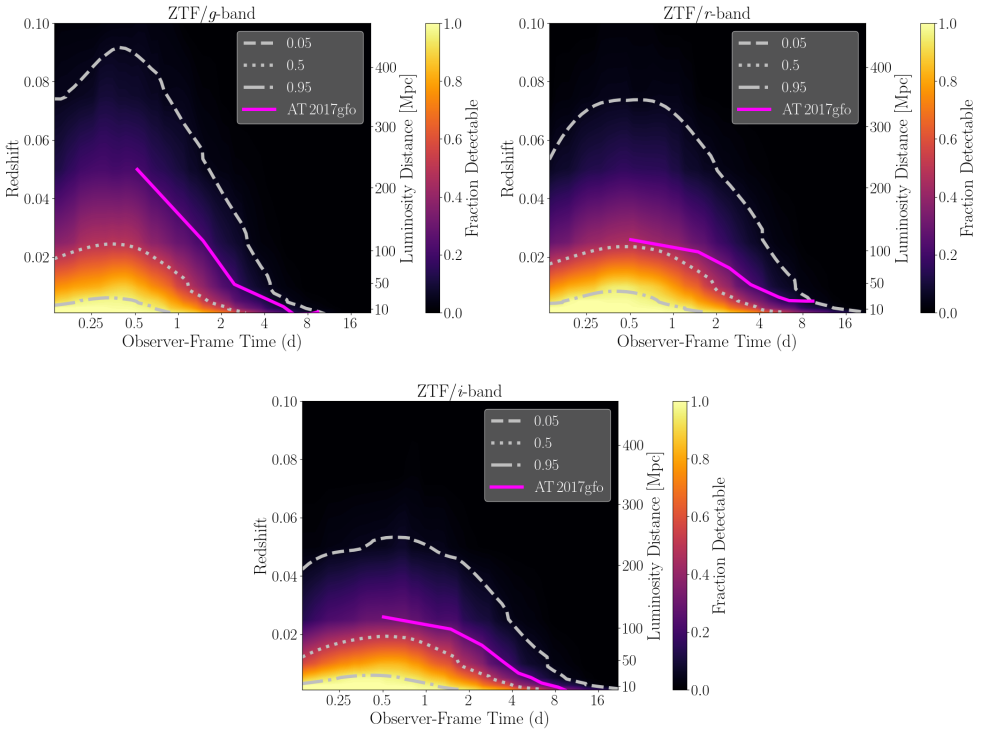

Figure A.4. Detectability contours for ZTF (see Figure A.1 caption).

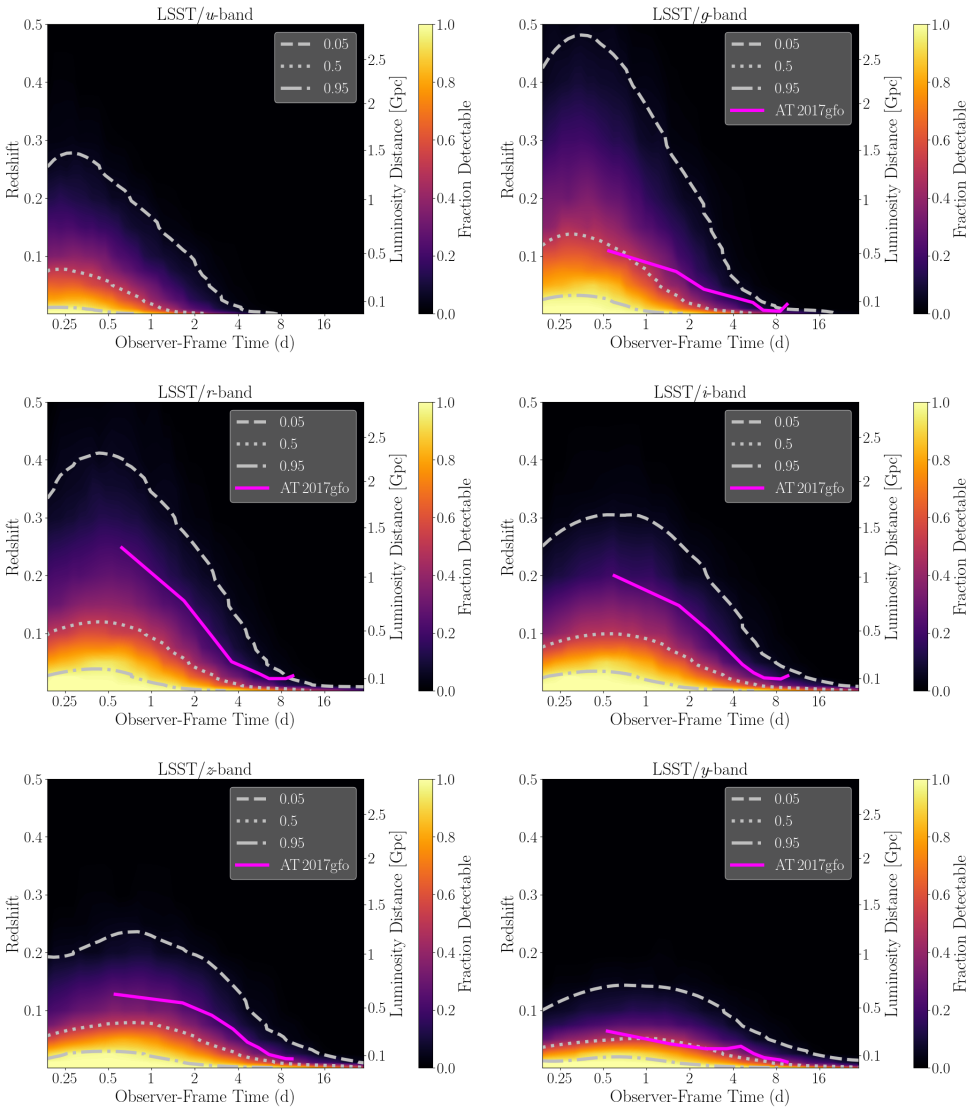

Figure A.5. Detectability contours for LSST (see Figure A.1 caption).

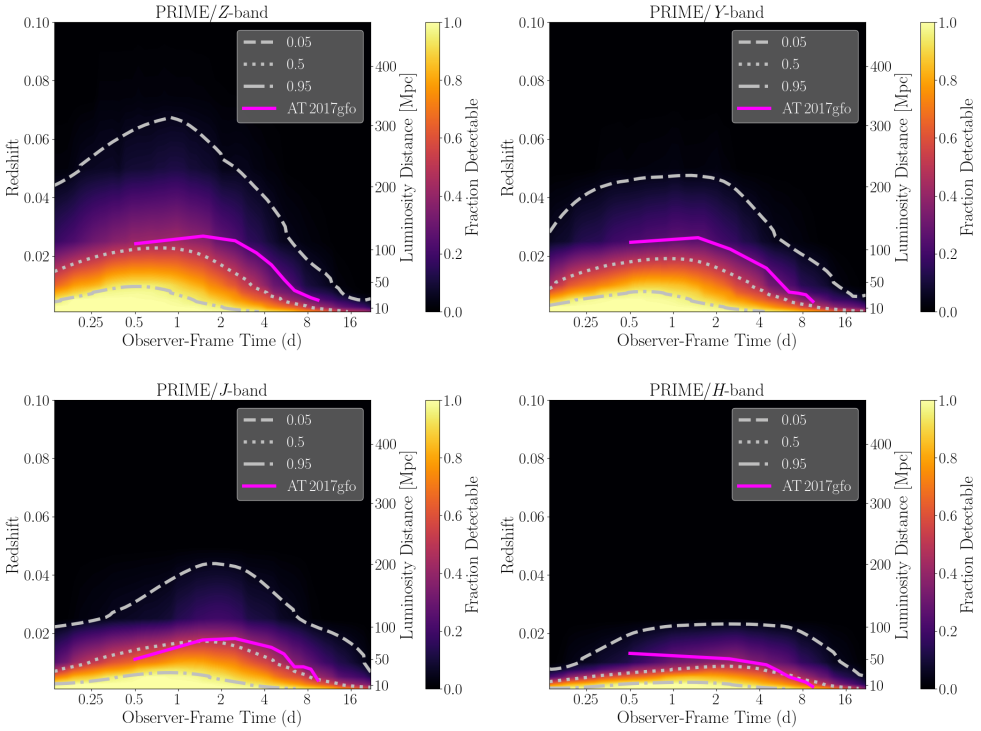

Figure A.6. Detectability contours for PRIME (see Figure A.1 caption).

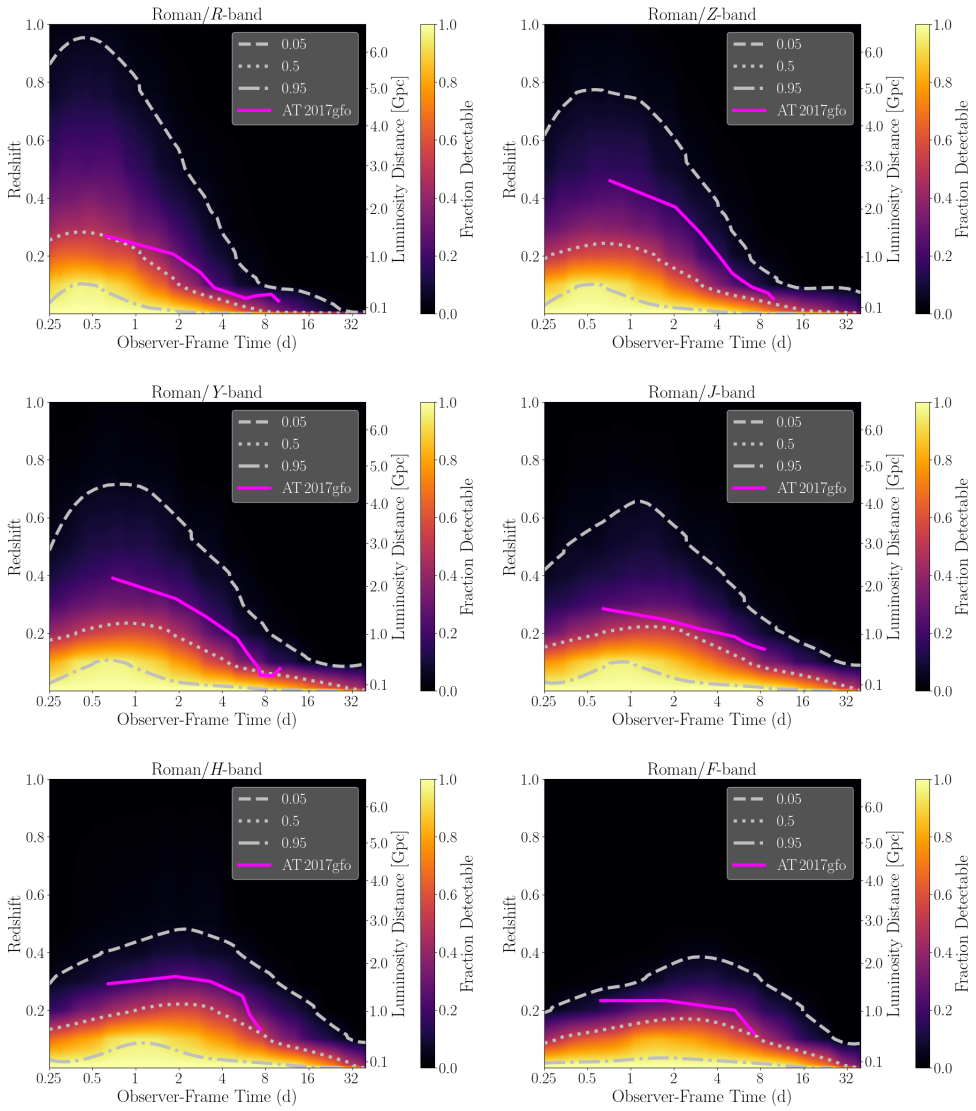

Figure A.7. Detectability contours for Roman (see Figure A.1 caption).

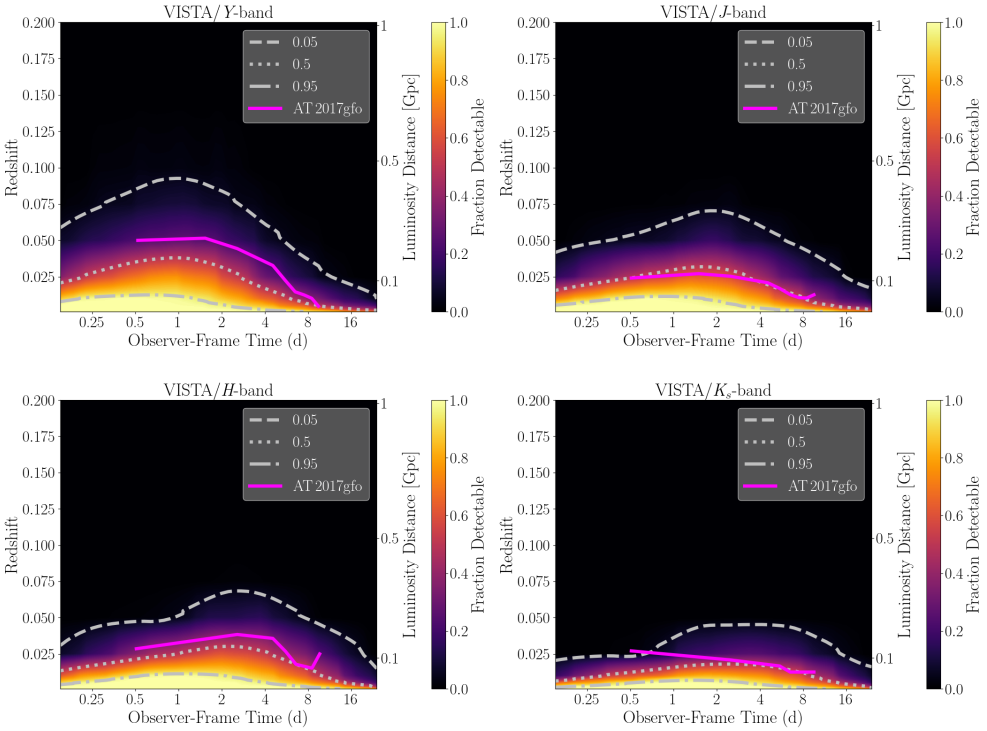

Figure A.8. Detectability contours for VISTA (see Figure A.1 caption).

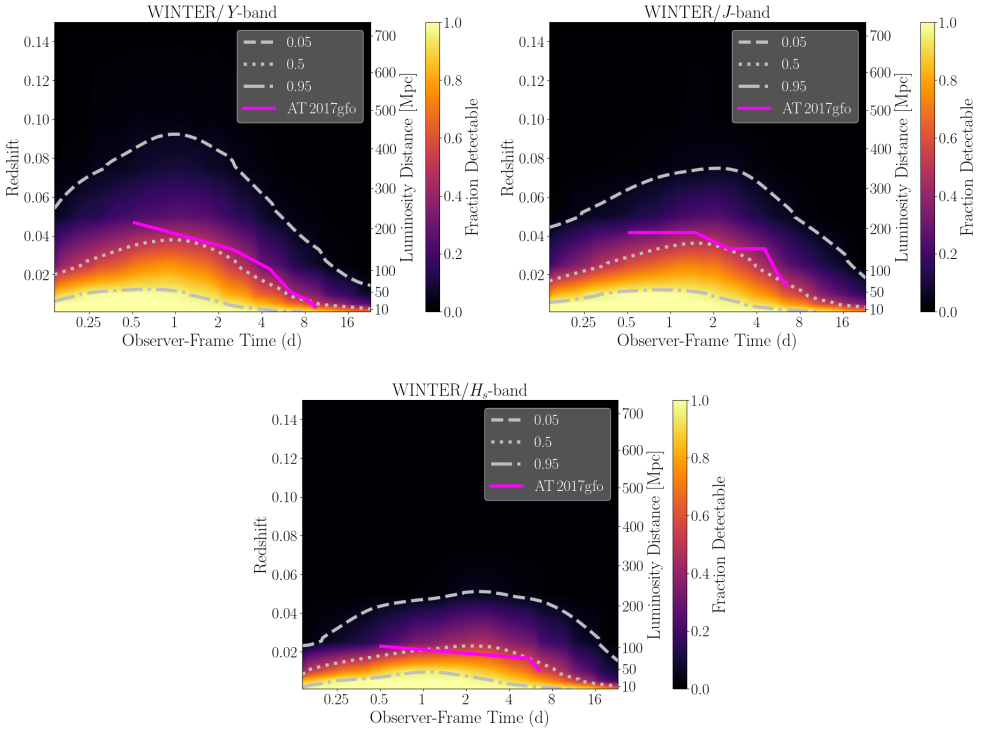

Figure A.9. Detectability contours for WINTER (see Figure A.1 caption).

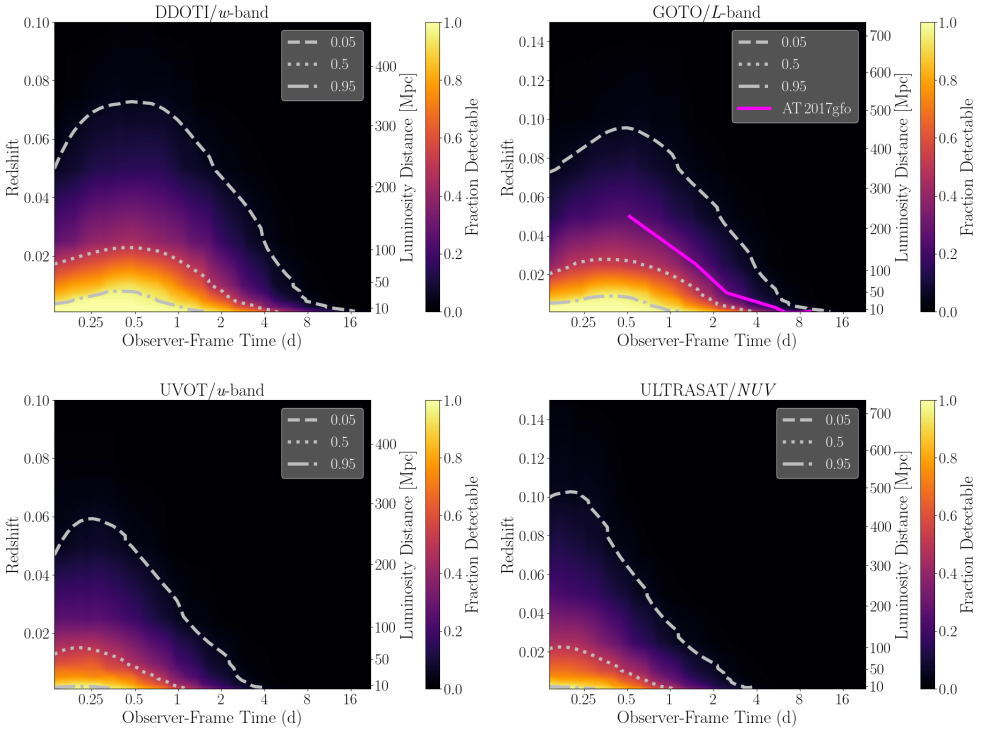

Figure A.10. Detectability contours for instruments with only one filter included in the study: DDOTI (*top left*), GOTO (*top right*), *Swift*/UVOT (*bottom left*), and ULTRASAT (*bottom right*). See Figure A.1 for more details. Note that the range of the vertical axis is not consistent in each panel.